Modulation Linearity of Si-Based Electro-Optic Modulators for Microwave Photonics

Seong, Minhyeok

Department of
Electrical and Electronic Engineering
Graduate School
Yonsei University

Modulation Linearity of Si-Based Electro-Optic Modulators for Microwave Photonics

Advisor Choi, Woo-Young

A Dissertation Submitted
to the Department of
Electrical and Electronic Engineering
and the Committee on Graduate School
of Yonsei University in Partial Fulfillment of the
Requirements for the Degree of
Doctor of Philosophy

Seong, Minhyeok

January 2026

Modulation Linearity of Si-Based Electro-Optic Modulators for Microwave Photonics

This Certifies that the Dissertation of Seong, Minhyeok is Approved

Committee Chair	**Choi, Woo-Young**
Committee Member	**Han, Sang-Kook**
Committee Member	**Lee, Myung-Jae**
Committee Member	**Park, Kangyeob**
Committee Member	**Im, Chul-Soon**

Department of Electrical and Electronic Engineering
Graduate School
Yonsei University
January 2026

TABLE OF CONTENTS

LIST OF FIGURES

LIST OF TABLES

ABSTRACT

Modulation Linearity of Si-Based Electro-Optic Modulators for Microwave Photonics

This dissertation presents a comprehensive study on the modeling, design, and characterization of highly linear silicon (Si) electro-optic (EO) modulators for next-generation microwave photonics (MWP) systems. Facing the limitations of digital electronics, MWP has emerged as a promising solution due to its wide frequency bandwidth, low transmission loss, and immunity to electromagnetic interference, which are essential for meeting the demands of future communication technologies. A key component of these systems is the Si-based EO modulator, which, despite offering high integration density and low fabrication cost, suffers from inherent nonlinearity due to the effects of its PN junctions. This nonlinearity degrades the overall system performance, making third-order intermodulation distortion (IMD3) and spurious-free dynamic range (SFDR) critical performance indicators.

While external compensation techniques, such as electronic pre-distortion, have been proposed to mitigate this issue, they are often unsuitable for broadband photonic systems due to high power consumption and narrow bandwidth. Therefore, it is crucial to develop EO modulators with inherently high linearity. This dissertation highlights the importance of creating accurate simulation models that can precisely predict and optimize modulator linearity. The research presented

here outlines a modeling and design approach to enhance the linearity of Si EO modulators, ultimately demonstrating the effectiveness of the proposed methodology.

This dissertation first introduces a novel and accurate simulation model for Si traveling-wave electrode Mach-Zehnder modulators (TWE MZMs). This model accounts for the nonlinearities of both the electro-optic phase shifters and the TWE, incorporating key parameters such as voltage-dependent effective refractive index and junction capacitance. The model parameters are extracted from a combination of measurements and simulations, and its accuracy is validated by comparing simulated and experimental results for electro-optic frequency response and IMD3. Our analysis reveals that the nonlinear variation of the effective refractive index and junction capacitance are the dominant contributors to IMD3, with their relative importance depending on the DC bias voltage. By accurately estimating the noise floor from RIN, shot noise, and thermal noise, our model effectively predicts the SFDR of the device, providing a valuable tool for the design and optimization of high-performance Si MZMs.

Furthermore, I propose a high-linear Si ring-assisted Mach-Zehnder modulator (RAMZM) designed for MWP applications. The device utilizes a differential modulation scheme and integrates two depletion-mode Si ring modulators into a Mach-Zehnder interferometer. To ensure optimal performance, the device incorporates thermal tuning for optical biasing. Through two-tone measurements, the proposed RAMZM demonstrates an exceptionally high SFDR of 105.4 $dB \cdot Hz^{6/7}$ at 10 GHz, while maintaining a compact footprint of approximately 1 mm^2. Notably, the measurements reveal a dominant 7th-order intermodulation distortion, indicating a significant improvement in linearity compared to

conventional Si modulators. This high-performance and compact RAMZM is a promising candidate for broadband and high-fidelity next-generation communication systems.

Keywords: Silicon photonics, microwave photonics, electro-optic modulator, modulation linearity, intermodulation distortion, spurious-free dynamic range, Mach-Zehnder modulator, traveling-wave electrode, ring-assisted Mach-Zehnder modulator

1. Introduction

1.1. Optical Interconnect

In recent years, the number of data centers worldwide has increased significantly to meet the ever-growing data demands driven by applications such as video streaming, social networking services (SNS), and artificial intelligence (AI) computing systems for a vast number of mobile users. Fig. 1-1 illustrates the projected growth in Internet of Things (IoT) connections from 2019 to 2030. Until 2024, the annual growth rate of IoT connections exceeded 20%, and it is expected to remain above 15% in the following years [1]. As a result, the number of companies managing these connections is also increasing globally. Furthermore, as shown in Fig. 1-2, the volume of data traffic required by communication systems is rising exponentially every year [2], emphasizing the growing need for data centers equipped with high-bandwidth interconnects. This trend necessitates a

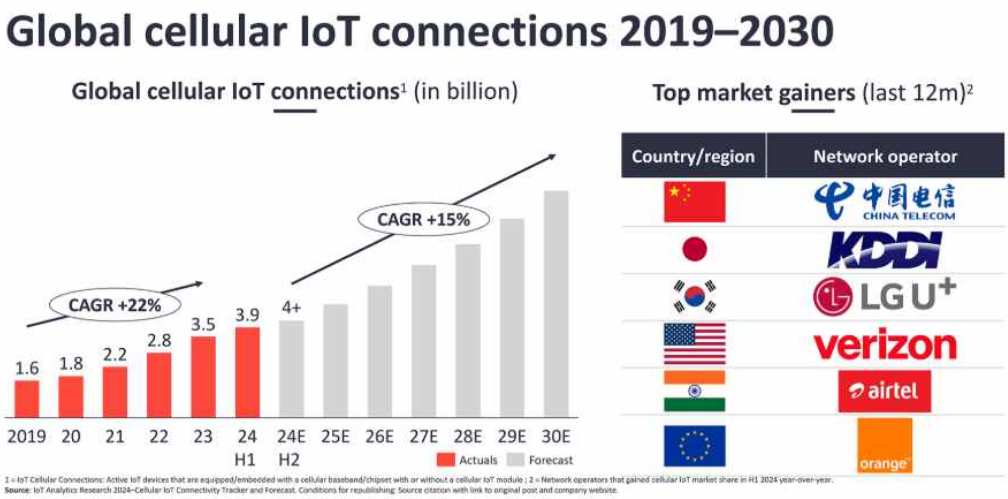

Fig. 1-1. Global IoT connections from 2019 to 2030 [1].

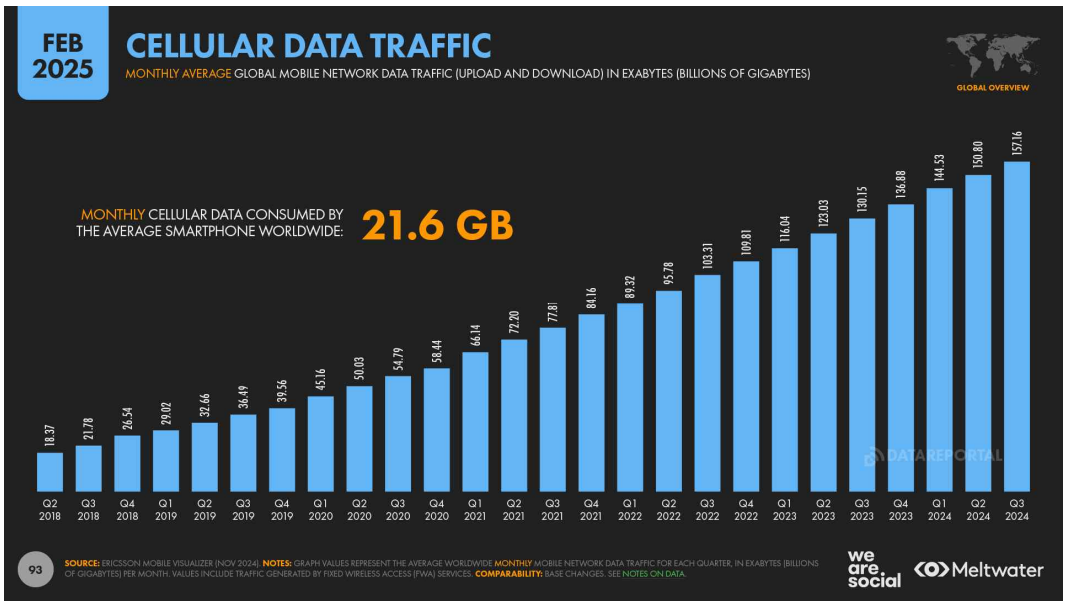

Fig. 1-2. Cellular data traffic by 2024 [2].

greater number of data centers capable of supporting high-bandwidth interconnects. To accommodate such large-scale data traffic, all levels of interconnect—ranging from inter-data center links to rack-to-rack, rack-to-chip, and even chip-to-chip connections—have become critical. Consequently, there is a growing demand for interconnect technologies that can support high-speed data transmission.

Traditionally, optical interconnects have been widely used for long-distance communications, such as transcontinental data transmission. However, the increasing need for higher data rates due to substantial data usage has led to a growing importance of optical interconnects for short-reach communication as well, and they are now widely being commercialized. As a result, many interconnects that were previously implemented using electrical signaling are being replaced by

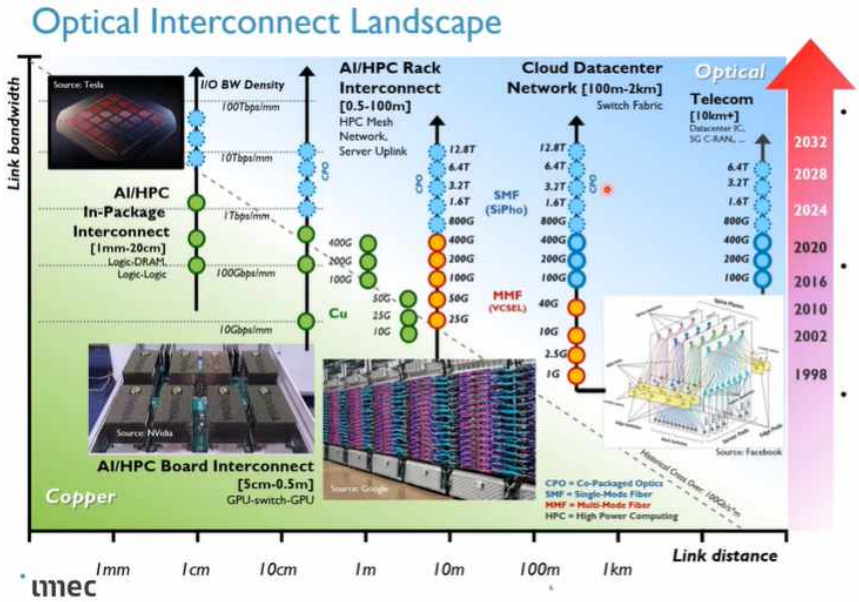

Fig. 1-3. Types and its distances of optical interconnect [5].

optical solutions, with data transmission speeds evolving from 100 Gbps to 400 Gbps, and even beyond 800 Gbps [3], [4].

Fig. 1-3 illustrates not only the increasing bandwidth requirements for interconnects but also the trend toward shorter transmission distances for optical links [5]. Whereas optical communication was previously limited to inter-data center networks, it is now increasingly employed within data centers themselves, covering shorter distances. Furthermore, high-performance electronic systems such as computing platforms require high bandwidth density and minimal latency. To meet these demands, significant efforts have been made to develop optical I/O technologies integrated with electronics in a single package, such as chiplets, for use in high-speed computing systems.

Fig. 1-4 demonstrates that both single-mode fiber (SMF) and multimode fiber (MMF) communications are being used for interconnects, even for distances below 1 km [6]. For lower data rates below 10 Gb/s, MMF interconnects using directly modulated vertical-cavity surface-emitting lasers (VCSELs) at 850 nm offer a cost-effective solution. However, as data rate should exceed 100 Gb/s, SMF communications at the O-band (1310 nm) or C-band (1550 nm) have emerged as more speculative solutions. This is primarily due to their compatibility with various bandwidth-scaling technologies, such as wavelength division multiplexing (WDM) and coherent communication.

Therefore, SMF communication has become indispensable for a wide range of interconnect applications, including data centers and high-performance computing systems. To support such communication needs, silicon (Si) photonics has emerged as one of the most promising technology platforms, offering a compelling balance between high performance and cost efficiency.

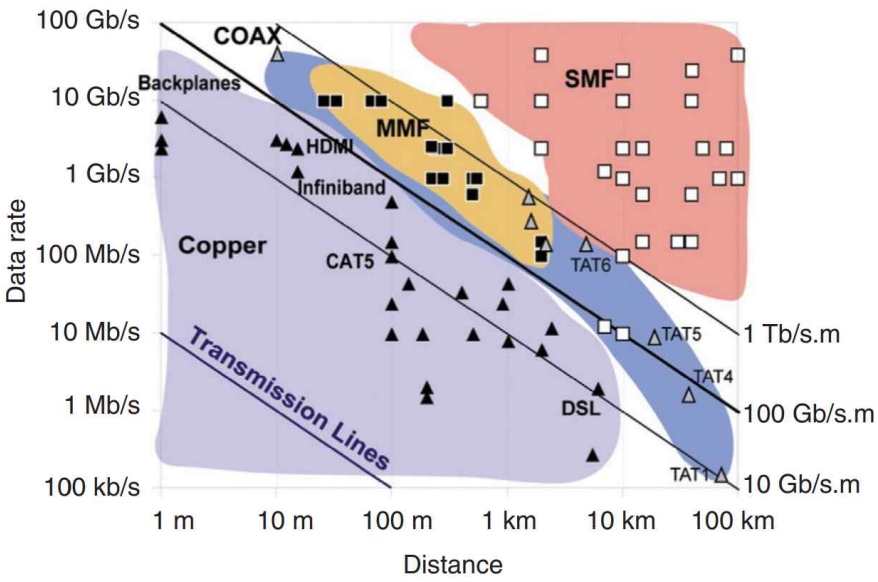

Fig 1-4. Various interconnect types according to data rates and distances [6].

1.2. Silicon Photonics

Si photonics is a technology that leverages Si-based photonic integrated circuits (PICs) to implement optical functions. This technology is built upon well-established Si manufacturing processes such as CMOS and BiCMOS, which are widely used in electronic circuit fabrication. Since Si is transparent in the 1310 nm and 1550 nm wavelength bands, it is not only feasible but also highly promising for use in optical fiber communication.

In addition, Si offers a significant refractive index contrast with its surrounding oxide cladding (typically SiO_2), which enables the formation of low-loss optical waveguides. This contrast allows for the miniaturization of photonic components, making PICs more compact and efficient compared to those based on compound semiconductors such as indium phosphide (InP), gallium arsenide (GaAs), or lithium niobate ($LiNbO_3$).

A major limitation of conventional optical interconnects has been their high cost. Most high-performance photonic devices have traditionally been fabricated using III-V compound semiconductors (e.g., InP [7], [8], GaAs [9], [10]) or electro-optic materials like $LiNbO_3$ [11], [12], which are not compatible with large-scale manufacturing. These materials inherently suffer from limited production scalability, leading to higher per-device manufacturing costs. Thus, for optical interconnects to be more broadly deployed, it is essential to develop photonic devices that are both cost-effective and scalable.

In this context, Si photonics has gained significant attention as it enables the use of mature CMOS-compatible Si fabrication technologies [13]-[15]. Si's transparency in both the C-band (1530–1565 nm) and O-band (1260–1360 nm)

makes it highly compatible with existing optical interconnect infrastructures. These advantages have facilitated the development of various Si photonics-based components, including optical filters [16], [17], photodetectors (PDs) [18], [19], and optical modulators [20], [21].

Recently, Si photonics has advanced toward realizing high-density photonic integrated circuits. As illustrated in Fig. 1-5, Si-based PICs are not only being applied in traditional data communication systems but are also expanding into emerging fields such as quantum computing [22], programmable photonic circuits [23], and microwave photonics [24].

The ability to reuse mature Si manufacturing processes from the electronics industry significantly enhances the cost-efficiency of Si photonics. As a result, Si photonics is widely recognized as a key platform for next-generation optical

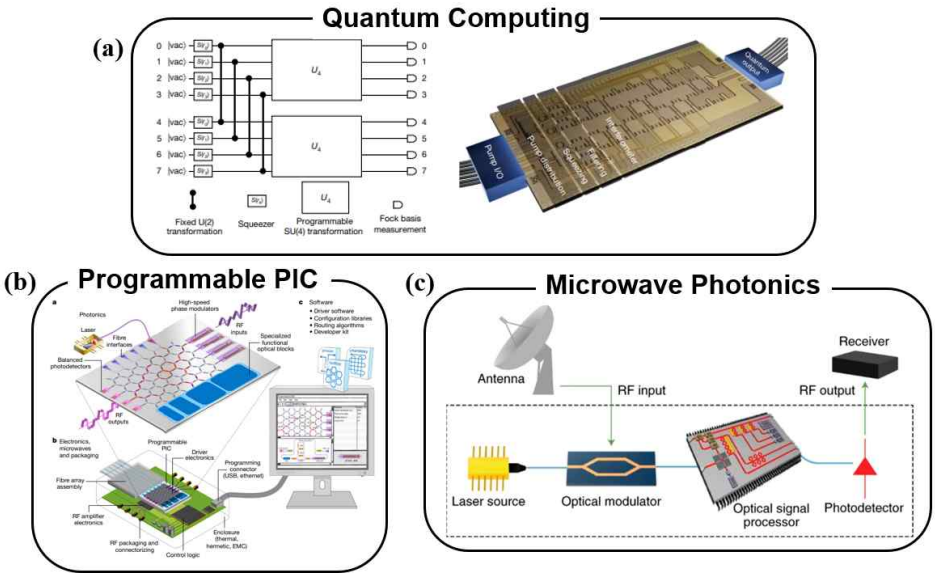

Fig. 1-5. Applications with Si photonics. (a) Quantum computing [22], (b) programmable PIC [23], and (c) microwave photonics [24].

interconnects. Its applications continue to diversify, finding increasing relevance in LiDAR, biosensing, and microwave photonics. As shown in Fig. 1-6, this technological versatility indicates strong potential for future market growth [25].

In Si photonics, optical interconnects typically employ modulators rather than direct modulation of lasers. Although direct laser modulation is a cost-effective approach and has led to the commercialization and widespread use of tunable lasers by many companies, it inherently suffers from limitations in modulation bandwidth due to the physical structure of the laser. Moreover, when Si-based lasers are integrated on-chip, achieving high efficiency becomes particularly challenging. As a result, to overcome these constraints, Si photonics more commonly relies on external modulation using optical modulators rather than directly modulating the laser. These modulators enable electrical signals to be either directly or indirectly converted into optical signals, making them essential components in high-speed optical interconnect systems.

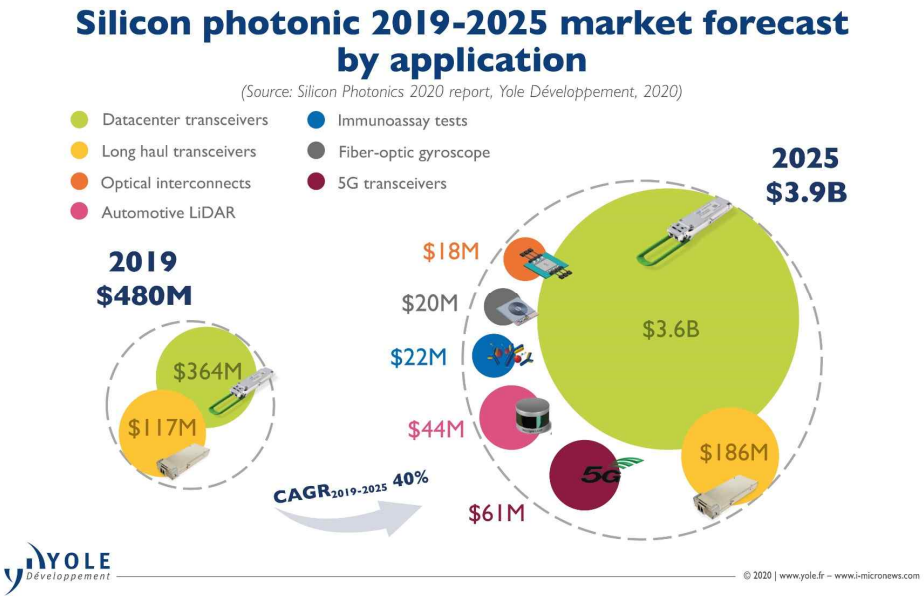

Fig. 1-6. Si photonics market scale [25].

1.3. Microwave Photonics

The growing demand for next-generation communication systems—such as 6G and IoT—is driving the development of communication networks that operate across multiple frequency bands, reach higher frequencies, and support broadband front-end systems [26]-[28]. While digital electronics are widely used, their performance is constrained by the limited speed of digital signal processors (typically below a few gigahertz). Moreover, conventional electronic systems struggle to meet the stringent requirements of modern radio-frequency (RF) applications due to limitations in analog-to-digital/digital-to-analog conversion speeds, poor tunability, and inherent signal losses [29].

Microwave photonics (MWP) offers a promising solution to these challenges [30]-[32]. By using photonic components to handle RF signals, MWP enables the generation, transmission, processing, and measurement of these signals with significant performance benefits. Photonic devices bring key advantages such as low transmission loss, wide frequency bandwidth, reconfigurability, and immunity to electromagnetic interference (EMI). These strengths allow RF systems to perform advanced functions that are difficult or impossible to achieve through purely electronic means, opening new possibilities for next-generation communication technologies.

Over the past 30 years, MWP has played a foundational role in communications, especially with the widespread use of optical fibers, which offer unparalleled bandwidth and low-loss signal transmission compared to traditional coaxial cables. Despite the increasing use of MWP for RF signal handling in communication and data systems, current MWP implementations still largely

depend on discrete optoelectronic and fiber-based components, which tend to be bulky, expensive, power-intensive, and lack scalability or flexibility.

After optical signal distribution, a photodetector converts the modulated optical signal back into the RF domain. This optical-to-electrical conversion is typically carried out using a reverse-biased photodetector with a P-I-N structure, which consists of an intrinsic layer sandwiched between heavily doped p-type and n-type layers. For high-performance MWP links, it is crucial to use photodetectors that offer high linearity, efficiency, and speed. These characteristics are often measured by three key parameters: responsivity, bandwidth, and linearity [33]-[35]. Additionally, to accommodate high optical power levels and minimize signal degradation, photodetectors with high power-handling capability are preferred.

As illustrated in Fig. 1-7, an MWP system integrates various signal processing functionalities into the optical domain, between the electro-optic (EO) and

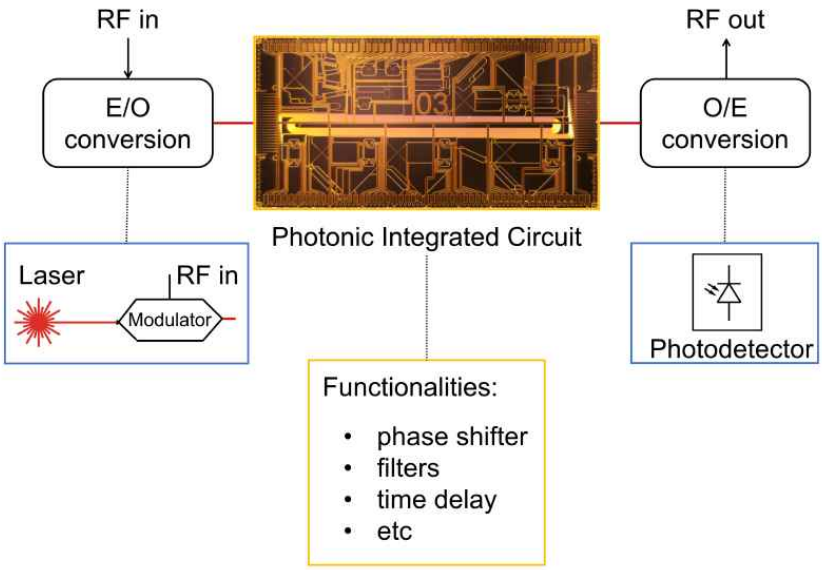

Fig. 1-7 Block diagram of MWP system [34].

opto-electrical (OE) stages [36]. These photonic processing features provide added value in real-world RF applications by leveraging the inherent advantages of photonics—such as low transmission loss, broad bandwidth, EMI immunity, reconfigurability, and wide frequency tuning.

In recent years, As I mentioned, there has been a significant effort to integrate multiple photonic components and functions into a compact PIC, using CMOS-compatible technologies similar to those used for electronic ICs. This advancement has led to the development of integrated MWP, which allows multiple core MWP functions to be combined into a single, compact chip [26], [30]-[32], [37]. Key integrated MWP functionalities that have been demonstrated include RF filtering [38]-[41], delay lines [42]-[46], waveform generation [47]-[49], phase shifting [50]-[53], photonic analog-to-digital converters (ADCs) [54], [55], and beamforming [57]-[60]. For integrated MWP systems to become competitive with electronic solutions, they must deliver high levels of RF performance.

In MWP systems, electro-optical (EO) modulators play a crucial role in converting high-frequency electrical signals into the optical domain. Si photonics can be applied to demonstrate the EO modulators, and those are fabricated on Si PIC process. One of the most important characteristics of these devices is their linearity, as it has a significant impact on the overall system performance. In particular, the third-order intermodulation distortion (IMD3) and its effect on the spurious-free dynamic range (SFDR) are commonly used as key indicators to evaluate modulator performance.

Fig. 1-8(a) provides a simplified illustration of a MWP system employing a EO modulator, and Fig. 1-8(b) shows the power spectral density of the output microwave signal in this system, including both the fundamental and distortion

components. Distortion signals come in various forms, but among them, the IMD3, which appears closest in frequency to the fundamental signal, is the most critical. This is because, in practical applications, bandpass filters are often used to suppress distortion components and ensure linearity; however, IMD3 components are difficult to filter out due to their proximity to the fundamental signal.

Fig 1-9 illustrates the concept of SFDR, which can be derived from the power levels of the fundamental and IMD3 signals. When plotted on a dB scale, the power of the fundamental signal increases linearly with input microwave signal power (slope of 1), while the power of the IMD3 signal typically increases with a slope of 3. The output of an MWP system also includes a noise floor. As the input microwave power decreases, the IMD3 power may fall below the noise floor, and with further reduction, even the fundamental signal may become buried in noise. The range of microwave power over which only the fundamental signal is visible above the noise floor (while IMD3 remains hidden) defines the SFDR. Conversely, as the input microwave power increases, there comes a point where the IMD3 power equals the fundamental power. This point is referred to as the third-order intercept point (IP3), and the corresponding output power is known as the power of output IP3 (P_{OIP3}).

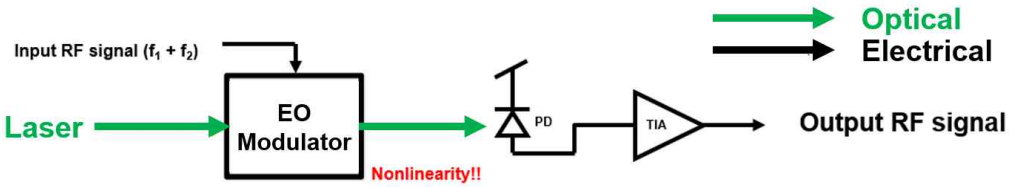

(a)

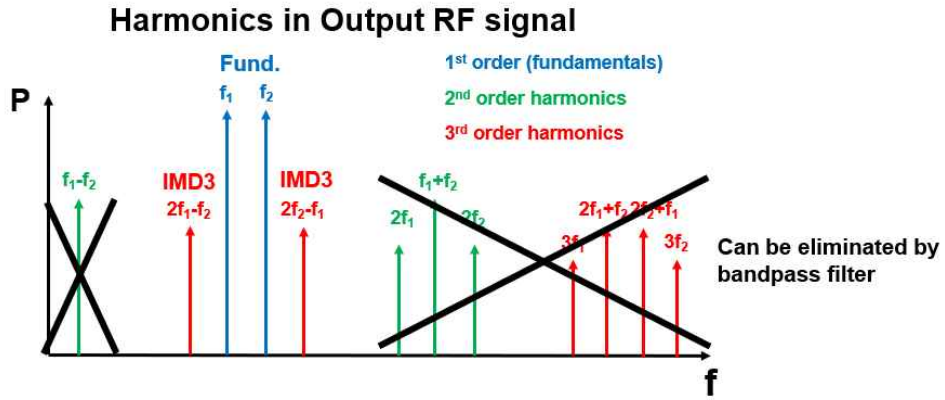

(b)

Fig. 1-8. (a) MWP system using EO modulators and (b) spectrum of output RF signal.

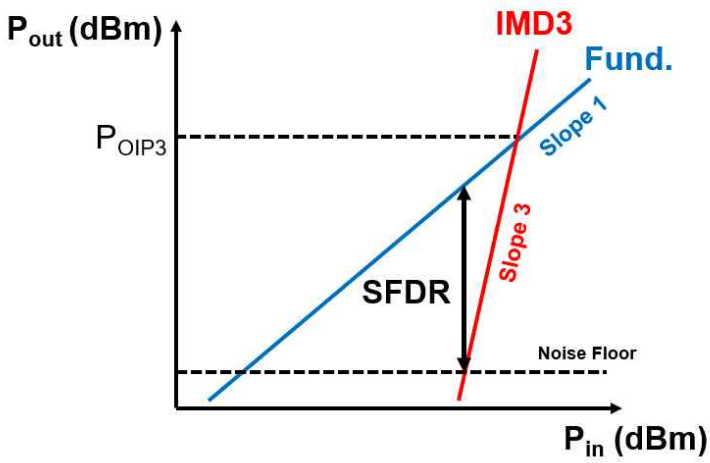

Fig. 1-9. Output RF power along input RF power and its SFDR.

1.4. Effects of Linearity on MWP System Performance

The linearity metric, SFDR, significantly impacts the performance of various MWP applications. This influence becomes especially prominent in the case of photonic ADC, an example of the MWP application, which utilize optical signals to convert analog signals into the digital domain [54], [55]. The photonic ADC is one of the critical device for military radars and communication systems using MWP.

The overall performance of any ADC is a composite measure of its resolution, noise floor, and linearity. While ideal N-bit resolution suggests a theoretical signal-to-noise ratio (SNR), the effective performance is quantified by the signal-to-noise and distortion ratio (SINAD) and its derivative, the effective number of bits (ENOB). Among the factors that degrade performance from the ideal, the non-linearity of the converter plays a critical role. This non-linearity is most precisely captured by the SFDR, a metric that quantifies the relationship between the desired signal and the largest undesired artifact.

SFDR is defined as the ratio between the power of the fundamental input signal and the power of the largest spurious component observed in the output spectrum. A high SFDR value signifies a highly linear converter, indicating that distortion products are very low relative to the signal. Conversely, a low SFDR indicates significant non-linearity, where spurious signals are relatively strong.

The link between SFDR and overall performance is established through SINAD. The SINAD metric, by definition, includes all noise and distortion components within the band of interest. Its formula can be expressed as [56]:

$$SINAD\ (\text{dB}) = 10\log_{10}\left(\frac{P_{Signal}}{P_{Noise} + P_{Distortion}}\right). \tag{1.1}$$

$P_{Distortion}$ epresents the summed power of all harmonic and spurious components. The SFDR of MWP system can be measured by identifying the fundamental signal power P_{signal} at carrier frequency and the largest spurious signal power $P_{Distortion}$ such as IMD3. Therefore, a poor SFDR directly and significantly increases the $P_{Distortion}$ term, which in turn degrades the overall SINAD.

Crucially, SFDR often sets the ceiling for dynamic performance of ADCs. The SINAD value will always be limited by the larger of the total noise P_{Noise} and the total distortion $P_{Distortion}$. In a "distortion-limited" scenario—common in high-resolution ADCs where quantization noise is very low—the $P_{Distortion}$ term dominates. In this case, the SINAD can be no better than the SFDR (SINAD ≤ SFDR).

This performance degradation is ultimately reflected in the ENOB, which is a direct conversion of the SINAD value back into a measure of resolution with following equation [56].

$$ENOB = \frac{SINAD - 1.76\ \text{dB}}{6.02} \tag{1.2}$$

In conclusion, SFDR is not merely an isolated specification; it is a fundamental limiter of effective precision of ADCs. It directly governs the distortion component of SINAD. Achieving a high ENOB is impossible without first ensuring a high SFDR. In applications demanding high fidelity and dynamic range, such as in

telecommunications, radar, and precision instrumentation, SFDR is a primary specification that dictates the true performance boundary of the entire system.

For the same reasons articulated above, the SFDR of a photonic ADC—which is often limited by the non-linearity of the electro-optic (EO) modulator at its front end—has a profound impact on its overall performance. Therefore, characterizing, optimizing, and enhancing the SFDR of EO modulators is essential for the accurate prediction and optimization of performance, such as ENOB. Through this dissertation, I intend to not only establish an accurate linearity simulation model for EO modulators but also to implement and experimentally demonstrate an advanced modulator structure designed to achieve a higher SFDR.

1.5. Research Goals

EO modulators used in MWP systems can be implemented using Si photonics technology, which offers high integration density and low fabrication cost. These EO modulators must not only support high-speed operation but also exhibit high linearity. However, unlike other types of EO modulators, Si-based modulators often suffer from poor linearity due to the effects of PN junctions. The PN junctions inside a Si EO modulator play a critical role: they induce a phase shift in the propagating optical signal in response to an electrical signal, thereby modulating the output. However, the phase shift induced by the PN junction is inherently nonlinear with respect to the applied voltage, which degrades the linearity of the device [61], [62].

To achieve high-linearity MWP systems, various techniques have been proposed to compensate for the nonlinearity of Si EO modulators. One such method involves electronic techniques. Fig. 1-10 shows a schematic of an MWP system using a Si MZM, where an electronic pre-distortion technique is applied to the input RF signal to reduce the nonlinearity in the output optical signal [63]. By intentionally adding distortion components to the RF signal before it enters the Si MZM, the inherent distortion generated by the modulator can be effectively canceled out. Similarly, as shown in Fig. 1-11, a linearization method using a low-noise amplifier and a second-order intermodulation generator has also been proposed, in which the pre-distorted RF signal is applied to segmented PN junctions within the Si MZM [64].

However, electronic linearization techniques often suffer from high power consumption and are inherently narrowband, making them unsuitable for broadband

photonic systems. Therefore, it is essential to design EO modulators with inherently high linearity to enable high-performance MWP systems. Additionally, developing an accurate simulation model that characterizes the modulator's linearity is critical, as it can guide the design and optimization of modulators with improved performance.

In this dissertation, we present a study on a modeling approach to characterize the linearity of EO modulators, along with the design and fabrication of a compact EO modulator optimized for high linearity. The results demonstrate the effectiveness of the proposed approach.

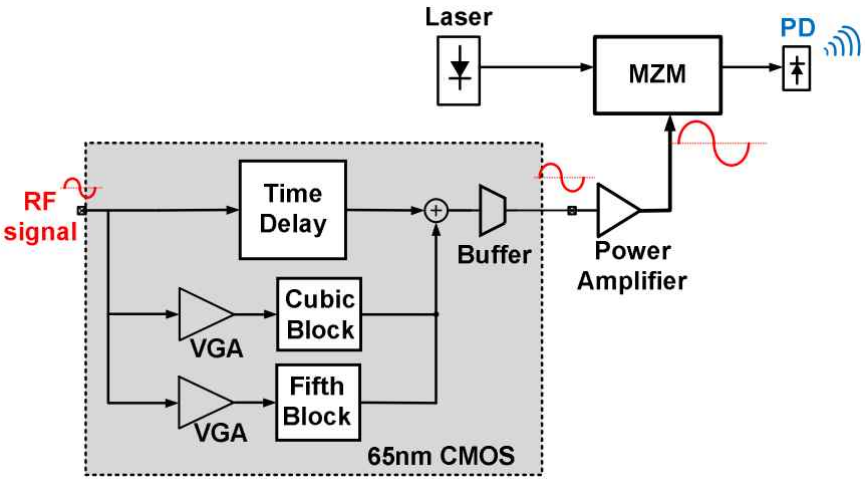

Fig. 1-10. MZM linearization with predistortion circuit [63].

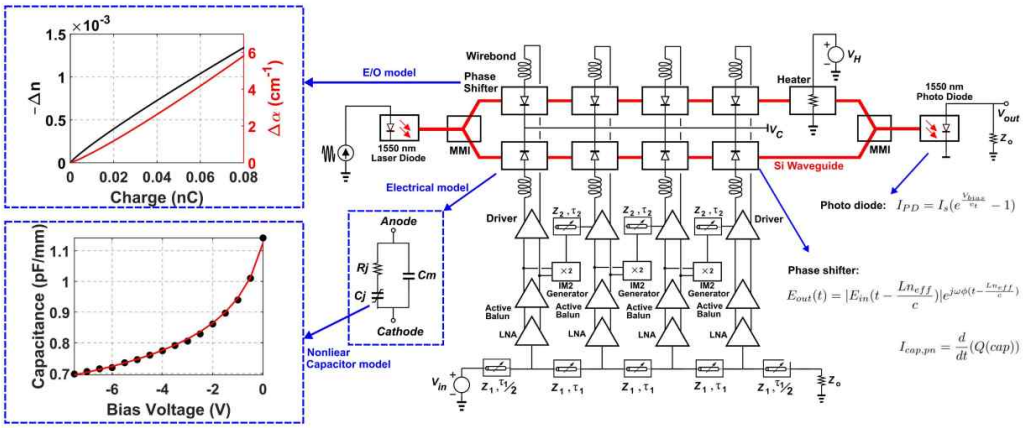

Fig. 1-11. MZM linearization with low-noise amplifier and second-order intermodulation generator [64].

1.6. Outline of Dissertation

This dissertation focuses on various Si EO modulators that can be used in MWP systems. The main contributions of this work are twofold: first, the development of a characterization model capable of evaluating the linearity of EO modulators used in MWP systems; and second, the design and fabrication of a Si EO modulator with enhanced linearity. Si EO modulators come in several forms, including Mach-Zehnder modulators (MZMs), ring modulators (RMs), and ring-assisted Mach-Zehnder modulators (RAMZM), which combine features of both MZMs and RMs.

Chapter 2 of this dissertation introduces the characteristics of Si MZMs and proposes a linearity characterization model for these devices. A Si MZM consists of PN-junction-based phase shifters and traveling-wave electrodes with metal lines. To accurately model the behavior of the Si MZM, the proposed model incorporates numerical equations that describe optical properties as well as transmission line theory. The model is validated experimentally using a fabricated sample Si MZM.

Chapter 3 presents the design and experimental characterization of a RAMZM, which is developed to achieve higher linearity. The RAMZM has a unique structure in which each arm of the MZI contains a ring modulator. This configuration leads to a distinct transmission characteristic that differs from conventional MZMs and contributes to improvements in both modulation efficiency and linearity. The fabricated RAMZM demonstrates high linearity even for RF signals in the X-band, above 10 GHz.

Finally, chapter 4 and 5 provide discussions and conclusion.

2. Si Mach-Zehnder Modulators (MZMs)[1)]

2.1. Structure

Si MZMs are the most widely used EO modulators based on Si photonics. While primarily utilizing Si, additional materials such as $LiNbO_3$ or III-V compounds can be incorporated to enhance modulation efficiency and reduce optical loss. The MZMs are based on a Mach-Zehnder interferometer (MZI) structure, as illustrated in Fig. 2-1.

An MZI consists of two arm waveguides. At the front end, a splitter divides the incoming optical signal into two paths, and at the back end, a coupler recombines the signals propagating through each arm. Depending on the phase difference between the two optical signals at the output, constructive or destructive

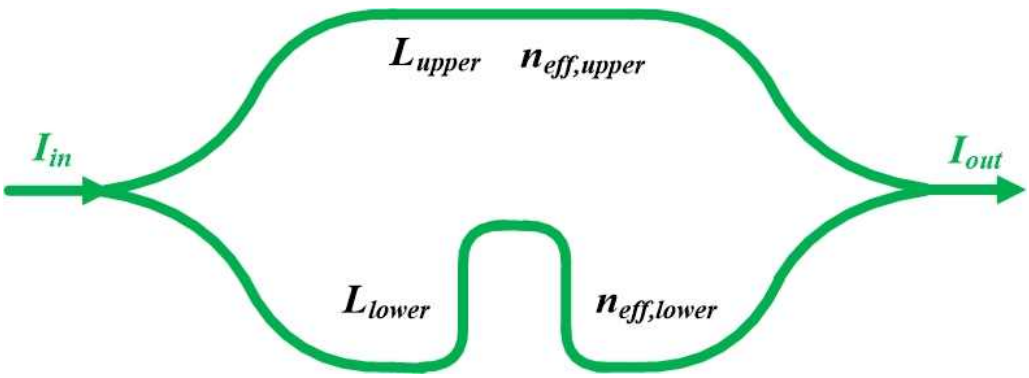

Fig. 2-1. Diagram of an MZI.

---

1) © IEEE & Optica Publishing Group. Reprinted with permission from "Min-Hyeok Seong *et al.*, 'Modulation lnearity characterization of Si Mach-Zehnder modulators,' *Journal of Lightwave Technology*, vol. 42, no. 6, march. 2024."

interference occurs, thereby modulating the output optical intensity. Assuming there is no optical loss in the waveguides, the output optical intensity of the MZI as a function of the input intensity can be expressed as following equation.

$$I_{out} = \frac{I_{in}}{2}[1 + \cos(\frac{2\pi n_{eff,upper}}{\lambda} L_{upper} - \frac{2\pi n_{eff,lower}}{\lambda} L_{lower})] \quad (2.1)$$

Here, $n_{eff,upper}$ and $n_{eff,lower}$ are the effective refractive indices of the upper and lower arm waveguides, and L_{upper} and L_{lower} are their respective lengths. A difference in $n_{eff}L$ between the two arms introduces a phase difference, which in turn causes interference at the coupler and modulates the output intensity.

With a fixed wavelength, the output intensity of the MZI varies depending on the phase difference between the two arms. Thus, MZIs are widely used in applications such as optical filters and switches [65]-[67]. However, when used for electro-optic modulation, the most practical approach to modulating output intensity is to vary the effective refractive index. In conventional $LiNbO_3$-based MZMs, this is achieved using the Pockels effect [68], which offers strong electro-optic behavior with high linearity and wide modulation bandwidth. However, Si does not exhibit the Pockels effect, so modulation in Si MZIs relies primarily on the plasma dispersion effect [69]. This effect is induced by embedding PN junction phase shifters in the arm waveguides of the Si MZM.

On top of the PN junctions in a Si MZM, there are metal layers that guide the propagating microwave signals. These metal lines deliver the RF signals to the PN junction phase shifters. The length of these lines typically exceeds 1 mm, depending on the length of the phase shifter. Due to their extended length, analysis of these structures requires transmission line theory. The combination of

metal lines and PN junction phase shifters is referred to as a TWE. Since the TWE significantly affects both the EO bandwidth and the linearity of the Si MZM, it is a critical component of the device.

Fig. 2-2 illustrates the full diagram of a Si MZM, including the PN junction phase shifters and TWE. When microwave signals are applied to each arm, the electrodes deliver the RF signals to the phase shifters, inducing a phase change in the optical signal. To achieve high bandwidth operation, the characteristic impedance of the traveling-wave electrode should be designed to match 50 Ω, and a 50 Ω termination resistor should be added at the end of the electrode to minimize microwave signal reflection. A more detailed discussion of each component is provided in chapter 2.2.

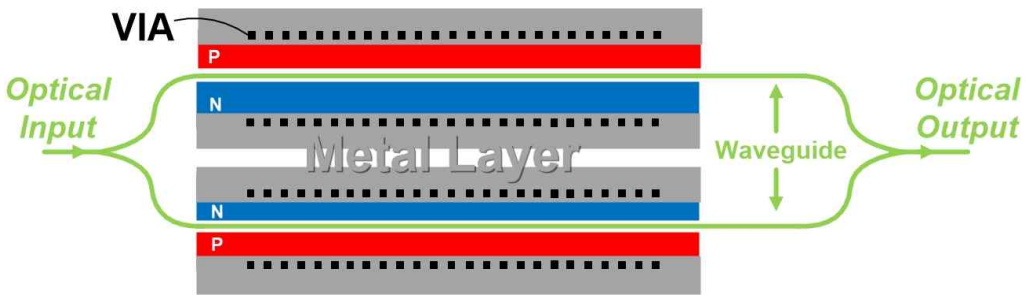

Fig. 2-2. Diagram of a Si MZM.

2.2. Characteristics

2.2.1 PN Junction Phase Shifter

The PN junction phase shifter in a Si MZM induces changes in the effective index and optical absorption of the Si waveguide, depending on the applied bias voltage. This phenomenon is referred to as the plasma dispersion effect, as discussed in this chapter. When a bias voltage is applied to the PN junction, it alters the carrier concentration, which in turn modifies optical properties of the waveguide—specifically, its effective refractive index and optical absorption. This behavior is described by the following equations [69].

$$-\Delta n = 5.40\times10^{-21}\Delta N^{1.167} + 5.84\times10^{-20}\Delta P^{1.109} \tag{2.2}$$

$$\Delta a[\mathrm{cm}^{-1}] = 8.88\times10^{-21}\Delta N^{1.167} + 5.84\times10^{-20}\Delta P^{1.109} \tag{2.3}$$

In the above equations, Δn and Δa represent the changes in the waveguide's refractive index and optical loss, respectively. ΔN and ΔP refer to the changes in electron and hole carrier densities.

A p-n junction is formed by adjoining a p-type semiconductor, characterized by an acceptor doping concentration N_A, and an n-type semiconductor with a donor concentration N_D. At thermal equilibrium, in the absence of an external voltage, a potential difference known as the built-in potential (ϕ_i) arises due to differences in the work functions of the p- and n-type materials. This potential is expressed as [70]:

$$\phi_i = \frac{kT}{q} \ln \frac{N_A N_D}{n_i}, \tag{2.4}$$

where n_i is the intrinsic carrier concentration, k is Boltzmann's constant, T is the absolute temperature, and q is the elementary charge.

When a bias voltage is applied across the junction:

- A forward bias (positive voltage to the p-type region) reduces the potential barrier and narrows the depletion region.
- A reverse bias (negative voltage to the p-type region) increases the barrier and widens the depletion region.

the total potential ϕ difference across the junction becomes [70]

$$\phi = \phi_i - V_a. \tag{2.5}$$

V_a is applied voltage to PN junction. Both forward and reverse voltage are describes in Fig 2-3 [71].

Under the abrupt junction approximation, the depletion region is assumed to have a well-defined boundary with a sharp transition to the quasi-neutral region, where the electric field is negligible and carrier concentration approximates the doping levels. The total depletion width x_d consists of contributions from the p-side (x_p) and the n-side (x_n), and that is given by

$$x_d = x_n + x_p. \tag{2.6}$$

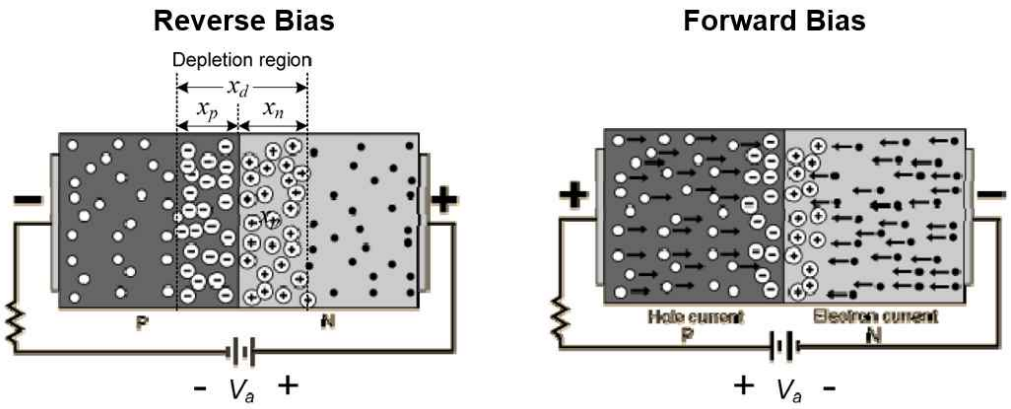

Fig. 2-3. Reverse and forward bias of PN junction [71].

Charge neutrality in the depletion region requires the total negative charge in the p-side to equal the total positive charge in the n-side. Therefore,

$$N_D x_n = N_A x_p. \tag{2.7}$$

Combining (2.6) with (2.7) yields the individual widths, and those are

$$x_n = x_d \frac{N_A}{N_A + N_D}, \tag{2.8}$$

$$x_p = x_d \frac{N_D}{N_A + N_D}. \tag{2.9}$$

The relationship between the depletion widths and the total electrostatic potential gives as following equation [70].

$$\phi_i - V_a = \frac{qN_D x_n^2 + qN_A x_p^2}{2\varepsilon} \tag{2.10}$$

In (2.10), ε is the permittivity.

Substituting the expressions for x_n and x_p, (2.8) and (2.9), into (2.10) yields the total depletion width:

$$x_d = \sqrt{\frac{2\varepsilon}{q}\left(\frac{1}{N_A}+\frac{1}{N_D}\right)(\phi_i - V_a)}. \tag{2.11}$$

From this, the individual depletion regions are

$$x_n = \sqrt{\frac{2\varepsilon}{q}\frac{N_A}{N_D(N_A+N_D)}(\phi_i - V_a)}, \tag{2.12}$$

$$x_p = \sqrt{\frac{2\varepsilon}{q}\frac{N_D}{N_A(N_A+N_D)}(\phi_i - V_a)}. \tag{2.13}$$

When a bias voltage is applied to the PN junction, the width of the depletion region changes, thereby altering the doping concentration within the PN junction waveguide. Depending on the polarity of the applied voltage, the PN junction can be either forward-biased or reverse-biased. In the case of forward bias, the depletion region narrows, leading to a decrease in both Δn and Δa. Conversely, under reverse bias, the depletion region widens, reducing the carrier concentration in the PN junction, which results in an increase in Δn and Δa. Since the depletion width changes with the square root of the applied voltage, this voltage-dependent behavior introduces nonlinearity in the Si MZM.

A Si MZM that operates under forward bias is referred to as a carrier-injection-type MZM, while one that uses reverse bias is called a depletion-type MZM. The carrier-injection type offers high modulation efficiency,

but due to its large junction capacitance, it typically suffers from limited EO bandwidth [72]. On the other hand, the depletion-type MZM provides lower modulation efficiency but supports higher EO modulation bandwidth, making it more suitable for high-speed applications.

Despite the high-speed capability of depletion-type MZMs, achieving destructive interference between optical signals requires a significant phase shift. This means that either a large peak-to-peak voltage must be applied or the MZM must have a long arm length. The modulation efficiency of an MZM is commonly represented by the $V_{\pi}L$ product, which is the product of the voltage required for a π phase shift and the modulator arm length. A smaller $V_{\pi}L$ value indicates a more efficient modulator. In recently reported Si photonic MZMs, $V_{\pi}L$ values range from 0.74 V·cm [73] to 11 V·cm [74]. For example, achieving a 2-V peak-to-peak drive voltage to get π shift may typically require a modulator length of 3.7 mm at least, resulting in a device footprint on the order of several millimeters.

2.2.2 Traveling-Wave Electrode (TWE)

The TWE of a Si MZM consists of a metal line positioned above the PN junction. The TWE serves as a transmission line through which the microwave signal propagates. As discussed in chapter 2.2.1, when attempting to drive the Si MZM with a low peak-to-peak voltage, the PN phase shifter must inherently be long to achieve the required phase shift. Consequently, the TWE is also long and thus must be analyzed using transmission line theory to accurately model the behavior of the microwave signal.

The core principle of the TWE design is that the presence of distributed capacitance does not inherently limit the modulation speed. By appropriately engineering the electrode and waveguide structure, it is possible to match the propagation velocities of the optical and electrical signals. This velocity matching ensures that phase modulation accumulates consistently along the device length, independent of modulation frequency.

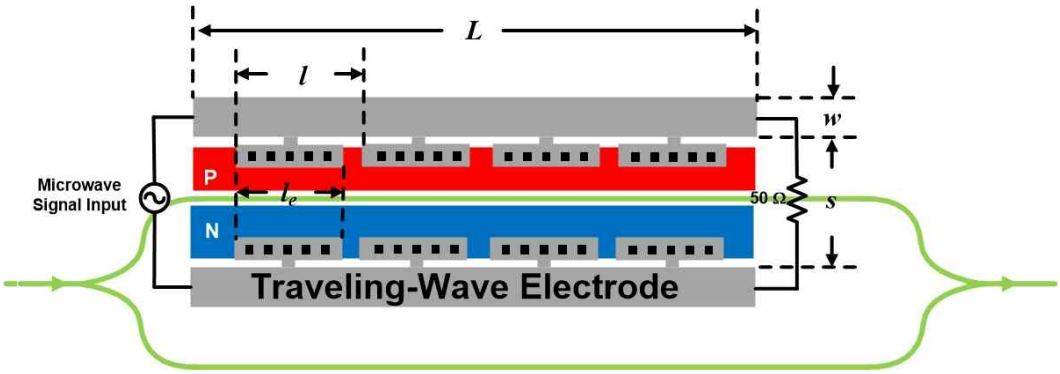

Fig. 2-4. Diagram of an example of TWE in a Si MZM.

In a TWE-based MZM, the central modulation electrodes—which interact with the optical signal beneath them—are segmented into multiple small units. Each segment can be approximated as a lumped capacitance, and these are periodically connected to the outer traveling-wave electrodes.

As depicted in Fig. 2-4 as an example, the complete TWE of Si MZM is flanked by two broad signal lines, forming a coplanar stripline (CPS) configuration. These electrodes have a defined width (w), length (L), and gap (s) between them. Along the optical waveguides, lumped phase modulation electrodes are periodically arranged with a spacing of l, and are electrically connected to the CPS electrodes through air-bridge structures.

Each of these inner modulation electrodes, with a length of l_e, is placed atop PN junction structures. These junctions are spaced and configured as individual diodes to facilitate efficient EO interaction, as illustrated in Fig. 2-5.

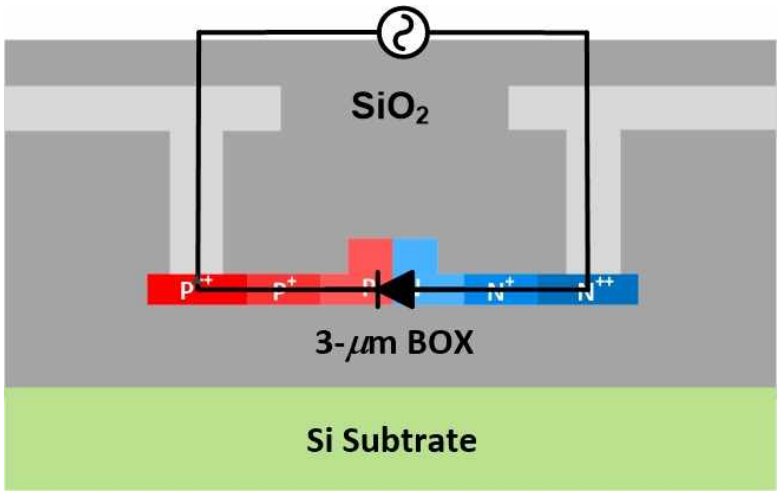

Fig. 2-5. Cross-section of the TWE in a Si MZM.

The microwave behavior of a TWE MZM can be effectively modeled using a loaded transmission line approach. In this model, the active modulation electrodes serve as periodic capacitive loads along the segmented transmission line—an approach as discussed.

Here, the metal of the TWE itself functions as an unloaded transmission line, which is electrically characterized by the following per-unit-length parameters: resistance R_0, inductance L_0, conductance G_0, and capacitance C_0.

For the low-loss approximation, where signal attenuation is negligible, R_0 and G_0 can be assumed to be zero. Under this condition, the characteristic impedance Z_0 and the microwave refractive index n_{mw} of the unloaded line are given by

$$Z_0 = \sqrt{\frac{L_0}{C_0}}, \tag{2.14}$$

$$n_{mw} = c \cdot \sqrt{L_0 \cdot C_0}, \tag{2.15}$$

where c is the speed of light in vacuum.

When capacitive loading is introduced—represented by a load capacitance per unit length C_L—the loaded line exhibits modified characteristics. Its characteristic impedance Z and effective microwave index n_{mw}' are then expressed as [75]

$$Z = \sqrt{\frac{L_0}{C_0 + C_L}}, \tag{2.16}$$

$$n_{mw}' = c \cdot \sqrt{L_0 \cdot (C_0 + C_L)}. \tag{2.17}$$

To achieve velocity matching, a key design objective in TWE MZMs, the effective microwave index n_{mw}' must be equal to the optical group index n_o. Enforcing $n_{mw}' = n_o$, we can solve for the required inductance per unit length L_0 as

$$L_0 = \frac{n_{mw}' \cdot Z}{c} = \frac{n_o \cdot Z}{c}. \tag{2.18}$$

Moreover, (2.16) and (2.17) imply that the total capacitance per unit length of the loaded line must satisfy

$$C_L + C_0 = \frac{n_{mw}'}{c \cdot Z} = \frac{n_o}{c \cdot Z}. \tag{2.19}$$

By combining relations from (2.14) to (2.17), the values of the unloaded line capacitance C_0 and the load capacitance C_L can be determined as follows:

$$C_0 = \frac{n_{mw}^2}{c \cdot Z \cdot n_o}, \tag{2.20}$$

$$C_L = \frac{n_o^2 - n_{mw}^2}{c \cdot Z \cdot n_o}. \tag{2.21}$$

Additionally, a useful relation linking the loaded and unloaded parameters—specifically Z, Z_0, n_{mw} and n_{mw}'—is given by

$$n_{mw} \cdot Z_0 = n_{mw}' \cdot Z. \tag{2.22}$$

C_L of Si MZM is derived from junction capacitance C_J of PN junction shifters. When the applied voltage varies, the stored charge within the depletion region changes accordingly, giving rise to a junction capacitance, which must be included in the equivalent circuit model. The junction capacitance versus the applied voltage is defined as:

$$C_J(V_a) = \left| \frac{dQ(V_a)}{dV_a} \right|. \tag{2.23}$$

Q is the charge in the PN junction. Using (2.12), the depletion width expression for the n-side, and the relation $Q = qN_Dx_n$, (2.23) becomes [75]

$$C_J = \sqrt{\frac{q\varepsilon}{2(\phi_i - V_a)} \frac{N_A N_D}{N_A + N_D}}. \tag{2.24}$$

This expression resembles that of a parallel-plate capacitor:

$$C_J = \frac{\varepsilon}{x_d}. \tag{2.25}$$

However, unlike an ideal parallel-plate capacitor, the depletion width is voltage-dependent, which makes the junction capacitance a nonlinear function of the applied voltage. Often, the voltage-dependent capacitance is referenced to its zero-bias value, C_{J0}, as [75]

$$C_J(V_a) = \frac{C_{J0}}{\sqrt{1 - \frac{V_a}{\phi_i}}}. \tag{2.26}$$

This functional form is particularly useful in extracting the doping concentration and built-in potential from C–V measurements. Taking the derivative yields:

$$\frac{d(\frac{1}{C_J^2})}{dV_a} = -\frac{2}{q\varepsilon}\frac{N_A + N_D}{N_A N_D}. \tag{2.27}$$

Plotting $1/C_J^2$ versus V_a results in a straight line whose slope provides the doping concentration, and whose x-intercept reveals the built-in potential.

2.2.3 EO Bandwidth of Si TWE MZMs

EO Bandwidth is a critical performance metric that determines the quality and responsiveness of an EO modulator. For a TWE MZM, the EO bandwidth is defined as the frequency at which the modulation depth of the optical intensity decreases to 70.7% of its reference (low-frequency) value, corresponding to a 3-dB drop in the received signal power [75].

In EO modulation, the accumulated phase shift experienced by an optical signal as it propagates through the waveguide is linearly dependent on the applied voltage. The proportionality constant is influenced by several parameters, including the geometrical dimensions of the waveguide, the optical wavelength, the refractive index, the EO coefficient, and the degree of spatial overlap between the optical and microwave fields.

Because the applied voltage travels along the device in the form of a traveling wave, the total phase modulation acquired by a photon is the integrated effect of the instantaneous voltages encountered along the propagation path. This cumulative modulation is position-dependent, governed by the local interaction between the optical and microwave signals.

A simplified equivalent circuit model of the TWE MZM is illustrated in Fig. 2-6, where the entire modulator is electrically modeled as a transmission line. This representation facilitates the analysis of signal propagation, impedance matching, and bandwidth performance in the high-frequency domain.

In the model, the sinusoidal voltage modulating the TWE MZM at position x with angular frequency ω can be expressed as [76]-[77]

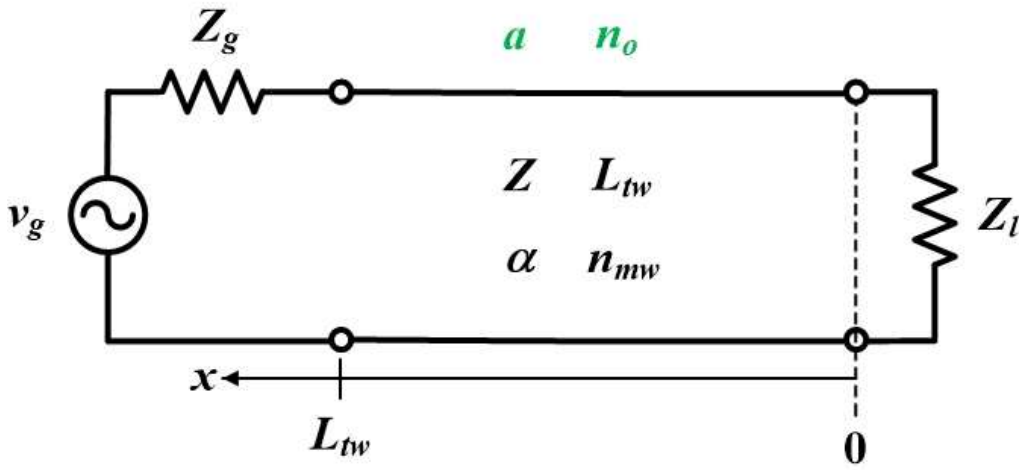

Fig. 2-6. A simplified equivalent circuit of Si TWE MZM.

$$v(x,\omega)=\frac{v_g}{2}(1+\Gamma_g(\omega))e^{j\beta_s(\omega)L_w}\cdot\frac{e^{(j\beta_s(\omega)-j\beta_a(\omega))L_w}+\Gamma_l(\omega)\cdot e^{-(j\beta_s(\omega)-j\beta_a(\omega))L_w}}{e^{j\beta_s(\omega)L_w}+\Gamma_g(\omega)\cdot\Gamma_l(\omega)\cdot e^{-j\beta_s(\omega)L_w}} \quad (2.28)$$

In (2.28), the parameters are given as

$$\Gamma_g(\omega)=\frac{Z(\omega)-Z_g}{Z(\omega)+Z_g}, \quad (2.29)$$

$$\Gamma_l(\omega)=\frac{Z_l-Z(\omega)}{Z_l+Z(\omega)}, \quad (2.30)$$

$$\beta_o=\frac{\omega}{c}n_o, \quad (2.31)$$

$$\beta_e(\omega)=-j\alpha(\omega)+\frac{\omega}{c}n_{mw}(\omega). \quad (2.32)$$

The meaning of the variables in equations from (2.29) to (2.32) is defined as follows:

v_g is the amplitude of the input sinusoidal voltage,

L_{tw} is the TWE length,

Γ_g is the reflection coefficient at RF source,

Γ_l is the reflection coefficient at the termination load,

Z is the characteristic impedance of the TWE,

Z_g is the source impedance, normally is 50 Ω,

Z_l is the impedance of the termination load,

α is the microwave attenuation constant,

β_e is the microwave propagation constant,

β_o is the optical propagation constant in the waveguide,

n_{mw} is the microwave refractive index,

n_o is the optical group index,

c is the velocity of light in vacuum.

Under small-signal modulation conditions, the optical modulation depth is linearly proportional to the applied modulating voltage. In this regime, a modulation reduction factor, denoted as $r(x,\omega)$ can be introduced to quantify the degradation in modulation efficiency along the device length at modulation frequency ω, and that is

$$r(x,\omega) = \left| \frac{v(x,\omega)}{v(L_{tw},0)} \right|. \tag{2.33}$$

The EO bandwidth of the TWE MZM, as previously defined, corresponds to the frequency at which the modulation reduction factor decreases to 70.7% of its

low-frequency value—i.e., a 3-dB drop in intensity modulation depth. Mathematically, this can be expressed as

$$r(\omega) = \frac{1}{\sqrt{2}}. \tag{2.34}$$

To simplify the analysis, the position-dependent voltage $v(x,\omega)$ is replaced by its average value $v_{avg}(\omega)$ along the modulator length L_{tw}. This allows the modulation reduction factor to be approximated in a simplified form as:

$$r(\omega) = \left| \frac{v_{avg}(\omega)}{v_{avg}(0)} \right|. \tag{2.35}$$

Here, $v_{avg}(\omega)$ is defined as the average voltage along the modulation length and can be expressed as [76]-[78]

$$v_{avg}(\omega) = \frac{1}{L_{tw}} \cdot \int_0^{L_{tw}} v(x,\omega) dx = \frac{v_g \cdot (1+\Gamma_g(\omega)) \cdot e^{j\beta_o(\omega)L_{tw}}}{2 \cdot (e^{j\beta_e(\omega)L_{tw}} + \Gamma_g \cdot \Gamma_l \cdot e^{-j\beta_e(\omega)L_{tw}})} \cdot (V_+(\omega) + \Gamma_l(\omega) \cdot V_-(\omega)) \tag{2.36}$$

In (2.36), V_+ and V_- are

$$V_\pm = e^{\pm j\phi_\pm} \cdot \frac{\sin\phi_\pm}{\phi_\pm}. \tag{2.37}$$

V_+ is the average voltage applied to a photon by the forward traveling wave. V_- is the average voltage applied to a photon by the reverse traveling wave. $\phi_\pm$ is

$$\phi_\pm = \frac{\beta_e \mp \beta_o}{2} L_{tw}. \tag{2.38}$$

$\phi_{\pm}$ represents the complex phase shift accumulated between the microwave and optical waves as the microwave signal propagates forward and backward along the length of the TWE. This approximation is particularly useful for analytically or numerically estimating the bandwidth performance without solving the full transmission line equations along the modulator.

Furthermore, Si TWE MZM in this research has series resistance (R_s) and junction capacitance (C_J) in PN junction. For deriving EO S21 of Si TWE MZM, the effect of these components should be added. Therefore, EO S21 of the Si TWE MZM is given as [78]

$$S_{21.EO}(\omega) = \frac{1}{\sqrt{(\omega R_s C_J)^2 + 1}} \cdot \left| \frac{v_{avg}(\omega)}{v_{avg}(0)} \right| . \tag{2.39}$$

There is the critical point that EO bandwidth is influenced by impedance mismatch; microwave loss; junction resistance and capacitance; and the velocity mismatch between optical and electrical signal.

If there is no effect of R_sC_J and the TWE has a perfectly matched line, which is $Z = Z_g = Z_l = 50\ \Omega$ and $\Gamma_g = \Gamma_l = 0$, (2.35) can be reduced to the expression of

$$r(\omega) = e^{\frac{-\alpha L_{tw}}{2}} \cdot \left| \frac{\sin \phi_+}{\phi_+} \right|, \tag{2.40}$$

$$\phi_+ = \frac{\beta_e - \beta_o}{2} L_{tw} = \frac{L_{tw}}{2} \cdot \left[\frac{\omega}{c} (n_{mw} - n_o) - j\alpha \right] = \frac{\pi \cdot f \cdot L_{tw}(n_{mw} - n_o)}{c} - j \cdot \frac{\alpha \cdot L_{tw}}{2} \tag{2.41}$$

Additionally, if microwave loss does not exist, which is $\alpha = 0$, (2.40) becomes

$$r(\omega) = \left| \frac{\sin \phi_+}{\phi_+} \right| = \left| \frac{\sin \Theta}{\Theta} \right|, \tag{2.42}$$

$$\Theta = \frac{\pi \cdot f \cdot L_{tw} \cdot (n_{mw} - n_o)}{c}. \tag{2.43}$$

Substituting (2.42) into (2.34), Equation of 3-dB EO bandwidth is

$$f_{3dB.EO} \approx \frac{1.39c}{\pi L_{tw}(n_{mw} - n_o)} \tag{2.43}$$

The equation is an expression that describes the relationship between modulation bandwidth and velocity mismatch between the optical and microwave signals. It is important to emphasize that this relation is derived under the assumptions of a characteristic impedance of 50 Ω for the device and negligible microwave propagation loss throughout the entire electrode structure.

If the condition $n_{wm} = n_o$, that velocities of both microwave and optical signal are matched, is added, (2.40) is modified to

$$r(\omega) = e^{\frac{-\alpha L_{tw}}{2}} \cdot \left| \frac{\sin(\frac{-j\alpha L_{tw}}{2})}{\frac{-j\alpha L_{tw}}{2}} \right|. \tag{2.45}$$

By Euler's formula (additional explanation in appendix A), (2.45) can be revised to

$$r(\omega) = \frac{1 - e^{-\alpha L_{tw}}}{\alpha L_{tw}}. \tag{2.46}$$

By substituting (2.46) into (2.34), we obtain the condition under which the optical intensity modulation depth drops to 70.7% of its low-frequency value (i.e., a 3-dB decrease in modulation response):

$$\alpha L_{tw} = 0.7384. \tag{2.47}$$

Under this condition, the corresponding electrical loss is calculated as follows:

$$20 \cdot \log\left|e^{-j\beta_e L_{tw}}\right| = 20 \cdot \log(e^{-\alpha L_{tw}}) = 20 \cdot \log(e^{-0.7384}) = -6.4 \text{ dB}. \tag{2.48}$$

Assuming perfect velocity and impedance matching, the EO 3-dB bandwidth can be accurately estimated by evaluating the electrical transmission loss (i.e., the S21 parameter). The frequency at which the electrical loss reaches –6.4 dB is identified as the 3-dB cut-off frequency of the modulator's EO response.

In practical modulators, microwave loss and velocity mismatch can be minimized through careful design, but cannot be entirely eliminated. Therefore, it is essential to evaluate the modulator’s frequency response while considering the combined effects of both microwave attenuation and phase velocity mismatch.

(2.40) is used for further analysis. So, $r(\omega)$ becomes [79]

$$r(\omega) = e^{-\alpha L_{tw}} \cdot \left|\frac{\sin\phi_+}{\phi_+}\right| = \left|e^{-\alpha L_{tw}} \cdot \frac{\sin\phi_+}{\phi_+}\right| = \left|\frac{1-e^{-(\alpha+j\beta_{mw-o})L_{tw}}}{(\alpha+j\beta_{mw-o})L_{tw}} \cdot e^{j\frac{\beta_{mw-o}L_{tw}}{2}}\right| = \frac{\sqrt{e^{-2\alpha L_{tw}} - 2e^{-\alpha L_{tw}} \cdot \cos(\beta_{mw-o}L_{tw}) + 1}}{\sqrt{(\alpha L_{tw})^2 + (\beta_{mw-o}L_{tw})^2}}, \tag{2.49}$$

where

$$\beta_{mw-o} = \frac{\omega}{c}(n_{mw} - n_o). \tag{2.50}$$

As indicated in (2.48), determining the modulation reduction factor $r(\omega)$ requires knowledge of both the product αL_{tw} and the term $\beta_{mw\text{-}o}$. Here, L_{tw} denotes the length of the TWE, α is the microwave attenuation constant—a frequency-dependent parameter that quantifies the microwave loss across the entire modulator—and $\beta_{mw\text{-}o}$, defined in (2.49), represents the velocity mismatch within the device.

In the context of a Si TWE MZM, the entire electrode structure, including both the outer electrodes and the periodic reverse-biased capacitive loads, can be treated as a microwave transmission line. Accordingly, the microwave loss coefficient α of the modulator corresponds to the attenuation constant of this transmission line. When combined with the scattering matrix description of the line, α can be expressed analytically as

$$\exp(-\alpha L_{tw}) = |S_{21}| \tag{2.51}$$

Therefore, $r(\omega)$ of (2.48) can be rewritten as

$$r(\omega) = \frac{\sqrt{|S_{21}|^2 - 2\cdot|S_{21}|\cdot\cos(\beta_{mw-o}L_{tw}) + 1}}{\sqrt{(\ln|S_{21}|)^2 + (\beta_{mw-o}L_{tw})^2}}. \tag{2.52}$$

Since the scattering parameters of the transmission line can be readily obtained using either electromagnetic (EM) simulation tools or network analyzer measurements, equation (2.51) provides a practical and powerful method for both

design validation and experimental characterization of the EO bandwidth of Si TWE MZMs.

2.3. Linearity Characterization

This dissertation develops a linearity model using the characteristics of the Si TWE MZM and equations discussed in chapter 2.2, and experimentally validates the model. The validated model is then used to analyze how different components of the Si TWE MZM affect its linearity.

2.3.1 Simulation Model

Recent research has investigated the linearity performance of Si MZMs through both simulations [80] and experimental measurements [81]. In addition, several design optimization strategies have been introduced to enhance the linearity of Si MZMs [82]-[84].

One commonly used approach for characterizing Si MZM linearity is the Taylor series expansion of the modulator's transfer function [80]. However, the mathematical complexity of this method often limits its practical applicability. In [85], closed-form expressions were derived for second- and third-order harmonic distortions, but the mismatch between theoretical predictions and measured results was not sufficiently addressed. Meanwhile, [86] identified the biasing conditions that yield the maximum SFDR for the Si MZM; however, it did not provide a predictive model for evaluating linearity performance across different operating conditions. The linearity model proposed in this study allows for numerical analysis by inputting model parameters into the equations, and it has the advantage of being compatible with user-friendly tools such as MATLAB or Python.

v_{avg} mentioned in chapter 2.2.3 represents the average voltage experienced by the optical signal propagating inside the Si TWE MZM. As the voltage propagates through the TWE, it varies with frequency due to impedance mismatch, velocity mismatch, and microwave loss. In the linearity model, this is captured using (2.36). Additionally, the voltage-dependent nonlinearity of the effective index of the Si PN junction waveguide, as well as the voltage-dependent nonlinearity of the junction capacitance, are also incorporated into the model.

Fig. 2-7 shows the complete diagram of the linearity model for the Si TWE MZM. When a two-tone sinusoidal signal $v_{in}(t)$, which has angular frequency near ω, is applied, as discussed in chapter 2.2.3, the voltage applied to the optical signal changes with frequency due to the properties of the TWE. The model uses the corresponding average voltage v_{avg}. If each tone of v_{in} has the amplitude v_g, the amplitude of v_{in} becomes $2v_g$. Also, (2.36) can be rewritten as the equation shown below.

$$v_{avg}(\omega) = \frac{v_g \cdot (1+\Gamma_g(\omega)) \cdot e^{j\beta_o(\omega)L_{tw}}}{e^{j\beta_e(\omega)L_{tw}} + \Gamma_g \cdot \Gamma_l \cdot e^{-j\beta_e(\omega)L_{tw}}} \cdot (V_+(\omega) + \Gamma_l(\omega) \cdot V_-(\omega)) \tag{2.53}$$

According to equation (2.53), v_{avg} is a function of ω. When $v_{in}(t)$ is modified by the effect of the TWE, the resulting signal is referred to as $v_{tw}(t)$, and the relationship between $v_{in}(t)$ and $v_{tw}(t)$ is given by the following equation.

$$v_{tw}(t) = v_{in}(t) \cdot \left| \frac{v_{avg}(\omega)}{v_{avg}(0)} \right| \tag{2.54}$$

This expression represents the input voltage $v_{in}(t)$ modified by a scaling factor resulting from the TW effect. As shown in (2.54), when the input signal

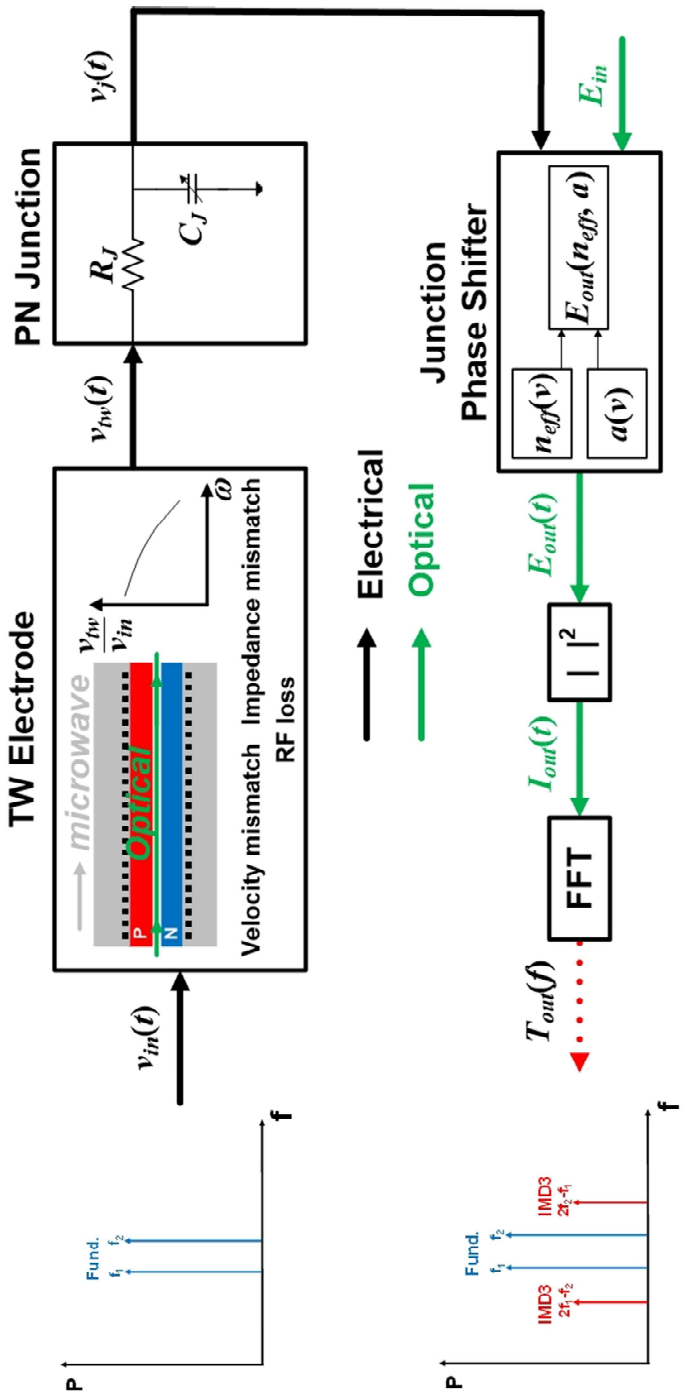

Fig. 2-7. Block diagram of the linearity simulation model of Si TWE MZM.

frequency ω is low, the TW effect is minimal and $v_{in}(t)$ is largely preserved. However, at higher frequencies, the voltage experienced by the optical signal can deviate substantially from the original input waveform due to propagation-related distortions.

As illustrated in Fig. 2-7, the voltage waveform after accounting for TW effects, v_{tw} is further shaped by the series resistance R_s and the voltage-dependent junction capacitance C_J of the Si waveguide. The resulting signal $v_j(t)$, which is the actual voltage applied across the PN junction of the doped Si waveguide, directly affects the effective refractive index $n_{eff}(v)$ and the optical absorption coefficient $a(v)$ through the plasma dispersion effect.

Electric field of output optical signal $E_{out}(t)$ in Fig. 2-7 can be represented by

$$E_{out} = \frac{1}{2} \cdot E_{in} \cdot \Big[j \cdot \exp(-a(v)L_m) \cdot \exp\big(-j\theta_1(v)\big) \cdot \exp(-j\phi) + \exp(-a(v)L_m) \cdot \exp\big(-j\theta_2(v)\big) \Big]. \tag{2.55}$$

θ_1 and θ_2 are phase shifts caused by propagation of optical signal on PN-doped Si waveguide of each arm. ϕ is initial phase difference between two arm waveguides. If v_j in Fig. 2-7 is applied to the Si TWE MZM with differential operation, $E_{out}(t)$ can be rewritten by

$$E_{out} = \frac{1}{2} \cdot E_{in} \cdot \left[j \cdot \exp(-a(-v_j/2)L_m) \cdot \exp\left(-j\frac{2\pi n_{eff}(-v_j/2)}{\lambda} L_m \right) \cdot \exp(-j\phi) + \exp(-a(v_j/2)L_m) \cdot \exp\left(-j\frac{2\pi n_{eff}(v_j/2)}{\lambda} L_m \right) \right]. \tag{2.56}$$

L_m represents PN junction length, and that is assumed to be equal to L_{tw}. As can be seen in (2.56), $n_{eff}(v)$ and $a(v)$ are changed with junction voltage $v_j(t)$, and that makes optical signal corresponding to input microwave signal. When E_{out} is squared, output optical intensity $I_{out}(t)$ can be driven, represented by

$$I_{out} = \frac{I_{in}}{4}\left[\exp(-2a(-v_j/2)L_m) + \exp(-2a(v_j/2)L_m) + 2\cos\left(\frac{2\pi n_{eff}(-v_j/2)}{\lambda}L_m - \frac{2\pi n_{eff}(v_j/2)}{\lambda}L_m + \phi\right)\right]. \tag{2.57}$$

(2.57) resembles (2.1), which is a basic transfer function of a Si MZM. To convert I_{out} into an electrical signal, the responsivity of the photodetector is applied, resulting in the output photocurrent. By performing Fast Fourier transform (FFT) on this current, the output power spectral density $T_{out}(f)$ is obtained, from which the fundamental and IMD3 signals of interest in this study can be extracted.

2.3.2 A Sample Si MZM

To verify the linearity model proposed in chapter 2.3.1, a sample Si MZM was fabricated using the multi-project wafer (MPW) service provided by Advanced Micro Foundry. The fabricated modulator was designed with a single push-pull Mach–Zehnder modulator (SPPMZM) structure [62], [87]. This SPPMZM employs series-connected PN junctions, which are known to reduce junction capacitance by half, thereby enabling EO bandwidth [62], [87]. In the fabricated device, the PN junctions are also connected in series, forming PNP-type junction phase shifters.

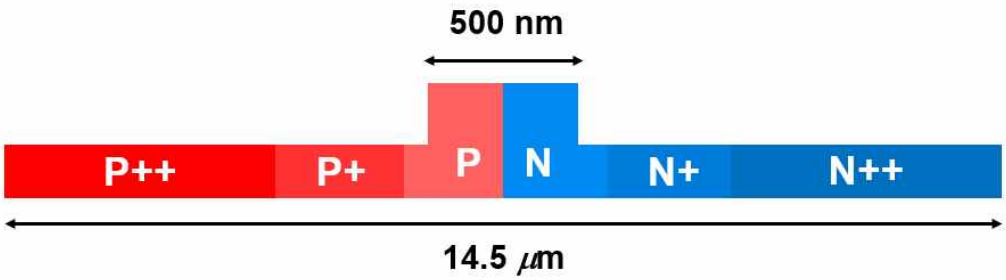

(a)

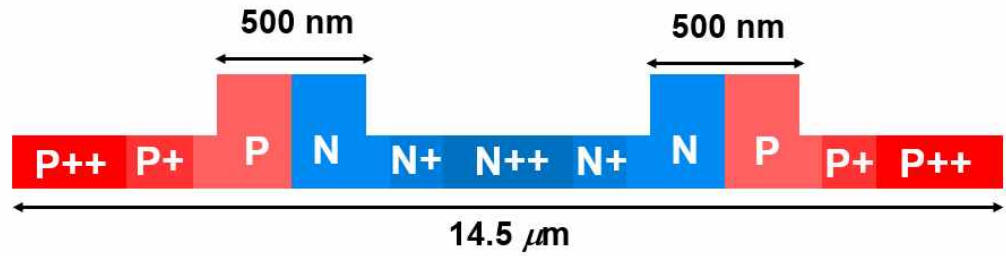

(b)

Fig. 2-8. Cross-sectional view of (a) a sample PN junction and (b) a PNP junction which has the same length with (a).

When PN junctions are connected in series in this way, the junction capacitance decreases, but at the same time, the junction resistance increases. Since these changes affect the overall microwave loss in the TWE through the junction RC time constant, an analysis of these effects is necessary.

Fig. 2-8(a) and (b) show the cross-sectional views of a simple PN junction and a series-connected PNP structure, respectively. Although the PNP structure includes longer traces—indicated by the gray dotted boxes—that contribute to increased resistance compared to a standard PN junction, the total length of the P+(+) and N+(+) regions (excluding the ~1 μm-wide PN region) is approximately 13.5 μm, meaning that the increase in resistance is less than double. The simulated junction resistance with the PNP configuration is 1.5 Ω·cm, while that of the only PN junction has the value of 1.05 Ω·cm. On the other hand, the capacitance becomes half, and this will make reduction of RC time constant.

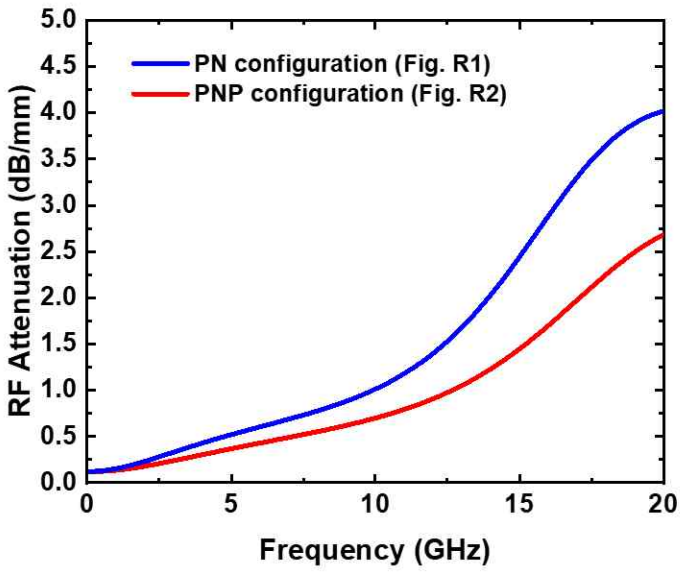

Fig. 2-9. RF attenuation of TWE with PN junction and PNP junction.

To evaluate the bandwidth enhancement resulting from reduced transmission line loss, we compared the microwave attenuation characteristics of transmission lines employing both PN and PNP doping configurations. As illustrated in Fig. 2-9, the PNP-doped structure exhibits lower microwave loss compared to the PN-doped counterpart. This result suggests that a Si MZM with a PNP doping configuration is capable of achieving higher modulation bandwidth, since the microwave loss directly impacts the EO S21.

Fig. 2-10(a) illustrates a simplified diagram of the SPPMZM structure. It has junction phase shifters of PNP structure. A 1 × 2 multimode interference (MMI) coupler splits the incoming optical signal into two paths, while a 2 × 2 MMI

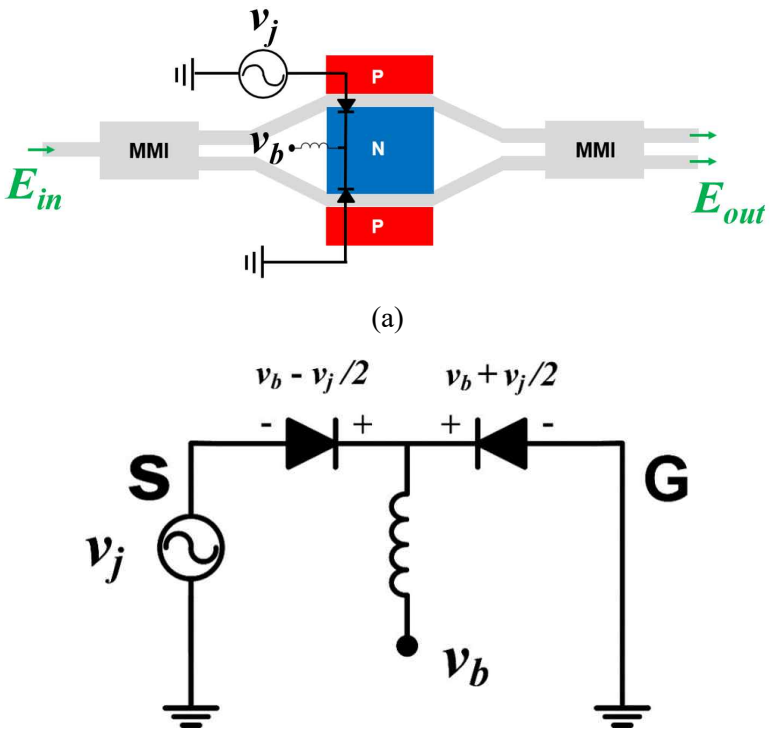

Fig. 2-10. (a) A simple diagram of the SPPMZM and (b) its equivalent circuit.

coupler combines the two optical signals after they have passed through separate phase shifters. A reverse bias voltage v_b is applied to the common N-type region of both phase shifters through an external inductor. This inductor—typically implemented using a commercial Bias-T—blocks the RF signal from leaking into the bias line, thereby enabling true push-pull operation of the Si SPPMZM.

When an microwave signal v_j is applied to one of the two P-type regions, labeled as S, it encounters two series-connected junction capacitances. Consequently, the voltages across the two PN junctions become $v_b - v_j / 2$ and $v_b + v_j / 2$, respectively. This configuration ensures that the modulator operates in a differential mode with a single-ended RF drive, as depicted in Fig. 2-10(b).

A photograph of the fabricated Si SPPMZM is presented in Fig. 2-11(a). The device integrates 2-mm-long PNP-doped junction phase shifters along with a TWE, which is designed to have a characteristic impedance of 50 Ω. To enable thermal bias tuning, thermo-optic heaters are implemented on both interferometer arms. Additionally, a termination resistor whose resistance is also targeted to 50 Ω is placed at the end of the TWE to suppress signal reflections. Grating couplers are employed for optical input and output.

Fig. 2-11(b) shows the vertical cross-sectional structure of the junction phase shifters. The optical waveguides used within the SPPMZM are rib waveguides, featuring a 500-nm width, 220-nm height, and a 90-nm slab thickness. The PNP doping profile is used to implement the phase shifters in this structure.

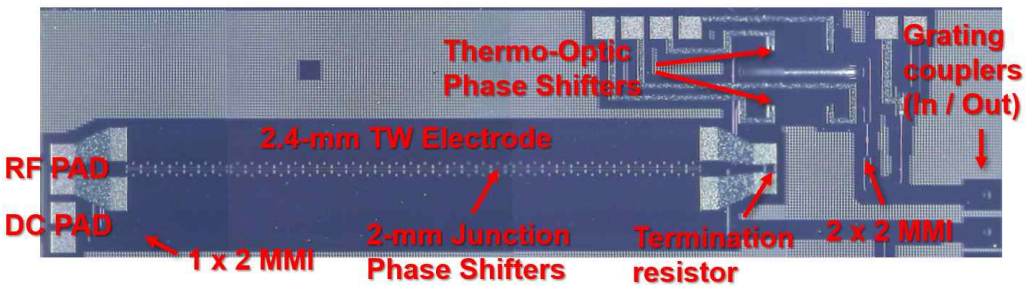

(a)

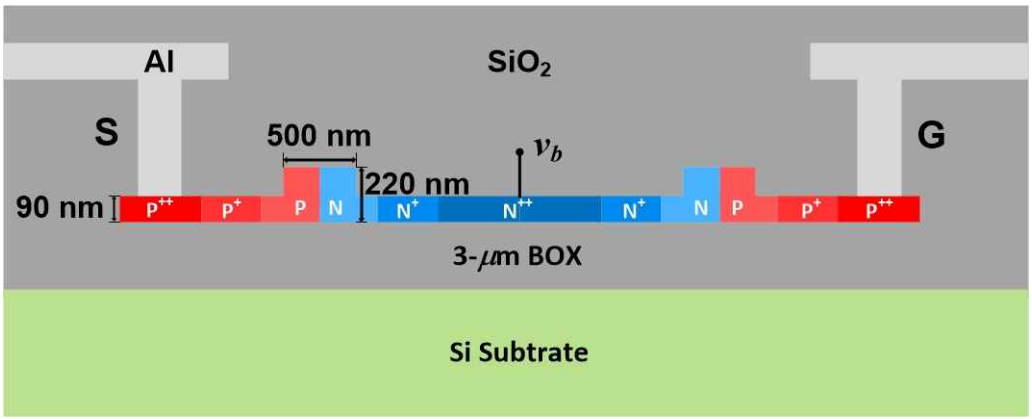

(b)

Fig. 2-11. (a) A chip photograph of the SPPMZM and (b) its cross-sectional view.

2.3.3 Extraction of Model Parameters

To accurately evaluate IMD3 and SFDR using the linearity model described in chapter 2.3.1, it is essential to precisely extract various model parameters of the sample Si MZM. This chapter describes the methods used for extracting these parameters.

A. Refractive Index n_{eff} and Optical Absorption Coefficient a

Since the foundry does not disclose the exact doping concentrations used in the junction phase shifters, the numerical values of the effective refractive index $n_{eff}(v)$ and the optical absorption coefficient $a(v)$ are extracted empirically. This is achieved by measuring the optical transmission characteristics of the fabricated Si SPPMZM and performing curve fitting of a theoretical model to the experimental data.

For this characterization, a bias voltage v_b is intentionally applied to only one of the two PN junctions in the Si SPPMZM. Under this asymmetric biasing condition, the measured transmission deviates from the original model in equation (2.56), and the corresponding modified expression becomes

$$E_{out} = \frac{1}{2} \cdot E_{in} \cdot \left[j \cdot \exp(-a(v_b)L_m) \cdot \exp\left(-j \frac{2\pi n_{eff}(v_b)}{\lambda} L_m \right) \cdot \exp(-j\phi) \right. \\ \left. + \exp(-a(0)L_m) \cdot \exp\left(-j \frac{2\pi n_{eff}(0)}{\lambda} L_m \right) \right]. \tag{2.58}$$

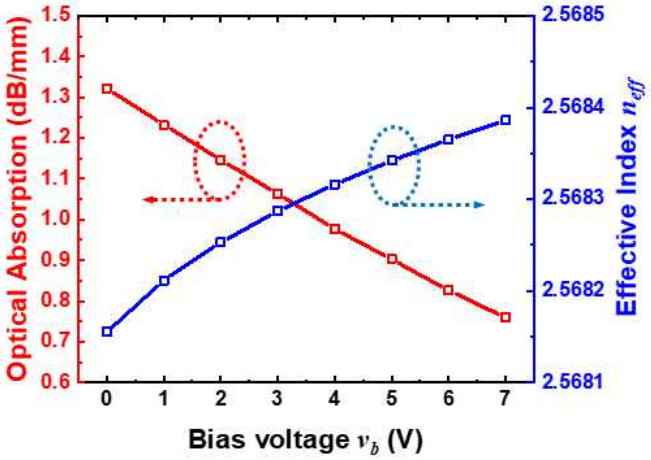

(a)

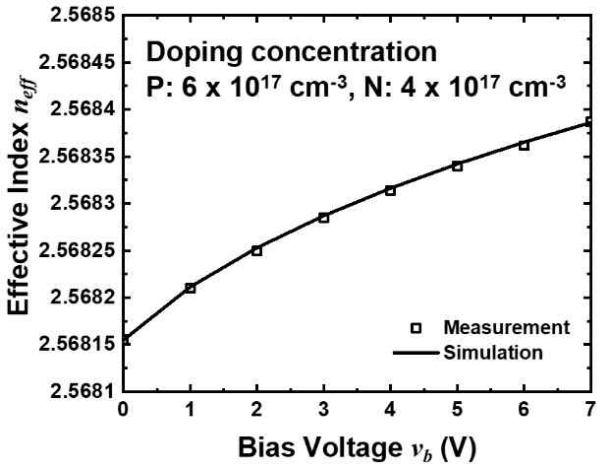

(b)

Fig. 2-12. (a) The extracted optical absorption and effective refractive index and (b) comparison between extracted and simulated values according to the doping concentration.

Due to the absence of explicit doping profiles in the process design kit (PDK) provided by the Si photonics foundry, we initially estimated the effective doping concentrations of the P- and N-type regions by assuming uniform doping and using the sheet resistance values listed in the PDK. However, as these estimates lacked sufficient accuracy, we further fine-tuned the doping levels to ensure that the simulated $n_{eff}(v)$ matched the measured values at 1550 nm. The simulations were performed using the MODE solver in Ansys Lumerical.

Fig. 2-12(a) presents the measured n_{eff} and a values at 1550 nm. As the reverse bias voltage v_b increases, the depletion width in the PN junction expands, leading to a decrease in a and an increase in n_{eff}. The effective index shows a square-root dependence on v_b, which is the primary contributor to the nonlinearity observed in the Si MZM transfer function. Fig. 2-12(b) compares the measured and simulated n_{eff} values across various bias voltages. The best-fit effective uniform doping concentrations were determined to be P: $6\times10^{17}\,\mathrm{cm}^{-3}$ and N: $4\times10^{17}\,\mathrm{cm}^{-3}$.

In Fig. 2-13, the measured normalized transmission characteristics (dotted lines) are compared with the simulation results (solid lines). To accurately model the device, waveguide dispersion effects were incorporated by using $dn_{eff}/d\lambda$ values of $-0.885\ \mu\mathrm{m}^{-1}$ for the doped waveguide regions within the junction phase shifters, and $-1.18\ \mu\mathrm{m}^{-1}$ for the undoped strip waveguides, as determined through simulation. While a is theoretically wavelength-dependent, its variation over the spectral range of interest was found to be negligible based on simulation results.

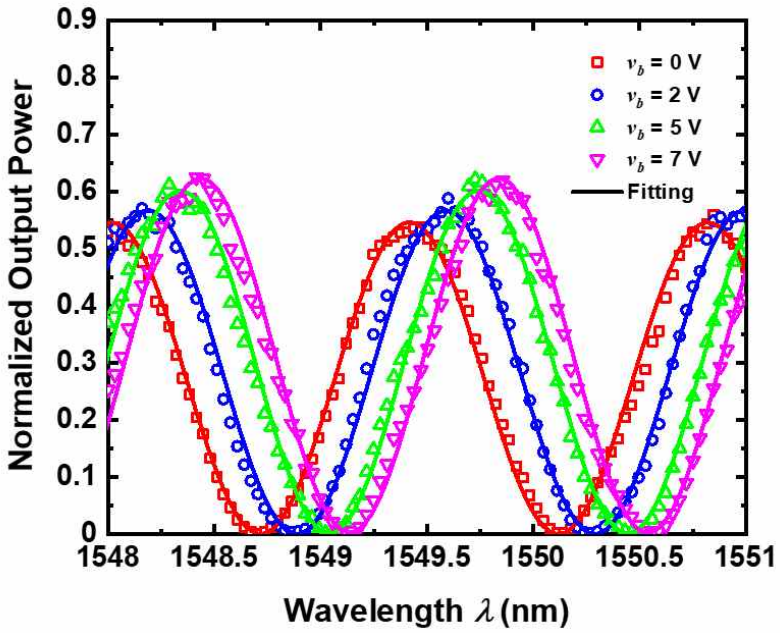

Fig. 2-13. The measured values of the output optical transmission spectra along various bias voltages v_b.

B. Characteristic Impedance Z, Microwave Effective Index n_{mw} and Microwave Attenuation Coefficient α

The characteristic impedance Z, microwave effective index n_{mw} and microwave attenuation coefficient α are key parameters that govern the transmission characteristics of the TWE. These quantities can be accurately extracted through EM simulations. Since the Si PNP junction directly affects the electrical behavior of the TWE, it is essential to determine both the series resistance R_s and junction capacitance C_J for the fabricated Si SPPMZM.

The values of R_s and C_J were derived from the PN junction, using the effective doping concentrations obtained in chapter 2.3.3.A. For this purpose, we first estimated the high doping concentrations in the P++ and N++ regions by

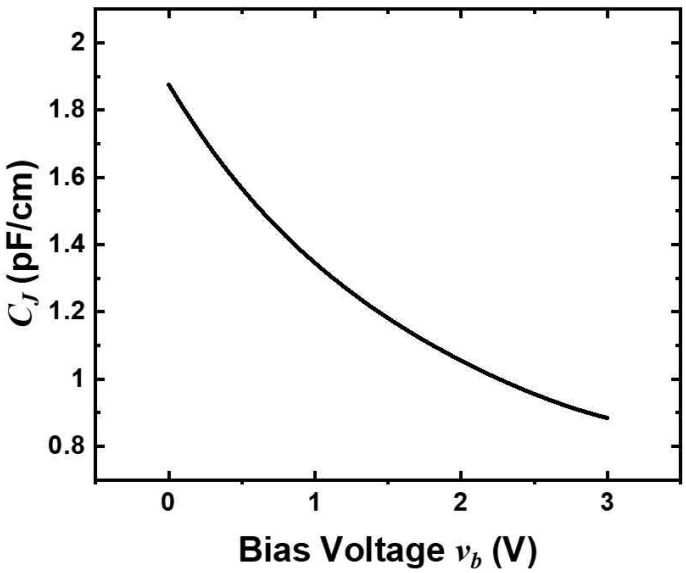

Fig. 2-14. Junction capactitance C_J along bias voltages v_b.

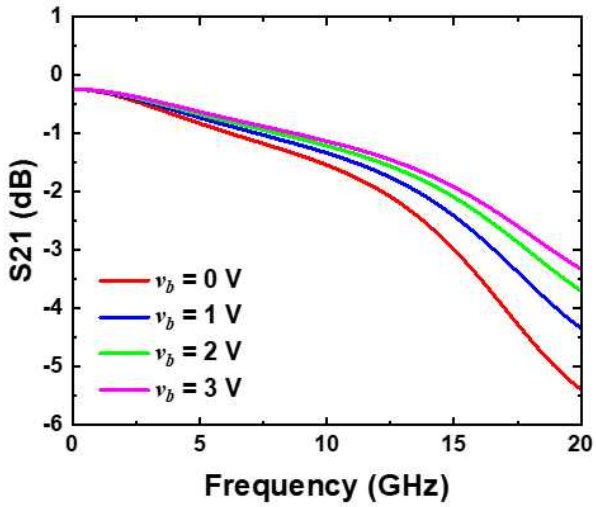

(a)

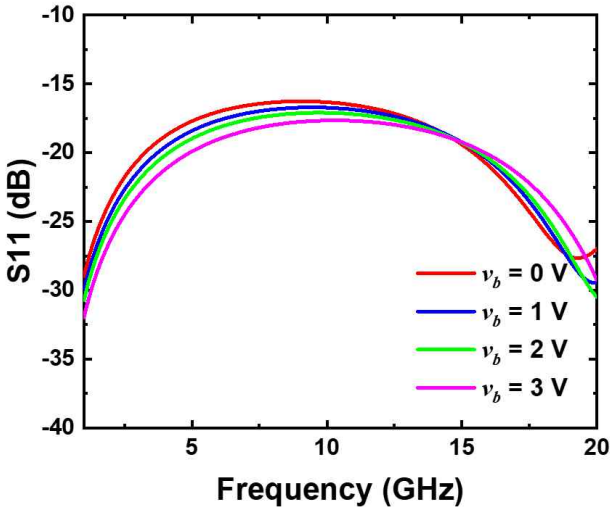

(b)

Fig. 2-15. The simulated (a) S21 and (b) S11 of the TWE.

assuming uniform doping and fitting the simulated resistance to the sheet resistance values provided in the PDK. A similar approach was applied to the P and N regions located in the core of the Si waveguide, with additional fine-tuning based on comparisons between measured and simulated effective indices.

With all six doping profiles extracted for the Si layers, current–voltage (I–V) simulations were performed for the PNP junction phase shifters using the DEVICE tool in Lumerical. C_J as a function of bias voltage is shown in Fig. 2-14. R_s was found to be approximately 1.5 Ω·cm, and remained independent of the applied bias voltage, as confirmed by I–V simulations, in accordance with the data of PDK. Using the estimated values of R_s and C_J, along with the physical structure of the traveling-wave electrode employed in the Si SPPMZM, we performed electromagnetic simulations using Advanced Design System (ADS) by Keysight. Specifically, Momentum EM simulation and schematic simulation tools within ADS were utilized to model the S-parameters of the traveling-wave electrode structure.

The simulation results are shown in Fig. 2-15(a) and (b), which present the absolute values of electrical transmission (S21) and reflection (S11) parameters at various v_b. From these S-parameters, Z, n_{mw} and α can be extracted using ABCD matrix method [88], [89].

Fig 2-16 simply shows a two-port system. The two-port system can be represented by the following equation.

$$\begin{pmatrix} V_1 \\ I_1 \end{pmatrix} = \begin{pmatrix} A & B \\ C & D \end{pmatrix} \begin{pmatrix} V_2 \\ I_2 \end{pmatrix} \tag{2.59}$$

ABCD matrix is defined as (See Appendix B)

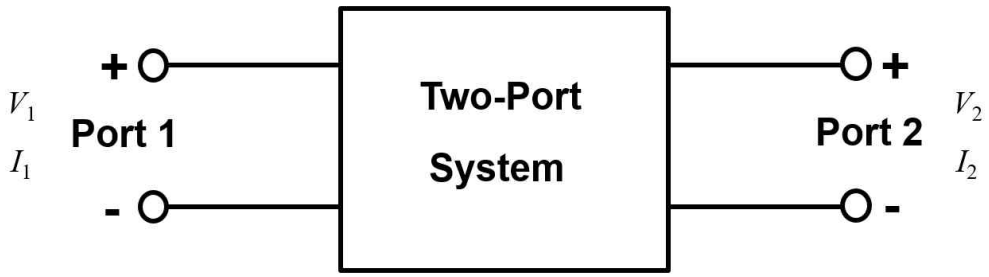

Fig. 2-16. Diagram of two-port system.

$$\begin{pmatrix} A & B \\ C & D \end{pmatrix} = \begin{pmatrix} \cosh(\gamma L) & Z\sinh(\gamma L) \\ \dfrac{\sinh(\gamma L)}{Z} & \cosh(\gamma L) \end{pmatrix} \tag{2.60}$$

Here, γ is given as

$$\gamma = \alpha + j\beta = \alpha + j\frac{\omega}{c} n_{mw} \tag{2.61}$$

L_{tw} is the length of TWE; α is microwave attenuation coefficient; and n_{mw} is microwave index as mentioned.

The ABCD matrix elements can be derived from the S-parameters using well-established conversion formulas as follows [88]:

$$A = \frac{(Z_g^* + S_{11}Z_g)(1 - S_{22}) + S_{12}S_{21}Z_g}{2S_{21}(R_g R_l)^{1/2}} \tag{2.62}$$

$$B = \frac{(Z_g^* + S_{11}Z_g)(Z_l^* - S_{22}Z_l) - S_{12}S_{21}Z_g Z_l}{2S_{21}(R_g R_l)^{1/2}} \tag{2.63}$$

$$C = \frac{(1-S_{11})(1-S_{22})-S_{12}S_{21}}{2S_{21}(R_g R_l)^{1/2}} \tag{2.64}$$

$$D = \frac{(1-S_{11})(Z_l^* + S_{22}Z_l)+S_{12}S_{21}Z_l}{2S_{21}(R_g R_l)^{1/2}} \tag{2.65}$$

where Z_g and Z_l denote the source and load impedances, and R_g and R_l represent their real components. In our measurement setup, these values are all standardized to 50 Ω. Additionally, due to the reciprocal and symmetric nature of the device under test, the S-parameters satisfy the conditions S21 = S12 and S11 = S22.

Once the ABCD matrix is obtained from the measured S-parameters, the characteristic impedance Z and the complex propagation constant γ can be extracted. The results of Z, n_{mw}, and α are shown in Fig. 2-17(a), (b), and (c) for different v_b. As shown in Fig. 2-17(a), the extracted $|Z|$ is slightly lower than 50 Ω, which can be attributed to inaccuracies in the initial estimates of R_s and C_J during the Si SPPMZM design stage.

Separately, the optical group index no is calculated via mode simulation of the waveguide structure, incorporating the previously estimated uniform doping concentrations. A value of 3.94 is obtained. The load impedance Z_l of the termination resistor is also measured independently via I–V characterization, yielding a value of 50.8 Ω.

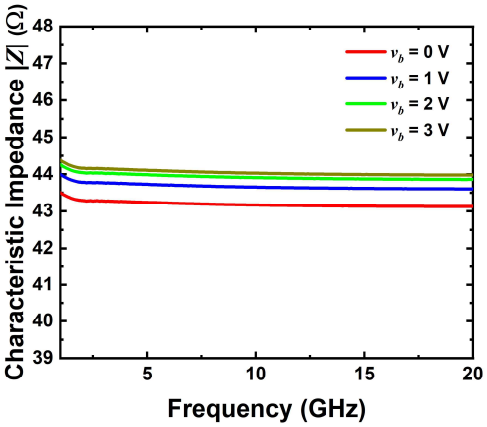

(a)

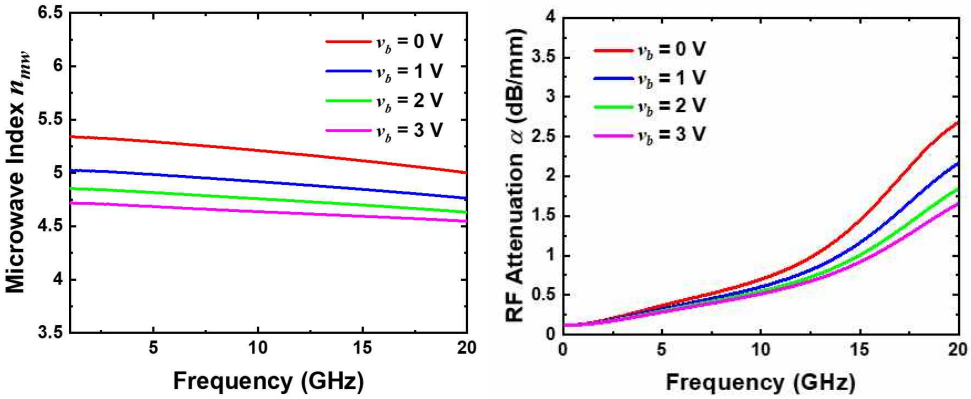

(b) (c)

Fig. 2-17. The calculated values of (a) characteristic impedance, (b) microwave index, and (c) RF attenuation of the TWE.

C. Verification of the accuracy of the extracted parameters

As mentioned in 2.2.3, EO frequency response results from the model parameters which are extracted in chapter 2.3.3.A and 2.3.3.B. To verify the accuracy of the extracted model parameter values, the EO frequency response was measured for different v_b values and compared with the calculated results obtained using those parameters. In Fig. 2-18, the dotted curves represent the measured EO S21, while the solid curves show the calculated EO S21 based on the extracted numerical parameter values. The close agreement confirms that these parameters are suitable for analyzing the linearity of the Si MZM.

In theory mentioned in chapter 2.2.3, an electrical S21 of –6.4 dB for the TWE corresponds to an EO response of 3 dB, assuming no velocity mismatch between the optical and RF signals and no impedance mismatch. However, as seen in Fig. 2-15(a) and 2-18, the microwave signal frequency at which the electrical S21 reaches –6.4 dB does not align with the frequency where the EO S21 reaches –3 dB. This discrepancy arises from velocity mismatch between the RF and optical signals, as well as impedance mismatches between the source, load, and TW electrodes. Additionally, R_s and C_J influence the EO S21, which can further increase the disparity.

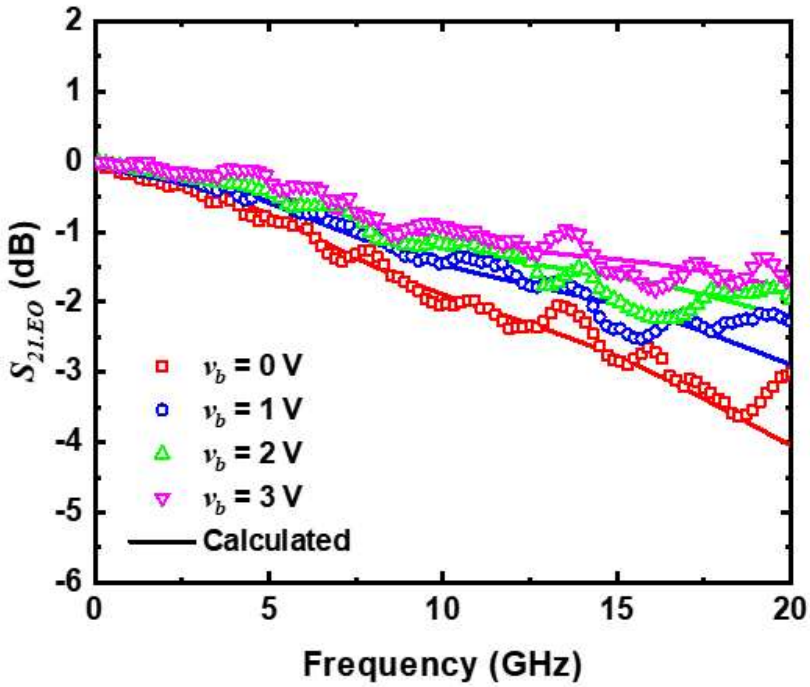

Fig. 2-18. Comparison between the measured EO S21 and calculated EO S21 with the extracted parameters.

2.3.4 Experimental Verification

Fig. 2-19 illustrates the experimental setup used for measuring the IMD3 of the fabricated Si SPPMZM, which serves to validate the proposed linearity simulation model. Two RF signal generators (Anritsu 68177C and Agilent 83752B) are employed to generate a two-tone input, which is combined using a Mini-Circuits ZX10-2-183-S+ power combiner before being applied to the modulator. The modulated optical signal is detected by an Optilab PR-23-M photodetector, and the resulting electrical signal is analyzed using an RF spectrum analyzer, Agilent 8593E, to obtain the RF power spectral density.

Both the simulation and the measurement use two-tone sinusoidal inputs at 9.9 GHz and 10.1 GHz, injected into the device. The simulated output power spectrum $T_{out}(f)$ is computed using the procedure described in Fig. 2-7, incorporating all previously extracted device parameters. To experimentally validate these results, $T_{out}(f)$ is measured under the same conditions.

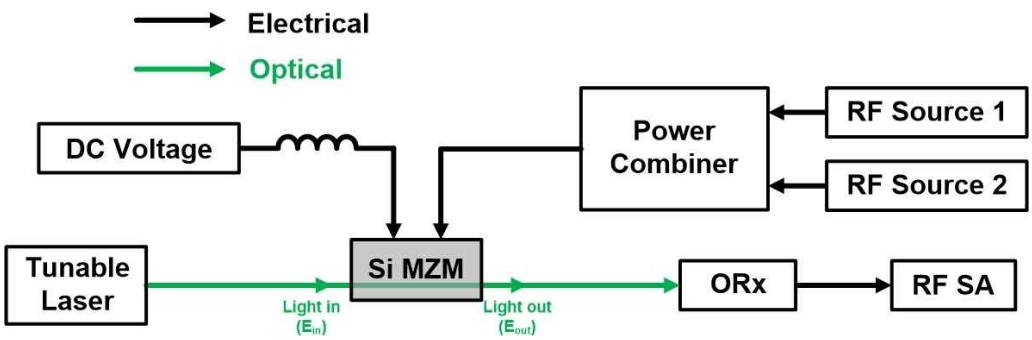

Fig. 2-19. Experimetal setup for two-tone measurement. ORx: optical receiver, RF SA: RF spectrum analyzer.

A wavelength of 1548.8 nm is selected for the measurement, as this minimizes coupling losses through the grating couplers. The input optical power is set to 0 dBm, and the device is placed on a temperature-controlled stage maintained at 25 °C.

Fig. 2-20(a) presents the simulated $T_{out}(f)$ spectrum (solid lines) alongside the measured data (empty squares). The fundamental tones appear at 9.9 GHz and 10.1 GHz, while the IMD3 components are observed at 9.7 GHz and 10.3 GHz. Fig. 2-20(b) compares the simulated and measured power levels of both the fundamental and IMD3 tones as a function of reverse bias voltage v_b, when the Si SPPMZM is biased at the quadrature (Q) point, where the optical output is at 50-% transmission. The results exhibit strong agreement, with deviations within 1.5 dB.

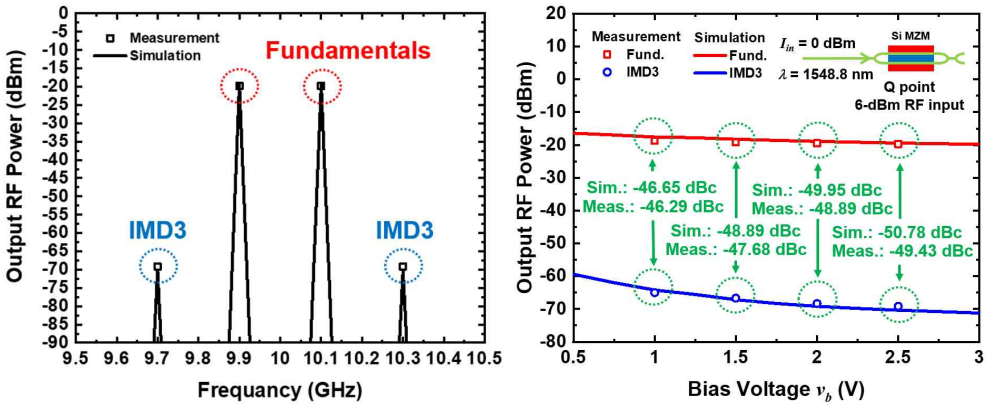

(a) (b)

Fig. 2-20. (a) The measured and simulted values of fundamental and IMD3 components generated by 9.9-GHz and 10.1-GHz microwave signals and (b) the simulated and measured values of fundamental and IMD3 signal power along bias voltages v_b. 0-dBm input optical signal is entered to the Si SPPMZM. The wavelength of the input optical signal is 1548.8 nm. Input RF power is 6 dBm. The bias of the Si SPPMZM is Q point.

Further comparison is made at different bias points, achieved by tuning the phase shift via thermo-optic heaters. Fig. 2-21(a), (b), (c), and (d) show both simulated and measured results for various v_b values and MZM bias points. If bias point is Q bias, phase difference between two arms of the MZM is 0 and optical DC transmission become half compared to peak power. On the other hand, if phase difference is changed to $-\pi/2$ or $\pi/2$ by the heaters, optical transmission becomes null or peak bias because of cosine characteristic of the MZM. As observed, the simulated and experimental trends are generally consistent. The simulation predicts that the IMD3-to-fundamental power ratio remains relatively constant across different bias points, whereas the measurements show a slight improvement in linearity when operating away from the Q point. This discrepancy may be attributed to modeling limitations in the current simulation framework.

The noise floor must be estimated prior to determining the SFDR [90]. In this analysis, the relative intensity noise (RIN) of the tunable laser is assumed to be –140 dB/Hz, and a temperature of 25 °C is used for thermal noise calculations. The noise is evaluated over a 1 Hz bandwidth.

The total noise floor at the photodetector consists of three main components: RIN, shot noise, and thermal noise. RIN arises from fluctuations in the laser's optical output power and is proportional to the output optical power. Shot noise originates from the photocurrent generated in the photodetector, while thermal noise results from the thermal agitation of electrons within the PIC at a given temperature. The overall noise floor is the sum of these three components.

RIN power can be calculated using the following expression:

$$P_{RIN} = RINi_{pd}^2 BR_l \,. \tag{2.66}$$

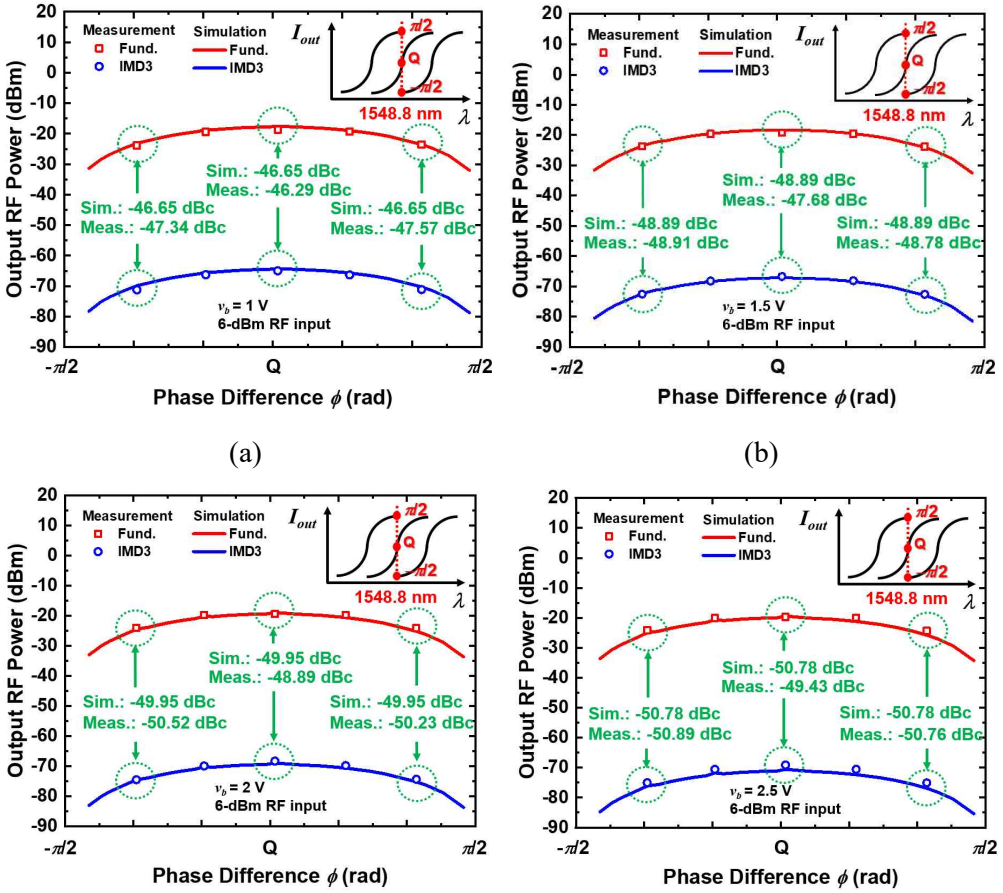

Fig. 2-21. The measured values of fundamental and IMD3 signals along phase difference between two arm waveguides in the Si SPPMZM at (a) v_b = 1 V, (b) v_b = 1.5 V, (c) v_b = 2 V, and (d) v_b = 2.5 V. 0-dBm input optical signal is entered to the Si SPPMZM. The wavelength of the input optical signal is 1548.8 nm. Input RF power is 6 dBm. The bias of the Si SPPMZM is Q point.

RIN in this study is 10^{-14} which is same with –140 dB/Hz. i_{pd} is photocurrent, and B is noise bandwidth. R_l is load resistance which is 50 Ω in this study. Shot noise power is expressed as

$$P_{shot} = 2qi_{pd}BR_l\,. \tag{2.67}$$

where q is electron charge. Thermal noise power is given by

$$P_{thermal} = k_bTB, \tag{2.68}$$

where k_b is Boltzman constant and T is absolute temperature.

As an example, at the Q point with v_b = 1 V, an input optical power of 0 dBm is attenuated to –5.5 dBm at the output of the Si SPPMZM. With a photodetector responsivity of 0.65 A/W, this results in a photocurrent of 0.184 mA. The corresponding shot noise and RIN noise are calculated to be –175.3 dBm and –167.7 dBm, respectively. The thermal noise contribution is –173.9 dBm, resulting in a total noise floor of –166.1 dBm. With the transimpedance amplifier (TIA) gain of 1150 V/A in the optical receiver, assuming there is zero noise figure to get SFDR of the Si MZM itself, the effective noise floor becomes –138.9 dBm/Hz.

Simulations and measurements were conducted by increasing the input microwave signal power to determine the SFDR. For the simulation, input microwave signals ranged from –4 dBm to 10 dBm, while the measurement used input powers from 6 dBm to 10 dBm, limited by the sensitivity of the RF spectrum analyzer, which prevented accurate measurements at lower power levels.

Fig. 2-22(a) and (b) present the fitted results of the fundamental and IMD3 components from both simulation and measurement at the Q bias point with v_b = 1 V. Fig 2-22(c) compares the measured and simulated SFDR values at different v_b levels under Q bias. Despite variations in v_b and phase ϕ, the simulated SFDR values closely match the measured results. The SFDR shows only a slight dependence on v_b. As v_b increases, the noise floor rises while IMD3 levels decrease, leading to minimal overall variation.

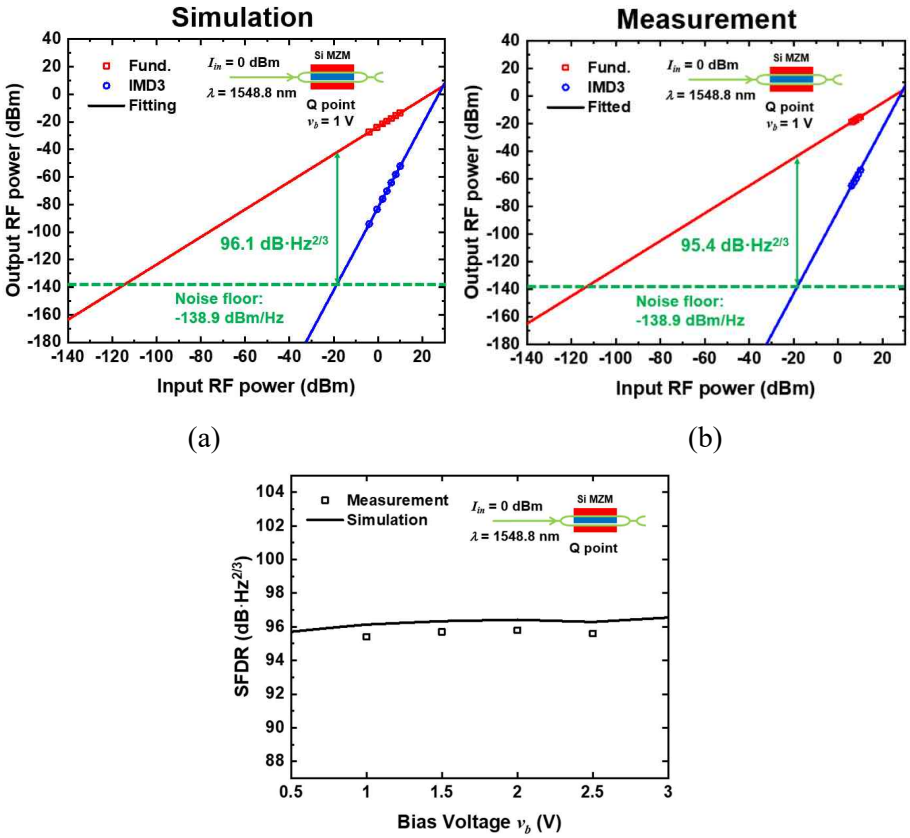

Fig. 2-22. (a) The simulated and (b) measured SFDR (c) SFDR values with different bias voltages v_b The input optical signal has 0-dBm power and wavelength of 1548.8 nm.

2.3.5 Linearity Analysis

Using the experimentally validated simulation model, we investigated the key parameters that influence the linearity of Si MZMs. Among these, the effective refractive index n_{eff} and the junction capacitance C_J are both voltage-dependent nonlinear parameters, making their roles in linearity performance particularly important. To evaluate their effects, we conducted simulations where each parameter was artificially linearized with respect to the bias voltage v_b, and the results were compared with the original simulation results at the Q point.

Fig. 2-23(a) presents the simulated fundamental and IMD3 signals under the assumption of both nonlinear and linear n_{eff}. The overall magnitudes of both signals are reduced in this case; however, at v_b = 1 V, the IMD3 component decreases more than the fundamental component, leading to approximately 3-dB

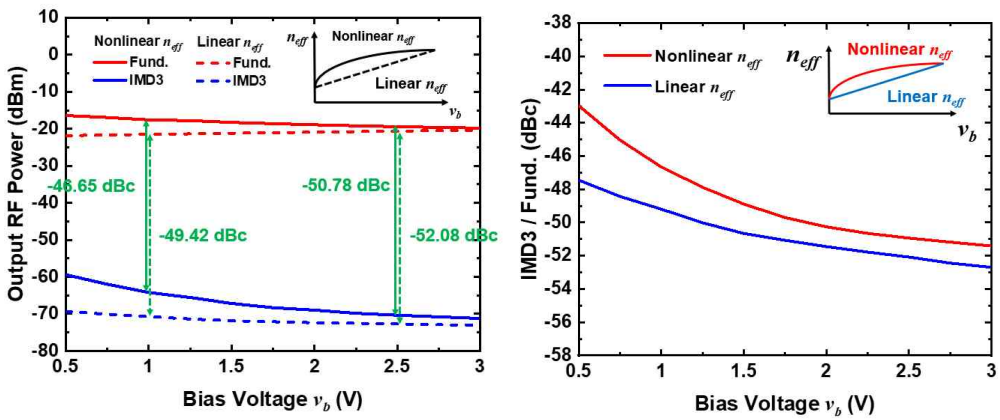

(a) (b)

Fig. 2-23. (a) The simulted values of fundamental and IMD3 power with linear n_{eff} and nonlinear n_{eff} (b) comparison of the ratio between fundamental and IMD3 power with both cases.

improvement in their power ratio. At a higher bias of v_b = 2.5 V, the improvement in the ratio is limited to about 1 dB, suggesting that the influence of n_{eff} becomes less significant at higher bias voltages. Additionally, the linearization of n_{eff} results in minimal variation in signal power across different v_b values. Fig. 2-23(b) compares the IMD3-to-fundamental power ratio at the Q point between the linearized and actual n_{eff} cases, showing a notable difference at lower bias voltages.

Similarly, Fig. 2-24(a) shows simulation results comparing the fundamental and IMD3 signals under conditions where C_J is either allowed to vary naturally or is held constant. When C_J is fixed, the voltage drop across the RC network increases, slightly reducing the fundamental signal power. The IMD3 signals are more significantly suppressed across all bias voltages, resulting in about 4-dB improvement in the fundamental-to-IMD3 power ratio. Fig. 2-24(b) illustrates the

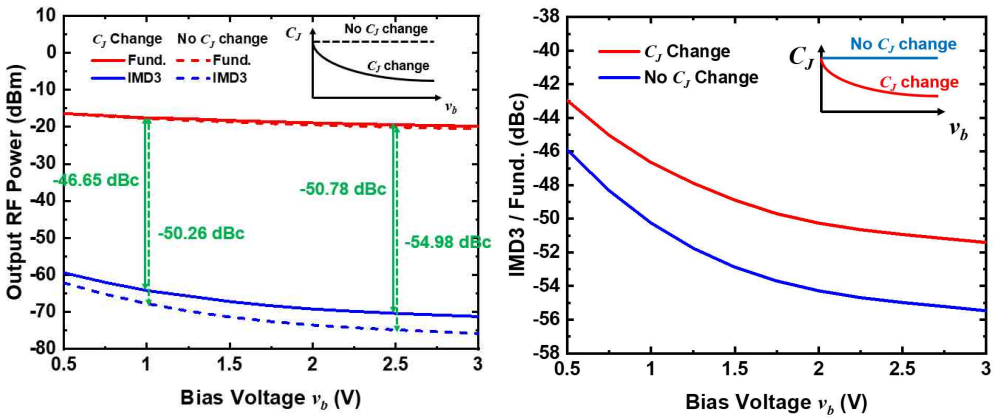

(a) (b)

Fig. 2-24. (a) The simulted values of fundamental and IMD3 power with constant C_J and voltage-dependent C_J (b) comparison of the ratio between fundamental and IMD3 power with both cases.

simulated power ratio at the Q point under the constant C_J assumption, highlighting a little increasing deviation from the real case as v_b increases.

These findings indicate that C_J plays a critical role in the linearity of the device, in addition to the nonlinear effects of n_{eff}. Specifically, neff has a dominant influence at lower bias voltages, whereas C_J becomes more significant at higher bias levels.

Unlike previous studies, which focused solely on EO models and neglected electrical nonlinearities, our modeling approach incorporates both electrical and optical effects, capturing additional sources of nonlinearity. As a result, our simulated values for IMD3 and SFDR show improved agreement with experimental results, enhancing the accuracy of performance prediction. This comprehensive modeling methodology is expected to serve as a valuable tool for the design and optimization of future Si MZMs.

Additionally, the linearity of the Si MZM is compared to that of an ideal MZM exhibiting only a fundamental cosine transfer function, excluding the effects of n_{eff} and C_J. In this comparison, I simulated the ratio of IMD3 power to fundamental power under the assumption that the MZM follows a pure cosine response and that both the effective refractive index and optical absorption vary linearly with the applied voltage. The Q-point condition is assumed to be maintained by appropriately controlling the phase difference between the two arms of the MZM.

Fig. 2-25 presents the simulated fundamental and IMD3 power as functions of input RF power, based on both the proposed Si MZM model and the ideal cosine-based MZM at a bias voltage of 1 V. As shown in the figure, the ideal MZM with a pure cosine characteristic achieves approximately a 6-dB better

IMD3-to-fundamental power ratio, indicating better linearity performance compared to the realistic Si MZM model.

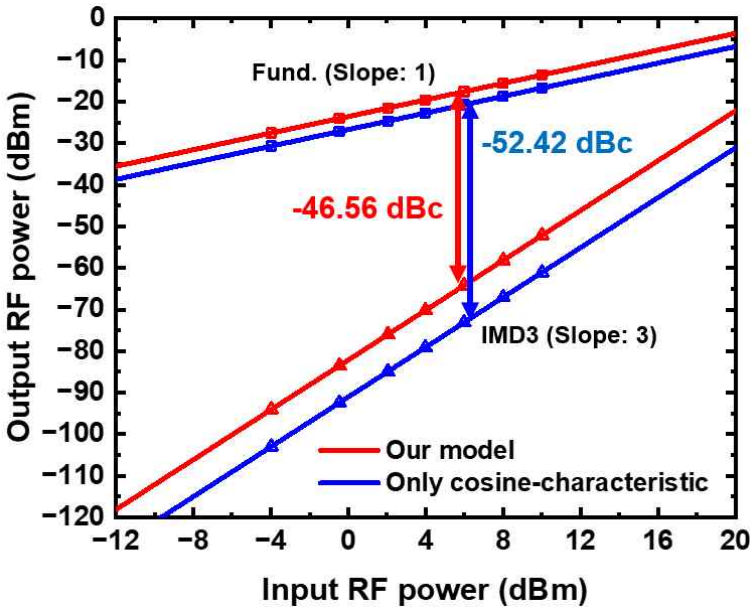

Fig. 2-25. The Simulated RF power of the fundamental and IMD3 signals using our model (red line) and based on only cosine characteristic of MZMs (blue line) at 1-V bias voltage.

2.3.6 Linearity Optimization

The validated model can also be used to simulate the linearity of a Si TWE MZM across all bias points and bias voltages. This allows us to identify the bias condition that yields the highest SFDR for the fabricated Si TWE MZM. Fig. 2-26 presents the simulated SFDR values for different bias points and voltages, based on the Si TWE MZM described in chapter 2.3.2.

In Fig. 2-26, the star symbol marks the bias condition producing the maximum SFDR, which occurs at a bias voltage of 2 V and at an MZM bias point slightly below the quadrature (Q) point. Under these conditions, the SFDR reaches 98.5 $dB \cdot Hz^{2/3}$. The slightly higher SFDR observed below the Q point is attributed to a lower noise floor at this bias point compared to the Q point for the same input optical intensity, which contributes to improved SFDR. The measured SFDR at the starred bias point was approximately 99.1 $dB \cdot Hz^{2/3}$, showing only a small deviation from the simulated value. This optimal SFDR is about 4 dB lower than recently reported result for a single Si MZM [86].

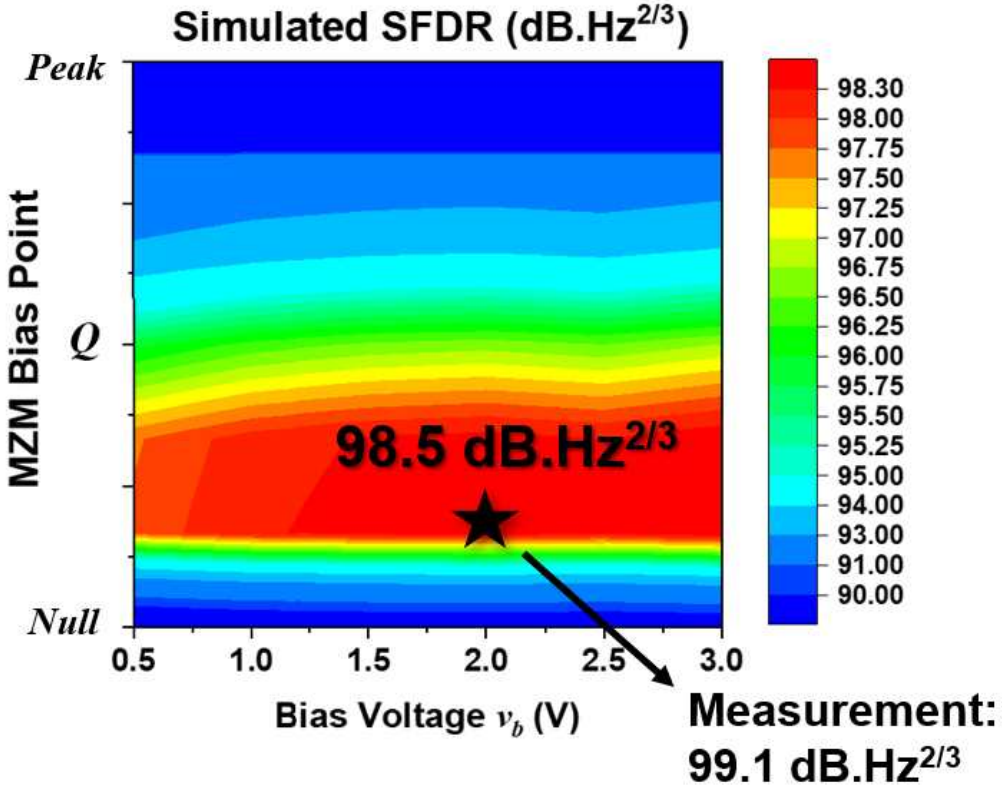

Fig. 2-26. The Simulated SFDR values along MZM bias points and bias voltages

2.4. Summary

A comprehensive modeling technique for evaluating the modulation linearity of Si TWE MZMs, which are crucial for analog and microwave photonic applications, is presented in this dissertation. The proposed model accounts for the nonlinearities in both the electro-optic phase shifters and the TWE, incorporating key parameters such as voltage-dependent effective refractive index and junction capacitance. The authors extract these model parameters through a combination of measurements and simulations and validate the accuracy by comparing the simulated EO frequency response and IMD3 with experimental results. The model is shown to predict SFDR values with high accuracy, even under varying bias conditions.

The study further analyzes how individual device parameters affect modulation linearity. It reveals that the nonlinear variation of the effective refractive index and junction capacitance play dominant roles in generating IMD3, with the effective refractive index being more critical at low bias voltages and the junction capacitance at higher ones. The noise floor is carefully estimated based on RIN, shot noise, and thermal noise to accurately determine SFDR. Comparison with an ideal cosine-response MZM confirms that the realistic Si MZM exhibits degraded linearity due to physical effects. Overall, this modeling framework provides valuable insight into the design and optimization of highly linear Si MZMs for MWP systems.

3. Si Ring-Assisted Mach-Zehnder Modulators (RAMZMs)[2)]

In addition to establishing a simulation model for precise linearity characterization of EO modulators, organizing MWP systems with high linearity is also important. Various linearization techniques have been proposed to address the nonlinear behavior of modulators, including electronic pre-distortion circuits [63] and IMD3 cancellation methods [64]. These approaches aim to correct nonlinearities in the electrical domain; however, they are fundamentally narrowband and do not fully leverage the broadband capabilities of photonic systems. As such, there is a growing need for linearization strategies that operate entirely within the photonic domain, especially for microwave photonic applications.

One approach involves modifying the structure of the MZM. The dual-parallel MZM (DPMZM) or dual-series MZM (DSMZM), for example, has been demonstrated to significantly enhance SFDR [91], [92]. However, since it consists of two MZMs, it occupies a relatively large footprint, making it less ideal for dense photonic integration. To address this, a Si ring-assisted MZM (RAMZM) has emerged as a promising alternative [93], [94]. By integrating compact Si ring modulators (RMs), the RAMZM achieves a smaller footprint, which is highly beneficial for integrated photonic circuits. In this architecture, the nonlinear voltage-to-phase characteristic of the ring resonator is used to compensate for the compressive phase-to-intensity response of the MZM, leading to improved overall

---

2) © IEEE. Reprinted with permission from "Min-Hyeok Seong *et al*., 'A highly linear and compact Si ring-assisted Mach-Zehnder modulator at X band,' in proccedings of *International Topical Meeting on Microwave Photonics 2025*, 14-17 Oct., 2025.

linearity. Nevertheless, previously reported Si RAMZMs have either shown limited SFDR [93] or operated only at relatively low frequencies [94].

In this chapter, a Si RAMZM, which can make high linearity at high microwave signal frequency such as X band, is described, and its measured results are presented.

3.1. Structure

The RAMZM essentially incorporates the structure of an MZI, but differs from a conventional MZM in that each arm waveguide of the MZI has a RM. Fig. 3-1 provides a schematic illustration of the RAMZM structure.

The PN junction inside the RM induces a phase change in the arm waveguide through the plasma dispersion effect, similar to that in a Si MZM. However, unlike the Si MZM, this plasma dispersion effect is applied within the RM. Moreover, the optical output characteristics of the RM vary not only in phase but also dominantly in intensity depending on the input wavelength. As a result, the optical output characteristics of the PN junction–based Si waveguide in an RM differ significantly from those of a Si MZM, leading to distinct linearity behavior.

The properties of the RM in the RAMZM and how the RM influences the overall RAMZM characteristics are discussed in detail in chapter 3.2.

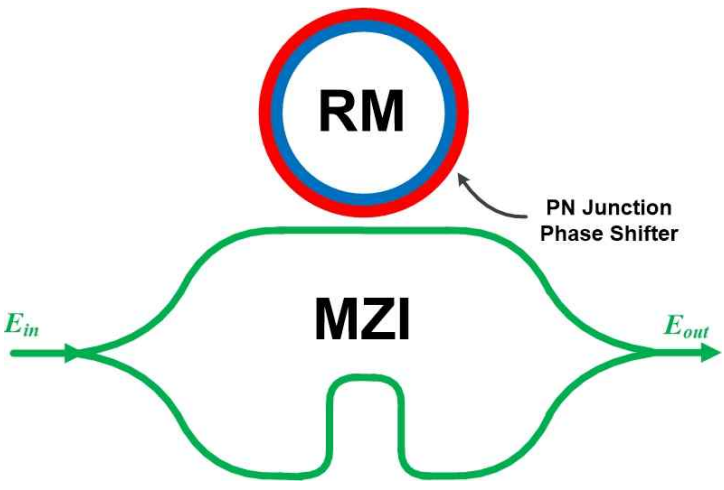

Fig. 3-1. A simplified diagram of an RAMZM.

3.2. Characteristics

3.2.1 Ring Modulators (RMs)

The Si RM used in the Si RAMZM can also be a highly promising candidate among Si photonics–based EO modulators on its own, owing to its high EO bandwidth and low power consumption. The RM is based on a ring resonator structure [95], as shown in Fig. 3-2.

A ring resonator is composed of a ring-shaped waveguide positioned adjacent to a straight bus waveguide, close enough for optical coupling to occur. The interaction between the two waveguides is characterized by two primary parameters: a, which denotes the round-trip loss within the ring waveguide, and r, the straight-through coefficient, representing the ratio of the optical field exiting the coupler to the input field. Another key parameter shown in Fig. 3-2 is the coupling coefficient k, which quantifies the fraction of the input optical field that

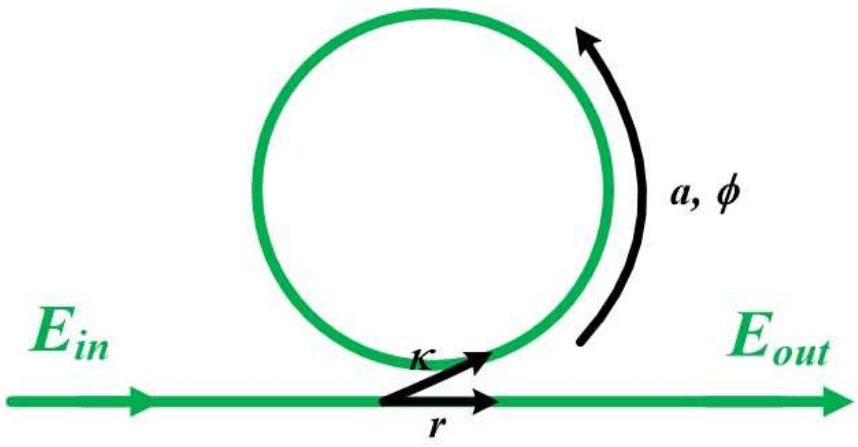

Fig. 3-2. A simplified diagram of a ring resonator.

couples into the ring waveguide. Due to the inherent 90° phase shift introduced during coupling, this coefficient is generally expressed as jk. Assuming negligible coupler loss, the coefficients satisfy the relationship $r^2 + k^2 = 1$

When light enters the ring resonator, a portion of it couples into the ring, circulating with a certain loss and phase shift. Upon completing one round trip, part of the optical field couples back out into the bus waveguide, while the rest continues circulating. This process repeats indefinitely, and as a result, the output optical field can be expressed as an infinite geometric series involving the input field E_{in}, the round-trip phase shift, and attenuation, given as

$$E_{out} = rE_{in} - k^2 ae^{-j\phi} E_{in} - k^2 rae^{-j2\phi} E_{in} - \cdots . \tag{3.1}$$

Letting L represent the ring circumference and n_{eff} the effective index, the round-trip phase shift, which is optical detuning, is determined by $\phi=2\pi n_{eff}L/\lambda$. This series can be summed analytically, yielding a closed-form expression for the output field E_{out} which is given as

$$E_{out} = E_{in} \frac{r - ae^{-j\phi}}{1 - rae^{-j\phi}}. \tag{3.2}$$

From that, the optical transmission function of the ring resonator can be derived. Optical transmission of the ring resonator T_{out} is given by

$$T_{out} = \left| \frac{E_{out}}{E_{in}} \right|^2 = \frac{a^2 + r^2 - 2ra\cos\phi}{r^2 a^2 - 2ra\cos\phi + 1}. \tag{3.3}$$

Additionally, the output phase relative to the input signal can be calculated using the angle of E_{out}/E_{in}, and that is

$$\theta = \pi + \phi + \arctan\frac{r\sin\phi}{a - r\sin\phi} + \arctan\frac{ra\sin\phi}{1 - ra\cos\phi}. \tag{3.4}$$

Resonance in the ring waveguide occurs when the round-trip phase shift is an integer multiple of 2π, satisfying

$$m\lambda_{res} = n_{eff}L, \tag{3.5}$$

where m is the modal integer and λ_{res} is the resonance wavelength. This condition results in periodic resonance wavelengths, as illustrated in Fig. 3-3. Since the resonance wavelength is sensitive to changes in the effective index, ring resonators are widely used in sensing applications [96]-[99] and as optical filters [100], [101].

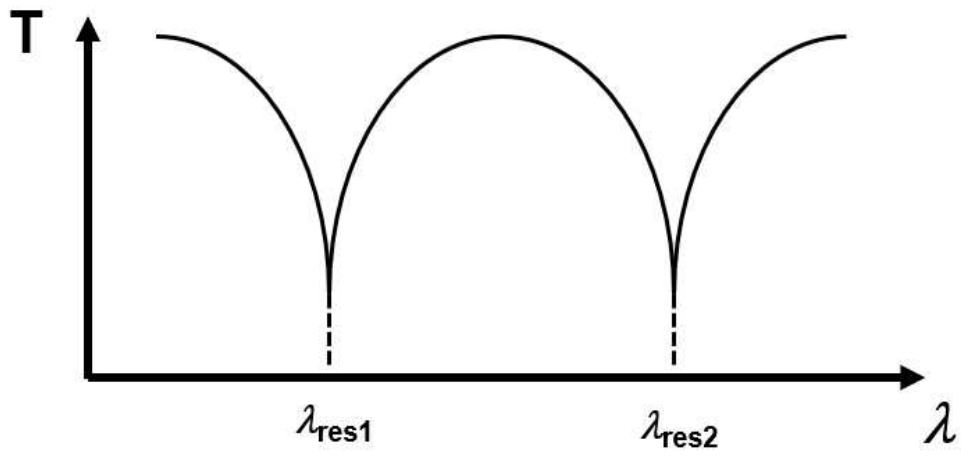

Fig. 3-3. Optical power spectrum of a ring resonator.

In addition, the phase shift expressed in (3.3) varies depending on the values of a and r, which in turn affect the characteristics of the ring resonator. Fig. 3-4 show the effective phase shift of the output optical signal θ relative to the input optical signal as a function of the relationship between a and r. When r is greater than a, the ring resonator is under-coupled, and the phase shift does not exceed π. When r is less than a, the ring resonator is over-coupled, and a π phase shift occurs at the point where the optical detuning is zero. When r equals a, the ring resonator is critically coupled; in this case, a sharp phase change occurs at the resonance wavelength where the optical detuning is zero, and the optical intensity at the resonance wavelength is the lowest among the three cases.

Since the RAMZM operates by modulating the phase difference between the two arm waveguides of the MZI through the input electrical signal, it uses RMs in the critical- or over-coupling regime, where the phase change at the resonance wavelength is large. In particular, over-coupling is often preferred because, in the

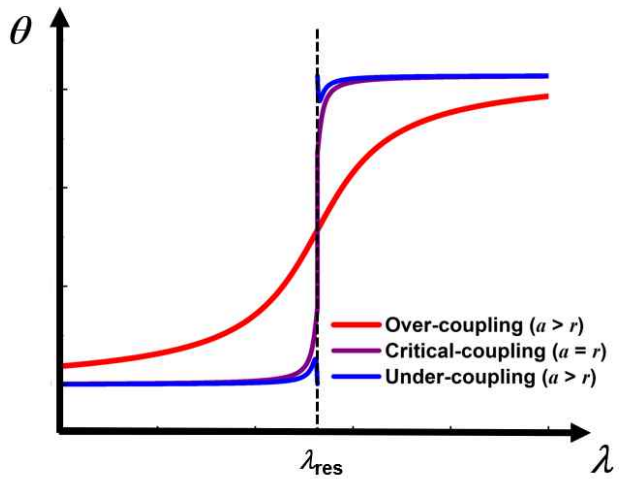

Fig. 3-4. The effective phase shift of a ring resonator for three coupling conditions.

critical coupling case, the optical intensity approaches zero at the resonance wavelength.

In optical communication, Si RMs offer an alternative to MZM for EO modulation. By exploiting the plasma dispersion effect [69], the effective index in the ring waveguide can be tuned via carrier concentration, which shifts the resonance wavelength and modulates the transmission. This is achieved by embedding a PN junction into the ring waveguide, as shown in Fig. 3-5. Applying a voltage across the junction alters the carrier density, thereby modifying the effective index and the optical transmission at a fixed operating wavelength, as demonstrated in Fig. 3-5.

There are two main types of Si RMs: carrier-injection (forward-bias) and carrier-depletion (reverse-bias). The carrier-injection type offers energy efficiency due to the large carrier modulation in forward-bias operation; however, it suffers from limited EO bandwidth because of carrier recombination effects [102]-[104]. For high-speed applications, the depletion-type RM is preferred despite requiring a higher voltage swing [105]-[107]. Thanks to their ultra-compact footprint and compatibility with wavelength-division multiplexing (WDM) without needing additional multiplexers, Si RMs enable low-power, high-throughput interconnects. These advantages position Si RMs as one of the most promising modulator technologies for Si photonic interconnect systems.

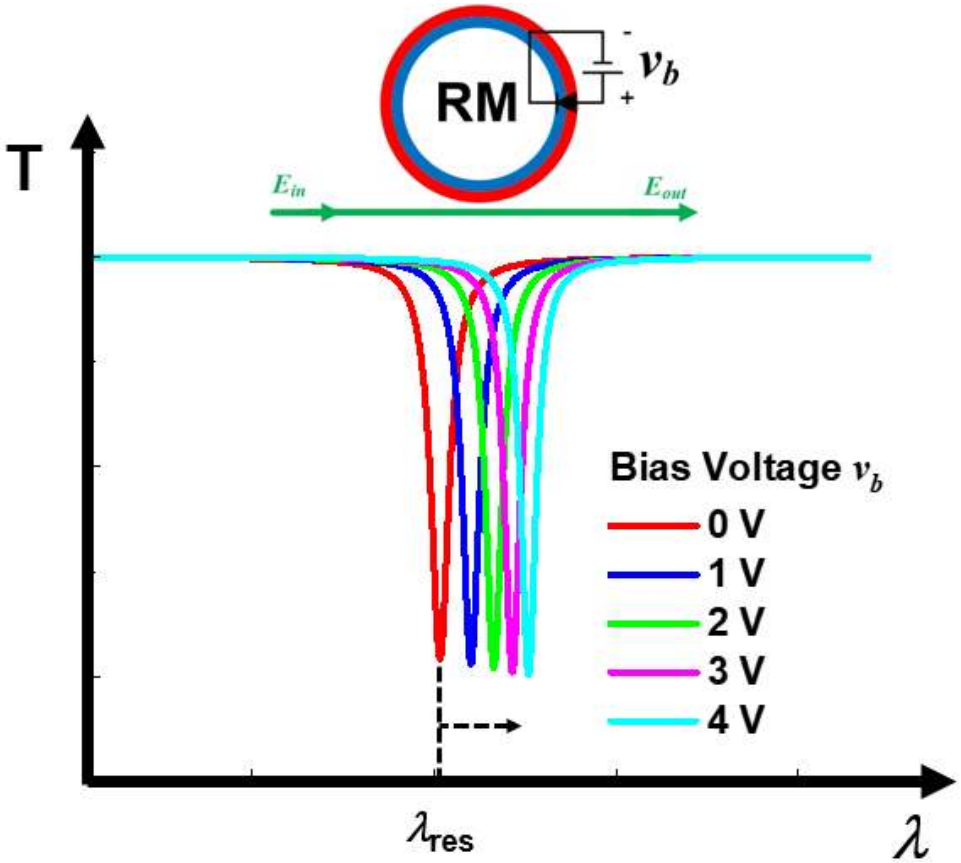

Fig. 3-5. Optical spectrum of a ring resonator along bias voltages.

3.2.2 RAMZM

The characteristics of a RAMZM can be analyzed in two configurations: one where a single RM is present in only one arm waveguide, and another where two RMs are placed in both arm waveguides. When the RAMZM has a structure with a Si RM located in one arm waveguide and that RM is of the depletion type, the configuration is as shown in Fig. 3-6. Here, $E_{out.RM}$ denotes the optical output of the RM, which follows the output field equation for the RM described in chapter 3.2.1. Assuming that the MZI of the RAMZM splits the optical signal via a 1 × 2 MMI and combines it via a 2 × 2 MMI, the output electrical field of the RAMZM, E_{out}, can be expressed in matrix form with respect to the input electrical field E_{in} as follows:

$$\begin{pmatrix} 0 \\ E_{out} \end{pmatrix} = \frac{1}{2}\begin{pmatrix} 1 & j \\ j & 1 \end{pmatrix}\begin{pmatrix} E_{out.RM}\cdot\exp(-j\varphi) & 0 \\ 0 & 1 \end{pmatrix}\begin{pmatrix} 1 \\ 1 \end{pmatrix}E_{in}. \tag{3.6}$$

(3.6) can be expressed by

$$E_{out} = \frac{1}{2}\cdot E_{in}\cdot\left[j\cdot E_{out.RM}\cdot\exp\left(-j\varphi\right)+1\right]. \tag{3.7}$$

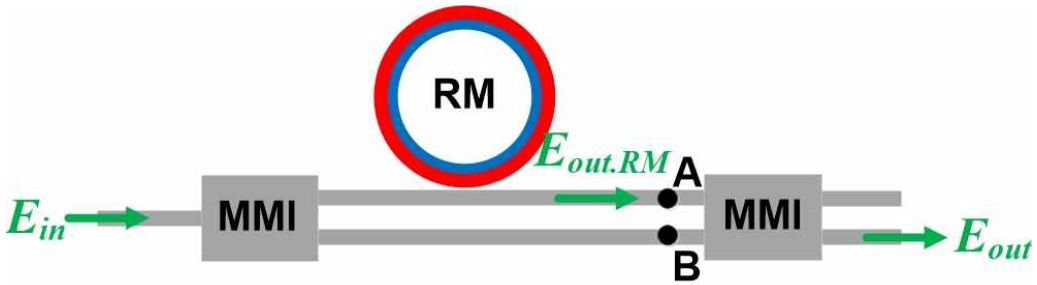

Fig. 3-6. Diagram of an RAMZM with a Single RM.

Here, φ represents the initial phase difference between the two arm waveguides. For high modulation efficiency and linearity, φ is typically fixed at 0, corresponding to the quadrature bias point. When a reverse bias voltage is applied to the ring, the effective refractive index and absorption coefficient change, which in turn alters E_{out}.

Fig. 3-7 and 3-8 show the optical transmission and phase at each point in Fig. 3-6. In the arm waveguide without an RM (point B), there is no change in either phase or intensity. In contrast, the output transmission from the RM (point A) follows the shape described in chapter 3.2.1, exhibiting its lowest intensity at the resonance wavelength (optical detuning = 0). Additionally, the phase change between the RM's input and output is shown in Fig. 3-7(b), which illustrates the over-coupling case. The optical output transmission curves of the RAMZM under the conditions of Fig. 3-7 and 3-8 and an MZM is shown in Fig. 3-9. Compared with the cosine characteristic of a conventional MZM, the RAMZM's transmission

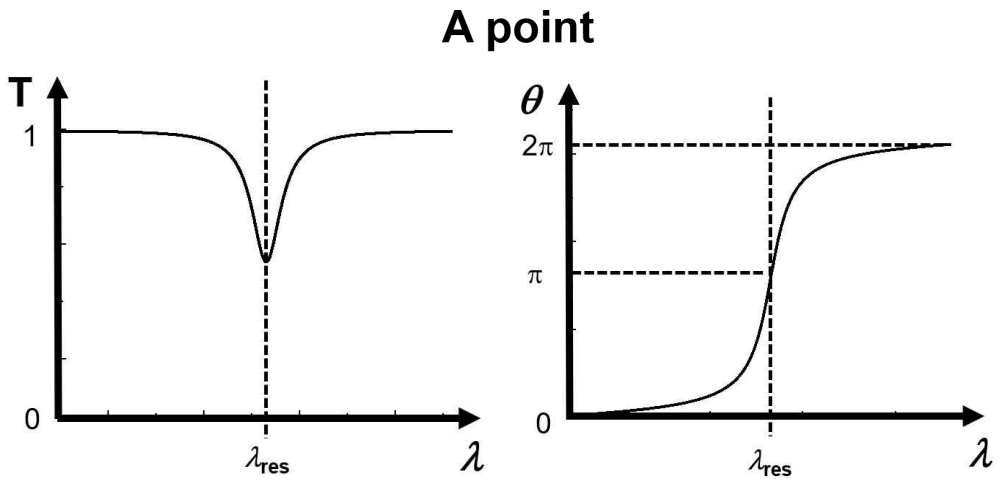

(a) (b)

Fig. 3-7. (a) Optical transmission curve and (b) phase at A point in Fig 3-6.

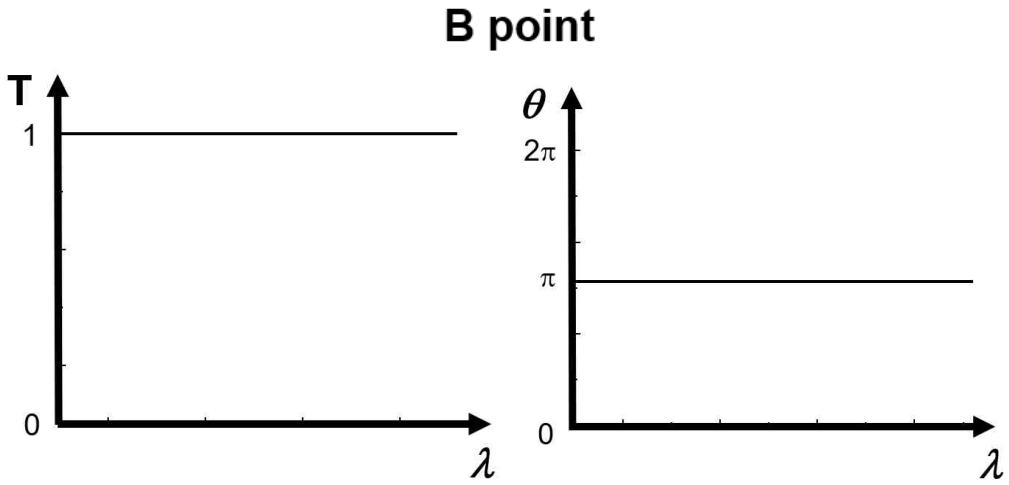

(a) (b)

Fig. 3-8. (a) Optical transmission curve and (b) phase at B point in Fig 3-6.

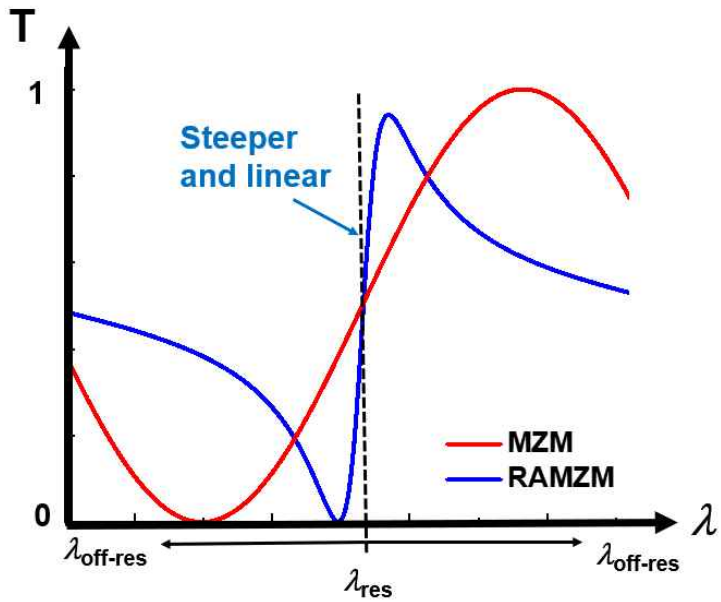

Fig. 3-9. Optical transmission curves of both MZM and RAMZM.

curve has its steepest slope at the resonance wavelength λ_{res}, which is a detuning of 0 and the shallowest slope at off-resonance positions $\lambda_{off\text{-}res}$, where the detuning is π or $-\pi$. This unique shape allows the RAMZM to achieve higher linearity, improved SFDR, and greater modulation efficiency at the resonance wavelength [108].

When two RMs are present in the RAMZM, the structure becomes that shown in Fig. 3-10, where the microwave signal is split and differentially applied to each RM. $E_{out.RM1}$ and $E_{out.RM2}$ represent the optical outputs of each RM, and in this case, (3.7) is modified as follows:

$$E_{out} = \frac{1}{2}\begin{pmatrix} 1 & j \\ j & 1 \end{pmatrix}\begin{pmatrix} E_{out.RM1}\cdot\exp(-j\varphi) & 0 \\ 0 & E_{out.RM2} \end{pmatrix}\begin{pmatrix} 1 \\ 1 \end{pmatrix}E_{in}. \tag{3.8}$$

(3.8) can be expressed by

$$E_{out} = \frac{1}{2}\cdot E_{in}\cdot\left[j\cdot E_{out.RM1}\cdot\exp\left(-j\varphi\right)+E_{out.RM2}\right]. \tag{3.9}$$

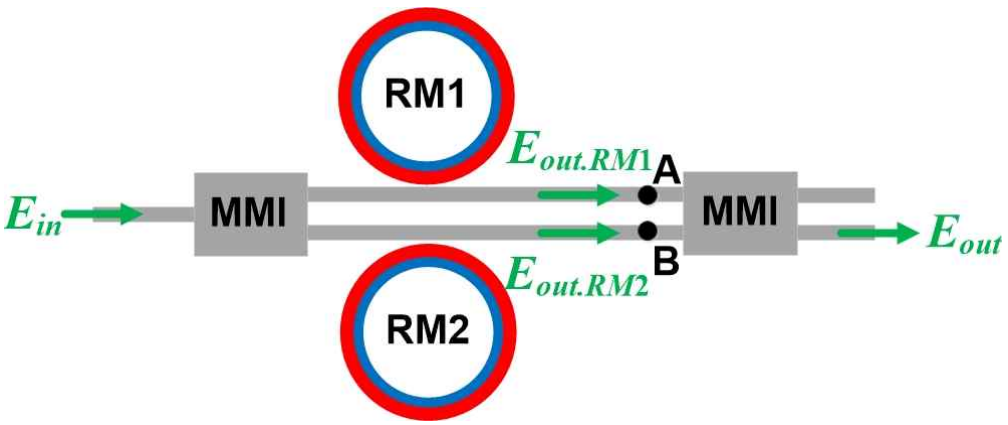

Fig. 3-10. Diagram of an RAMZM with two RMs.

When the microwave signal input to the RAMZM is applied differentially to each RM, the optical transmissions of both RMs must be identical. Therefore, the resonance wavelengths of both RMs ($\lambda_{res.RM1}$ and $\lambda_{res.RM2}$) are also same each other. Fig. 3-11(a) shows the optical transmission of the two RMs. When the optical signal at the resonance wavelength of the RMs and the bias voltages v_b are applied in a differential manner, the resulting transmission follows the shape shown in Fig. 3-11(b). This shape closely resembles that in Fig. 3-9, as the phase response of the RMs ultimately determines the optical transmission of the RAMZM. Additionally, voltage response of the RAMZM is steeper than that of MZM, so that can make stronger fundamental signal and higher SFDR.

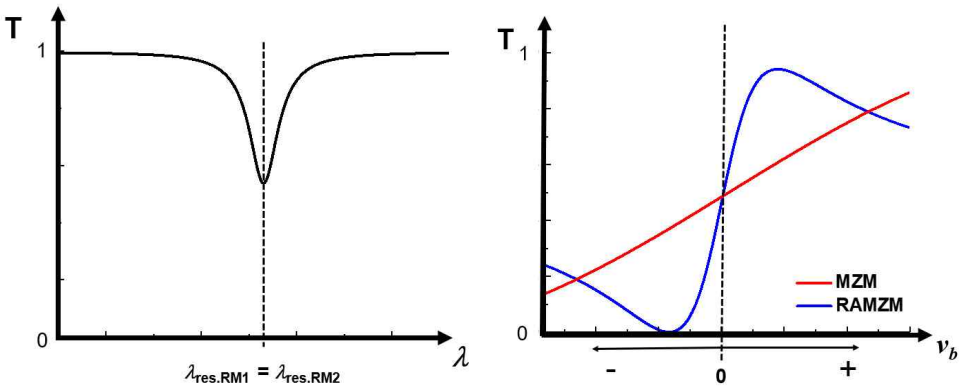

(a) (b)

Fig. 3-11. (a) Optical transmission curve of two RMs and (b) optical transmission of MZM and RAMZM along bias voltage v_b.

3.3. Fabrication

To realize a Si-based EO modulator with high linearity that can operate in the high microwave frequency range above 10 GHz, this study fabricated the Si RAMZM described above using a Advanced Micro Foundry PIC process. The Si RAMZM was fabricated through the MPW service provided by Advanced Micro Foundry. A photograph of the fabricated device is shown in Fig. 3-12(a), and its schematic layout is illustrated in Fig. 3-12(b). The Si RAMZM is based on a MZI structure, with each arm incorporating a RM implemented using MMIs, as explained in chapter 3.1. Optical signals are coupled into and out of the chip via grating couplers. To allow monitoring of the optical signals from each RM, additional waveguides are integrated into both arms of the MZI. Additionally, thermo-optic heaters are embedded in each arm to enable fine tuning of the MZI's optical bias through thermal control. The operating bias of the MZI must be set to the quadrature point for optimal modulation performance, which is accomplished using these heaters.

The overall footprint of the Si RAMZM is approximately 1.45 mm × 0.7 mm. Each RM also includes an integrated thermo-optic heater to tune its operating point. A tunable coupler, implemented using a 2×2 MZI-based thermo-optic switch, is placed on one side of each RM, allowing dynamic adjustment of the coupling coefficient κ between the through port and the ring waveguide. The two RMs used in the RAMZM are depletion-type modulators. Fig. 3-12(c) shows the cross-sectional view of one RM. The Si RAMZM can operate using both a single-ended and differential modulation scheme, which is known to enhance

linearity by suppressing even-order harmonics in the phase response of the ring modulators [94], as mentioned in chapter 3.2.3.

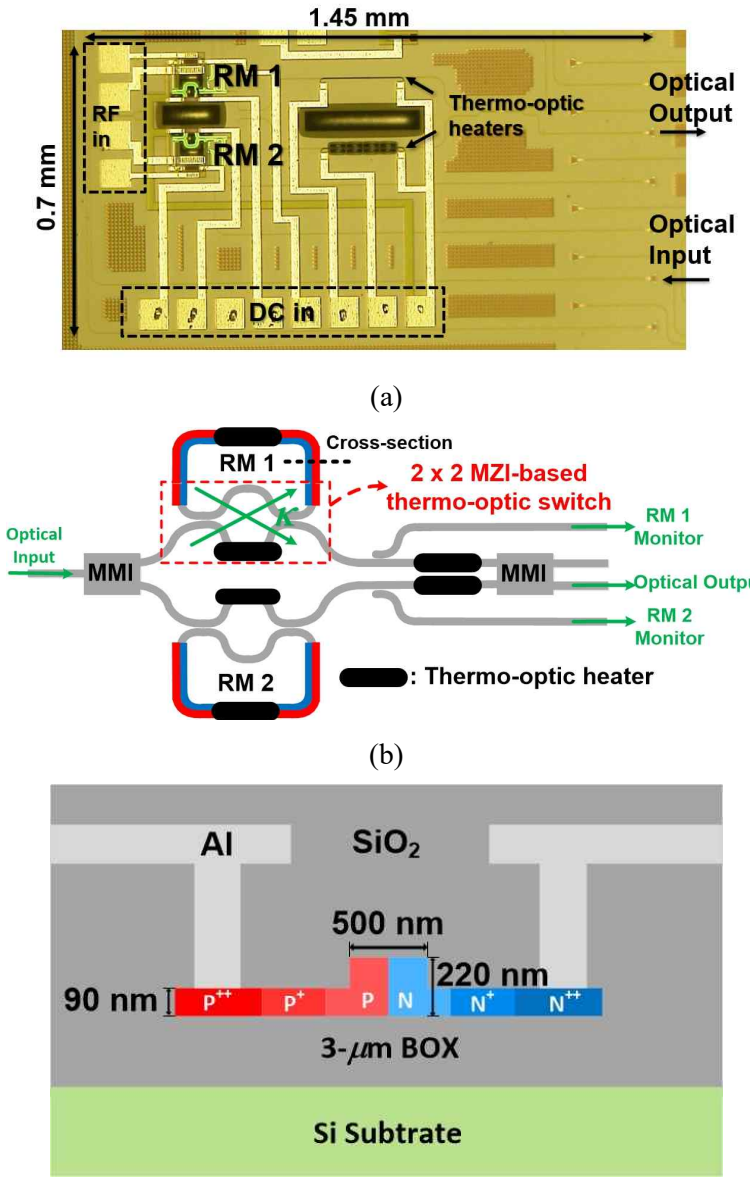

Fig. 3-12. (a) Chip photograph of the Si RAMZM,
(b) its schematic diagram, and (c) cross-sectional view of PN junction in RMs.

3.4. Linearity Simulation

To assess the linearity of the fabricated RAMZM prior to measurement, a simulation model was established, and a linearity simulation was performed using this model. Fig. 3-13 shows a diagram of the simulation model. The model takes the simulated output optical signals, $E_{out.RM1}$ and $E_{out.RM2}$, from the RMs within the RAMZM, which are generated in response to the input voltage v_{in}(t), and inputs them into the MZI that constitutes the RAMZM. The simulation for the RMs involves simulating the modification of the voltage signal due to the electrical part of the RM, followed by the simulation of the optical dynamic transmission that occurs as a result of the modified signal, v_e(t). The output optical signal from the RAMZM is converted into an electrical signal by a PD, and by performing a Fourier transform on this signal, the output RF spectrum is obtained.

Typically, other studies have used a large-signal model based on the coupled-mode equation (CME) to simulate optical dynamic transmission [61], [109]. However, the CME-based large-signal model exhibits a significant

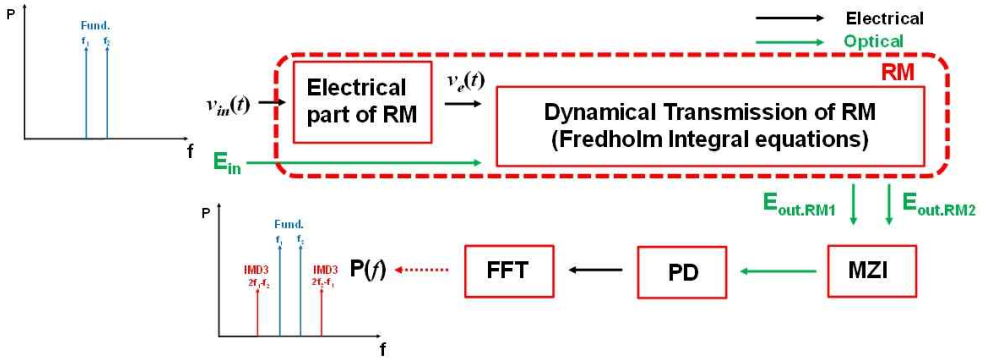

Fig. 3-13. Diagram of the simulation model for the linearity of the Si RAMZM.

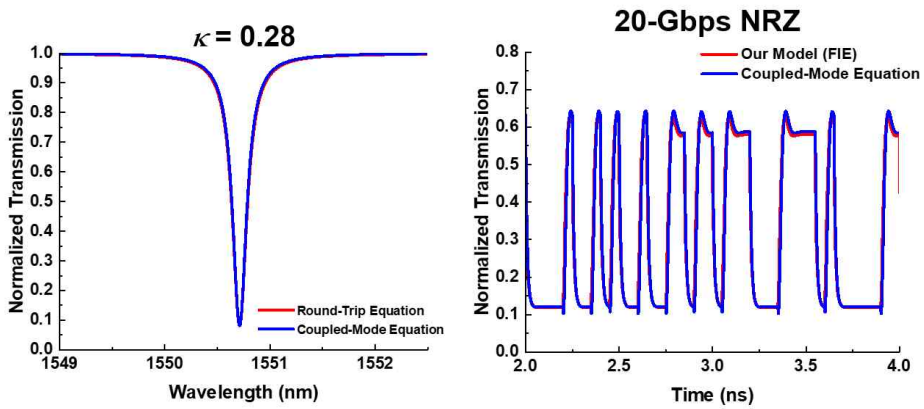

(a) (b)

Fig. 3-14. Comparison between the simulated results of (a) the DC transmission curve and (b) the transient simulation with low κ.

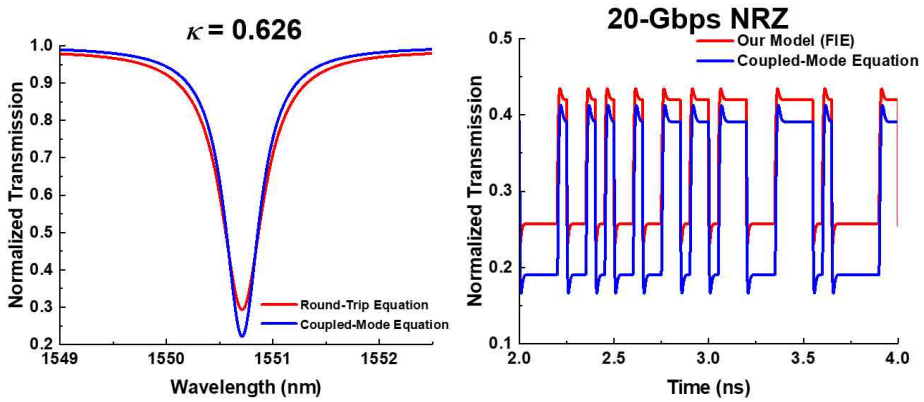

(a) (b)

Fig. 3-15. Comparison between the simulated results of (a) the DC transmission curve and (b) the transient simulation with high κ.

discrepancy from the actual transmission when the coupling coefficient, κ, of the RM becomes large, as the Q-factor of the RM resonator decreases. Since the RAMZM uses RMs with high κ for over-coupling, a different type of large-signal model is required. Therefore, we use a large-signal model constructed from the

round-trip equation (RTE), described in equation (3.1), and the Fredholm integral equation (FIE) [110]. The FIE is a suitable mathematical technique for a large-signal model because it can model heredity and fading memory of the cavity. The equation of the large-signal model with FIE is given by [110]

$$E(t) = r - a(t)e^{-i\phi(t)} + \sum_{n=1}^{\infty} r^n \left[r - a(t-n\tau)e^{-i\phi(t-n\tau)} \right] \times \prod_{m=0}^{n-1} a(t-m\tau)e^{-i\phi(t-m\tau)}. \quad (3.10)$$

$E(t)$ is the output electric field of the RM. r is the straight-through coefficient and a is the optical absorbtion coefficient as mentioned in chapter 3.2.1. ϕ is the round-trip shift of the RM and τ is the round-trip time delay of the RM.

Fig. 3-14(a) and (b) compare the transmission curves of RMs with a low κ of 0.28 and a high κ of 0.626, calculated using both CME and the RTE based on (3.1). While there is no difference in the transmission curves obtained from CME and RTE for a low κ, a significant difference appears for a high κ. Fig. 3-15(a) and (b) compare the large-signal model based on RTE and FIE with the large-signal model based on CME for both low and high κ values, using a 20-Gbps NRZ signal as the input voltage. As with the difference in the transmission curves shown in Fig. 3-14, a difference also exists in the large-signal simulation results.

To simulate the Si RAMZM, we extracted several parameters for the electrical part of the RM, as described in Fig. 3-16(a), through S11 measurements [111]. Fig. 3-16(b) shows the measured S11 values of the RM and the fitting results, from which the electrical parameters of the RM described in 3-16(a) were

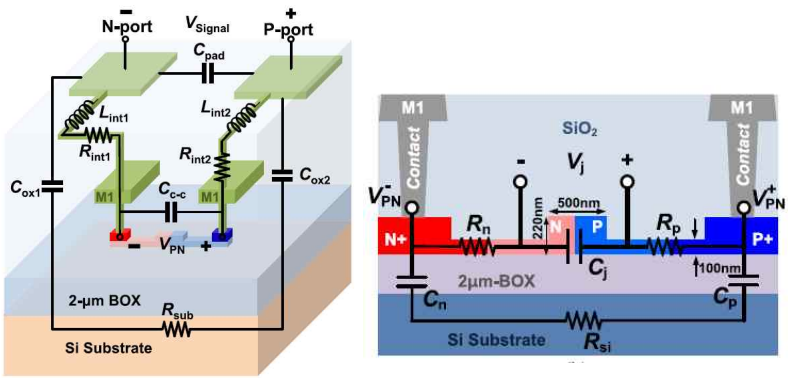

(a)

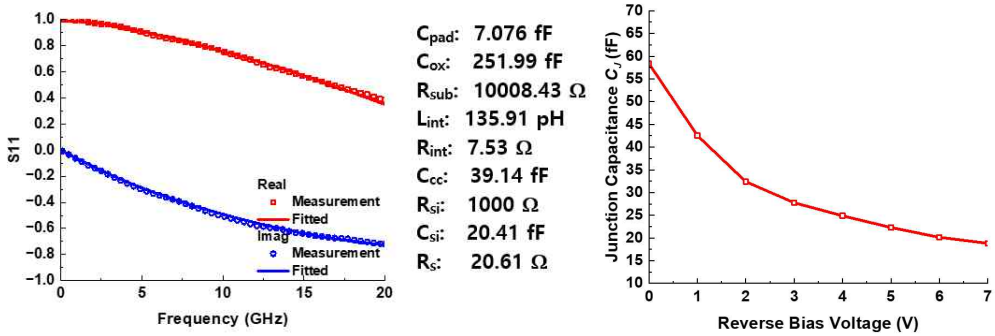

(b) ©

Fig. 3-16. (a) The electrical part of the RM [111], (b) The measured and fitted values of S11 of the RM in the Si RAMZM, and (c) the extracted values of jucntion capacitance of the RM along various bias voltages.

extracted. 3-16(c) presents the junction capacitance of the RM along various bias voltages from the measured S11 values.

Following this, the parameters for the optical dynamic transmission simulation—the effective index, n_{eff}, and the optical absorption coefficient, a—were extracted through experimentation. Fig. 3-17(a) shows the measured transmission curve as a function of the RM bias voltage, and Fig. 3-17(b) and (c) show the extracted n_{eff} and a from these measurements.

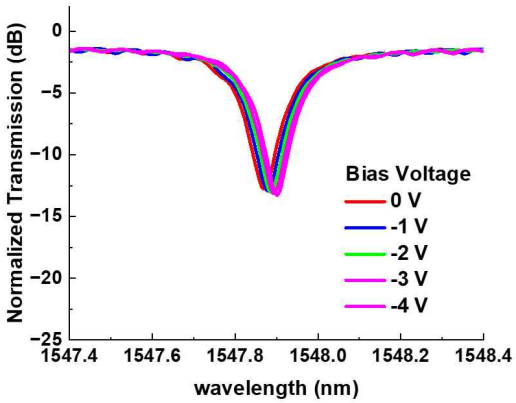

(a)

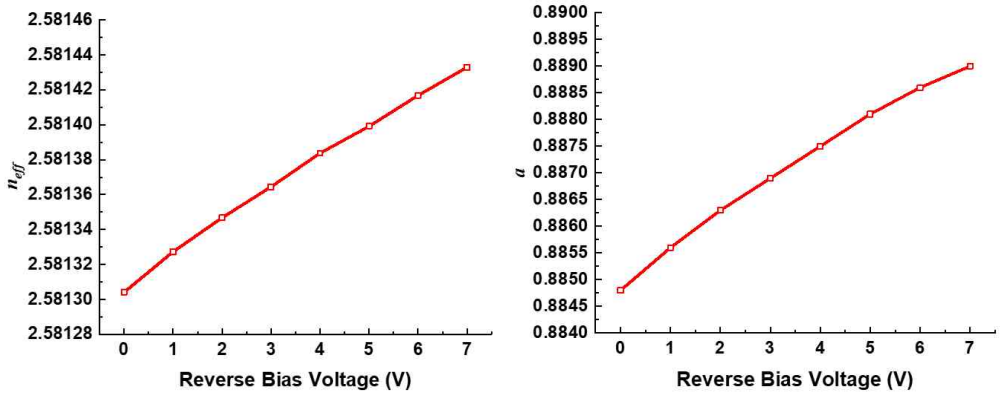

(b) (c)

Fig. 3-17. (a) The measured optical spectrum of the RM. (b) The extracted n_{eff} and (c) the extracted a with various bias voltages.

Using these extracted parameters, we performed the linearity simulation described in Fig. 3-16. A two-tone signal of 9.9 GHz and 10.1 GHz was used as the input microwave signal. The MZI in the Si RAMZM was biased at the quadrature point. The electrical signal was simulated to be input differentially to the two RMs. Fig. 3-18(a) illustrates the output transmission curve of the RAMZM and its internal RMs as a function of wavelength, shown to represent

various bias points for driving the Si RAMZM. Fig. 3-18(b) shows the simulated SFDR values for RMs with various κ values, plotted according to the bias points in Fig. 3-18(a). As mentioned in [108], it shows that the highest SFDR is obtained when biased at resonance wavelength of the RM, no matter what the value of κ is. Additionally, the SFDR values are simulated with various κ and RAMZM bias points, as illustrated in Fig 3-18(c). The highest SFDR is about 104.6 $dB.Hz^{2/3}$, at κ of 0.6 and the resonance wavelength of the RM. Notably, for making high SFDR values, κ of the RM should be more than 0.5, contrary to typical RMs having κ lower than 0.3 for high Q-factor [103], [106], [109], [111].

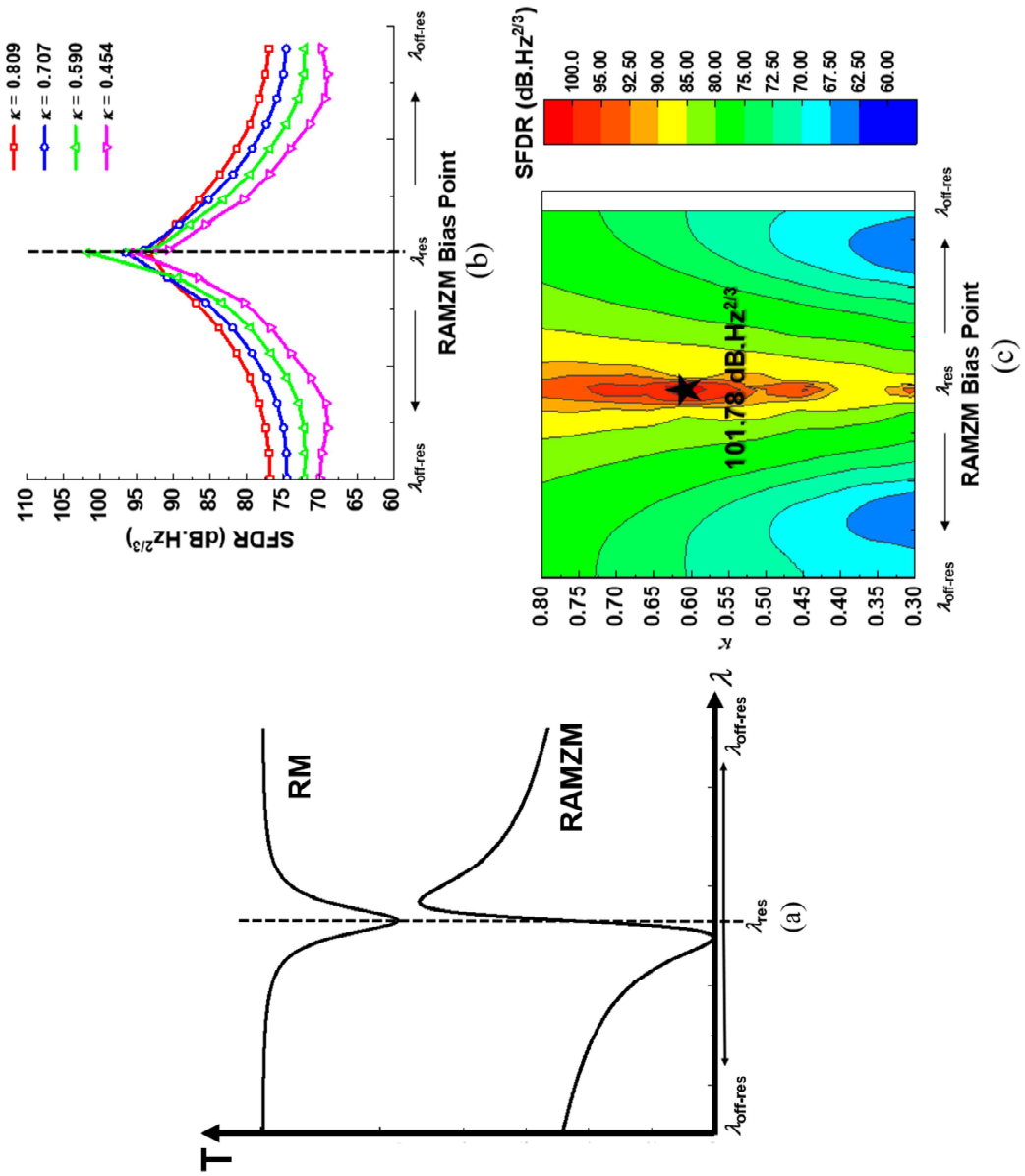

Fig. 3-18. (a) The optical transmission curve of the RAMZM and the RM inside the RAMZM. (b) The simulated SFDR values along various bias points of the Si RAMZM with 9.9-GHz and 10.1-GHz RF signals. (c) The contour map of the simulated SFDR along bias points and κ.

3.5. Measurements

3.5.1 DC Transmission

First, to characterize the 2 × 2 thermo-optic switch inside the fabricated Si RAMZM's RM, which is used to adjust the coupling coefficient g, we measured the RM's transmission by applying a voltage to the heater embedded in the thermo-optic switch of a test RM. Fig. 3-19(a) shows the RM structure within the RAMZM. In the thermo-optic switch located beneath the RM, the ratio of the optical electric field propagating to the through port to the input electric field corresponds to the *r* parameter described earlier. Fig. 3-19(b) illustrates the approximate transmission behavior of the thermo-optic switch in the RM as a function of heater voltage. Since the switch has an MZI configuration, increasing the heater voltage produces a cosine-shaped transmission response, and thus *r* also follows a cosine trend.

Depending on the relationship between *a* and *r*, there are four distinct coupling cases, and we measured the RM characteristics for each case.

Case 1 corresponds to an over-coupling condition where *a* is greater than *r*, and *r* decreases as the heater voltage increases. The RM transmission for case 1 is shown in Fig. 3-20(a), which presents the measured transmission curves when the thermo-optic switch is driven at the heater voltages corresponding to this case. As the heater voltage increases, *r* decreases, moving farther from *a*. This shifts the RM from critical coupling condition toward stronger over-coupling regime, causing the minimum value of the transmission curve to increase. Fig. 3-20(b) shows the transmission when 0.8-V heater voltage is applied along with a reverse bias

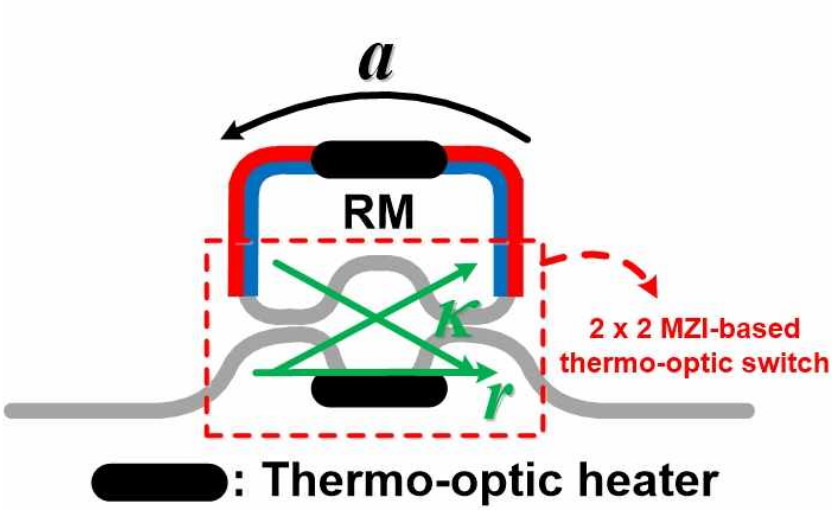

(a)

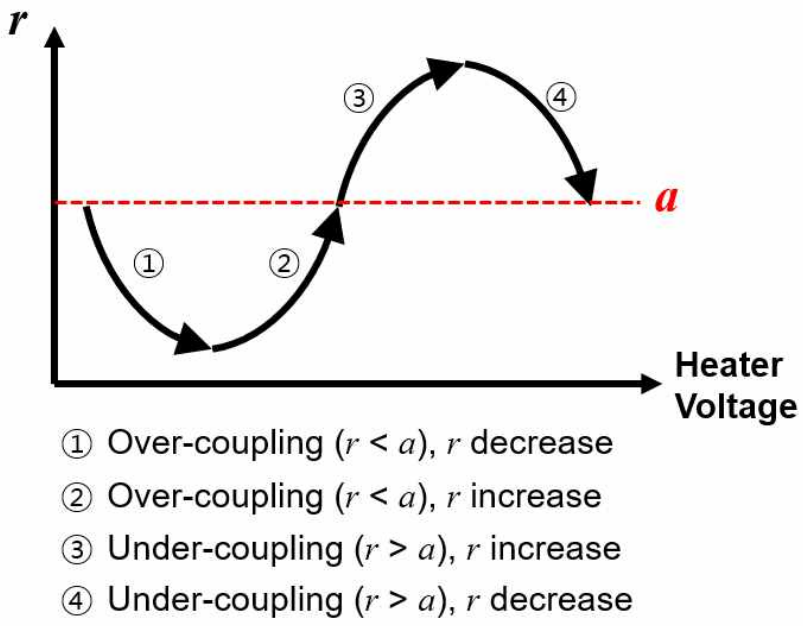

(b)

Fig. 3-19. (a) Diagram of the RM in the Si RAMZM and (b) the operation of the thermo-optic switch in the RM and its four cases.

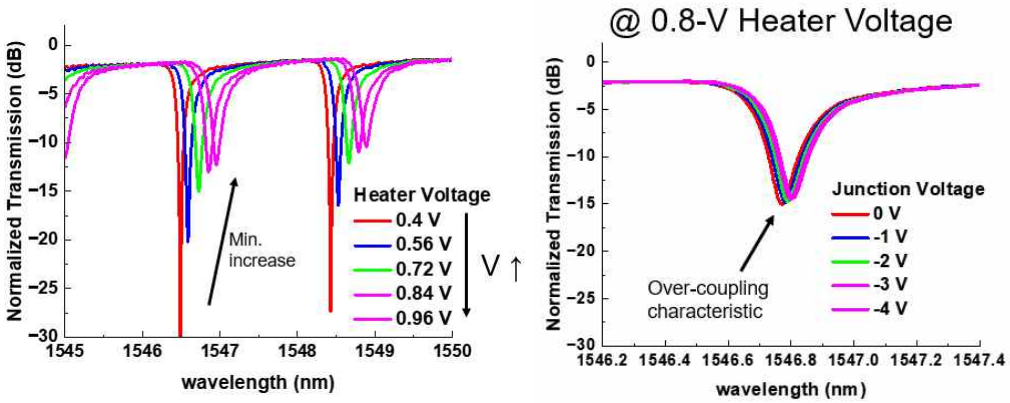

(a) (b)

Fig. 3-20. (a) Optical transmission curves with the condition of case 1 and (b) optical transmission curves of the RM along junction voltages.

voltage to the PN junction. As the reverse bias voltage increases, the minimum transmission value also increases, confirming the over-coupling.

Case 2 corresponds to an over-coupling condition where a is greater than r, and r increases with heater voltage. The RM transmission for this case is shown in Fig. 3-21(a), which presents the measured transmission curves when the thermo-optic switch is driven at heater voltages corresponding to case 2. As the heater voltage increases, r increases and approaches a, causing the RM to transition from an over-coupling state toward critical coupling. Consequently, the minimum value of the transmission curve decreases with increasing heater voltage. Fig. 3-21(b) shows the transmission when 1.3-V heater voltage is applied together with a reverse bias voltage to the PN junction. As the reverse bias voltage increases, the minimum transmission value rises, confirming that the RM remains in an over-coupling regime.

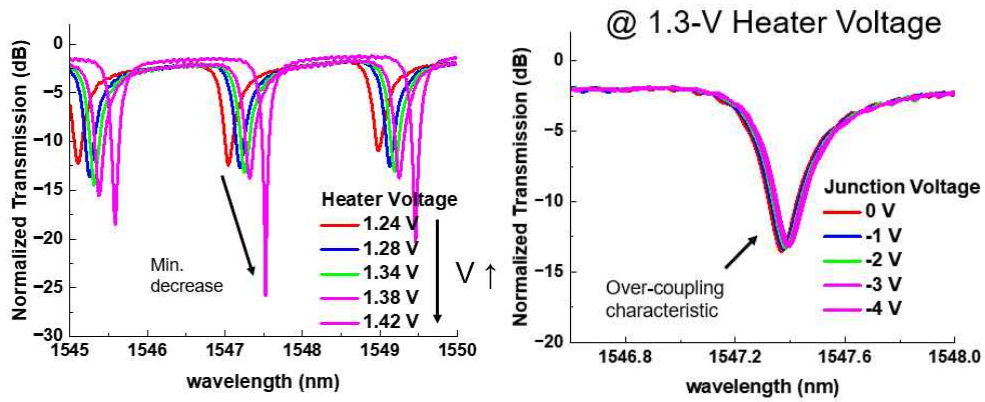

(a) (b)

Fig. 3-21. (a) Optical transmission curves with the condition of case 2 and (b) optical transmission curves of the RM along junction voltages.

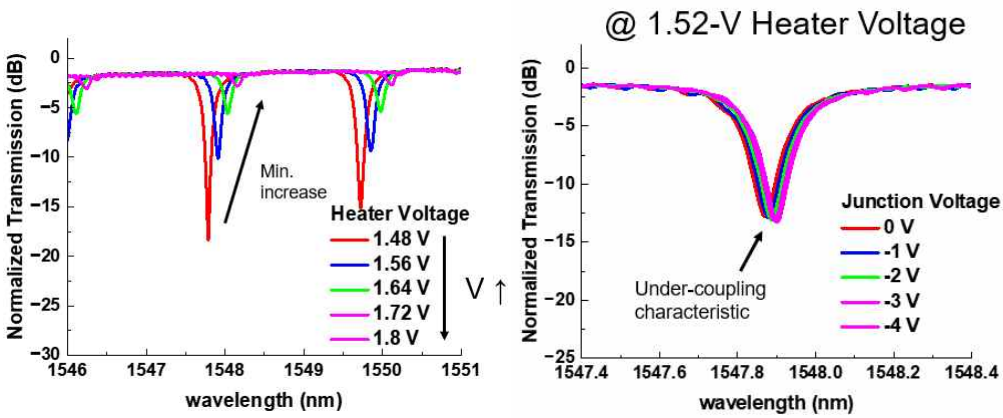

(a) (b)

Fig. 3-22. (a) Optical transmission curves with the condition of case 3 and (b) optical transmission curves of the RM along junction voltages.

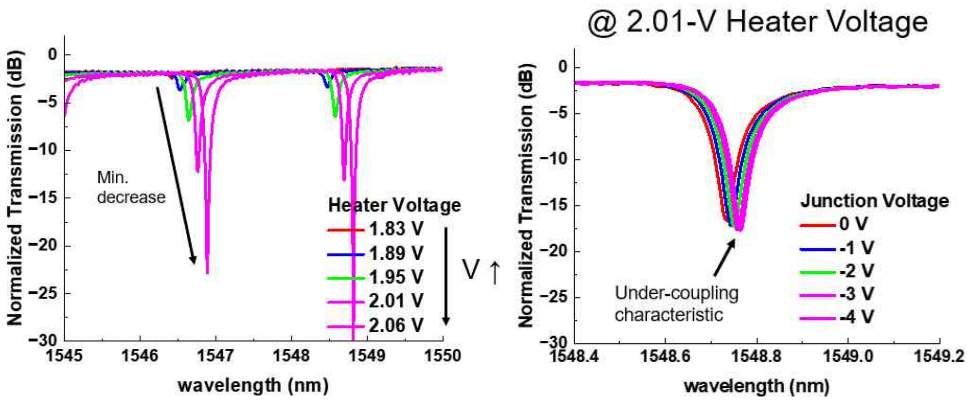

(a) (b)

Fig. 3-23. (a) Optical transmission curves with the condition of case 4 and (b) optical transmission curves of the RM along junction voltages.

In case 3, the RM operates in an under-coupling regime where *a* is smaller than *r*, and *r* rises as the heater voltage increases. Fig. 3-22(a) illustrates the measured transmission curves for heater voltages under these conditions. As the heater voltage grows, *r* moves further away from a, shifting the RM from critical coupling toward under-coupling state. Consequently, the minimum point of the transmission curve becomes higher. When 1.52-V heater voltage is applied along with a reverse bias on the PN junction, as shown in Fig. 3-22(b), the minimum transmission level decreases with increasing reverse bias voltage, verifying the under-coupling behavior.

Case 4 represents an under-coupling scenario where *a* is smaller than *r*, and *r* decreases as the heater voltage increases. Fig. 3-23(a) illustrates the measured RM transmission curves for heater voltages in this condition. With higher heater voltage, *r* decreases and moves closer to *a*, shifting the RM from an

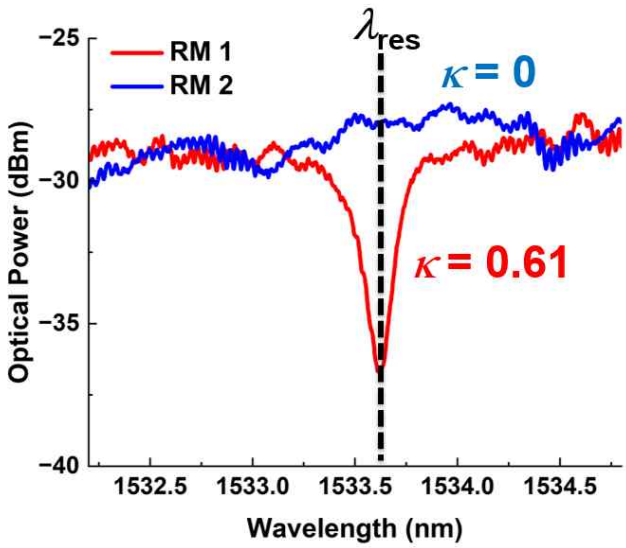

Fig. 3-24. The measured optical spectra of two RMs monitored from the monitoring ports for single-ended modulation scheme.

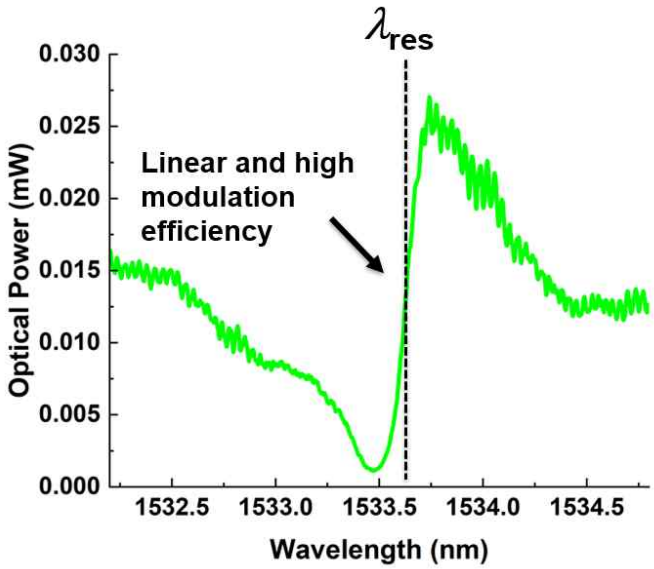

Fig. 3-25. The measured optical spectrum of the Si RAMZM.

under-coupled state toward critical coupling. As a result, the minimum value of the transmission curve decreases with increasing heater voltage. Fig. 3-23(b) shows the transmission when 2.01-V heater voltage is applied together with a reverse bias on the PN junction. In this case, the minimum transmission also decreases as the reverse bias voltage increases, reaffirming the under-coupling behavior.

Considering all four cases, it can be concluded that the thermo-optic switch in the RM successfully performs its role of adjusting g in response to the applied heater voltage.

As described in chapter 3.2.2, proper RAMZM operation requires the use of an over-coupling condition, such as in cases 1 and 2. Under this over-coupling condition, the wavelength-dependent transmission of the RAMZM was measured. In the single-ended modulation scheme, r for one of the RMs is set to 1, and that is the same with the condition that κ is 0. Fig. 3-24 shows the transmission measured at the monitoring optical ports of each arm waveguide when the thermo-optic switch in the RMs of the RAMZM is configured for single-ended modulation. In Fig. 3-24(a), the transmission curve of one of the RMs shows no variation with wavelength, which is due to r being set to 1. The κ of the other RM is set to 0.61, which is around 0.6, to make the highest SFDR.

Fig. 3-25 presents the output optical transmission of the RAMZM under the same conditions as in Fig. 3-24. As discussed in chapter 3.2.2, the slope near the resonance wavelength is steep, resulting in high modulation efficiency and improved linearity.

Fig. 3-26 shows the optical transmission of the output of the RMs at the monitoring ports, when the differential modulation scheme is used for driving the

RAMZM. The κ and resonance wavelength of the two RMs are set to the same value, so that those optical transmission curves are nearly matched.

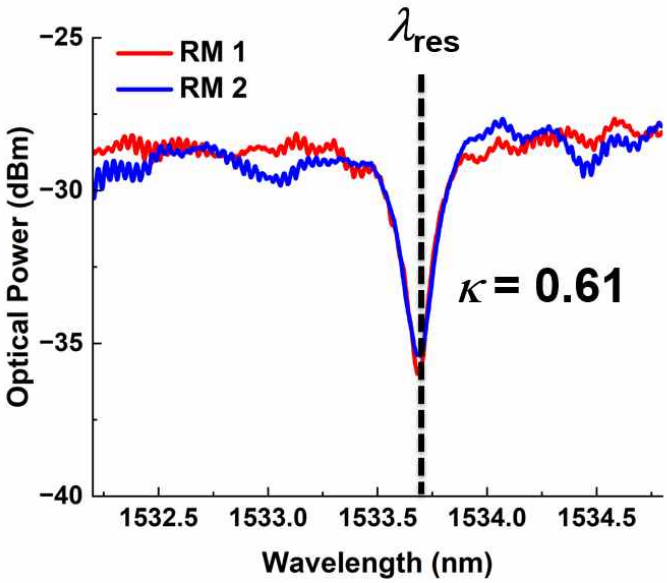

Fig. 3-26. The measured optical spectrum of two RMs for differential modulation scheme.

3.5.2 Linearity

To experimentally assess the linearity of the Si RAMZM, a two-tone test was conducted by injecting a microwave signal consisting of two closely spaced frequencies and analyzing the resulting output spectrum. The SFDR was determined by measuring the power levels of both the fundamental tones and the nearest IMD components. Fig. 3-27(a) and (b) illustrate the experimental setup used for the two-tone measurement. Fig. 3-27(a) is for single-ended modulation scheme, and Fig. 3-27(b) is for differential modulation scheme. A tunable laser provides the optical carrier, while two separate RF signal generators produce the microwave tones, which are combined using an RF combiner. A balun is employed to generate two differential signals—180 degrees out of phase—used to drive the two ring modulators for differential modulation. The Si RAMZM is placed on a temperature-controlled stage for making the device temperature 25 °C.

The modulated optical signal is detected by a high-speed photodetector (Coherent XPDV2320R-VF-FA), and the resulting electrical signal is analyzed using an RF spectrum analyzer (Keysight N9000B). To ensure the output signal exceeds the analyzer's minimum detection threshold, it is amplified using an RF amplifier (SHF S807C).

To characterize the device's linearity in the X-band, microwave signals near 10 GHz were applied. Fig. 3-28(a) and (b) presents the measured RF output spectrum when the input signal consists of two tones at 9.9 GHz and 10.1 GHz, each with an input power of 7.5 dBm for single-ended and differential modualation respectively. IMD components are clearly visible at 9.7 GHz and 10.3 GHz. The results between the two modulation scheme show that the ratio IMD signal to

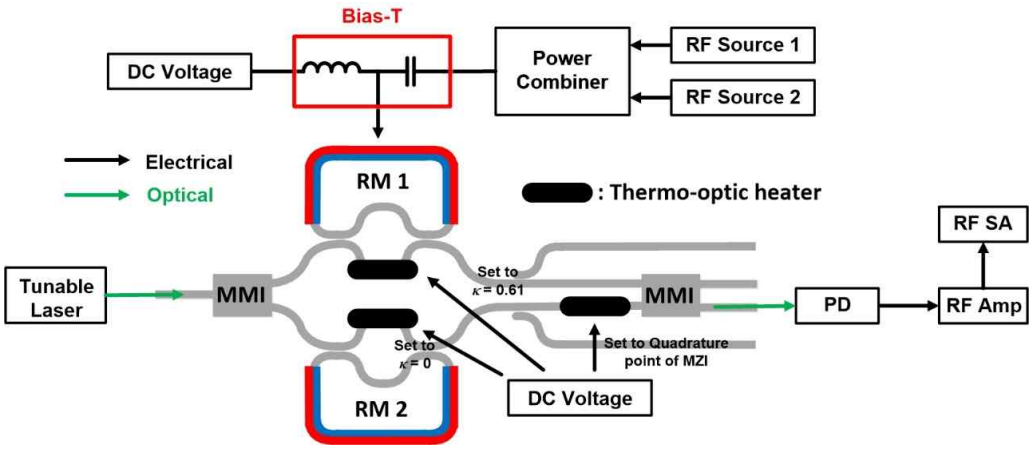

(a)

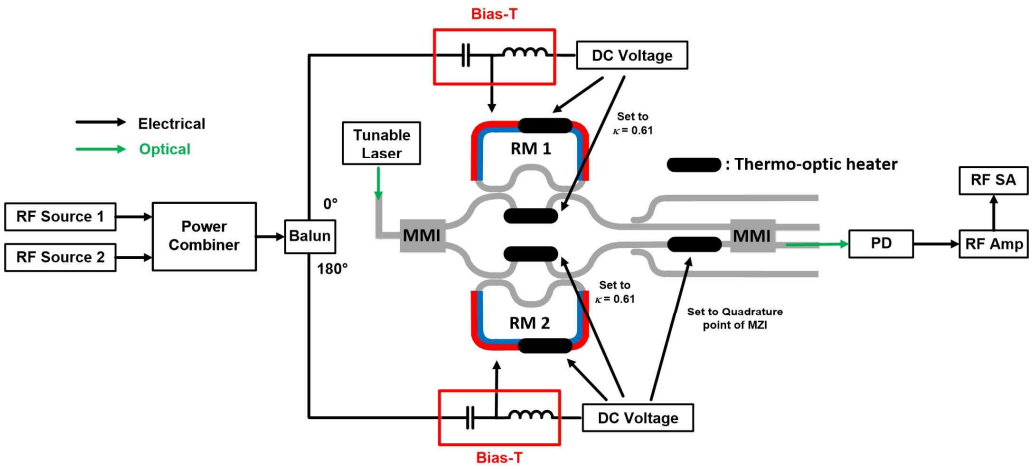

(b)

Fig. 3-27. Experimental setup for (a) the single-ended modulation and (b) the differential modulation. PD: photodetector, RF Amp: RF amplifer. RF SA: RF spectrum analyzer.

fundamental signal can be improved when the RAMZM is used with differential modulation scheme. All even-order distortions are ideally calcelled out resulting from differential, and this can make IMD components reduced [94].

As described in chapter 2.3.4, the noise floor is calculated based on the average optical power incident on the photodetector. For the exampled of our experiment with differential scheme, when the MZI in the Si RAMZM is biased at the quadrature point and the input laser wavelength aligns with the resonance of the RM, an input optical power of 4 dBm yields an output power of –5.5 dBm. This corresponds to a photocurrent of 0.282 mA. Given the laser's relative intensity noise (RIN) of –140 dB/Hz, the resulting RIN noise power is –167.8 dBm, while the shot noise power is calculated as –172.8 dBm. At a measurement temperature of 25 °C, the thermal noise power is –173.9 dBm. Combining these contributions results in an overall noise floor of –166.2 dBm/Hz after the PD. With RF amplifier gain of 23 dB, assuming it has zero noise figure to get SFDR values of the Si RAMZM itself, the effective noise floor becomes –143.2 dBm/Hz for

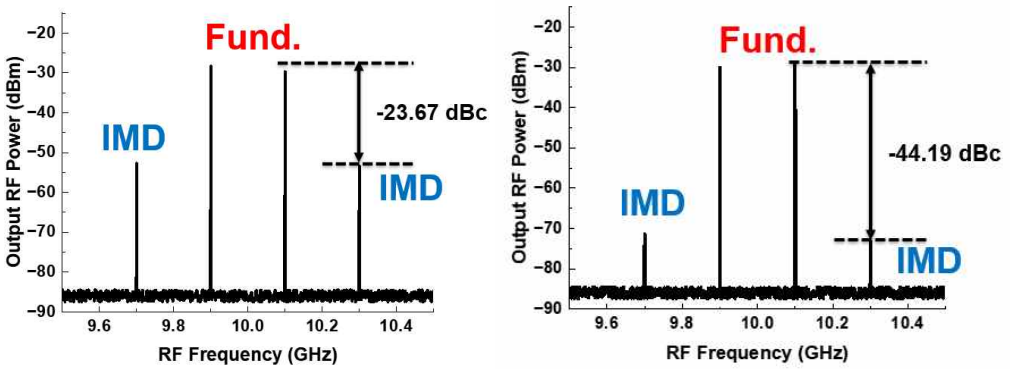

(a) (b)

Fig. 3-28. RF spectra of the output microwave signals with (a) the single-ended modulation and (b) the differential modulation. Input RF power is 7.5 dBm.

differential scheme. The effective noise floor for the single-ended scheme is –139 dBm/Hz, because the average optical output power of the RAMZM becomes larger, when the single-ended scheme is applied.

Fig. 3-29(a) and (b) present the measured power of the fundamental tones and the nearest IMD components as a function of input microwave power at RF C band and X band each with the single-ended modulation scheme illustrated in Fig. 20(a). The extracted SFDR value is 106.8 $dB \cdot Hz^{6/7}$ is made with 4-GHz microwave signal. Additionally, the Si RAMZM demonstrates SFDR greater than 105 $dB \cdot Hz^{6/7}$ at RF X band.

Fig. 3-30(a) and (b) plot the measured power of the fundamental tones and the nearest IMD components as a function of input microwave signal power at RF C band and X band. SFDR value of 106.8 $dB \cdot Hz^{6/7}$ is made with 4-GHz microwave

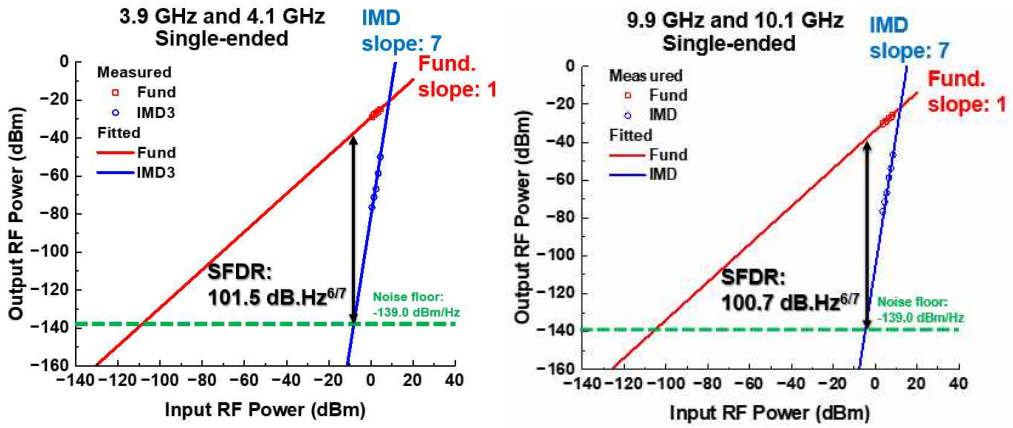

(a) (b)

Fig. 3-29. The output RF power of fundamental and IMD signals along the input RF power and its corresponding SFDR values with (a) 3.9-GHz and 4.1-GHz RF signals; and (b) 9.9-GHz and 10.1-GHz RF signals. The single-ended modulation scheme is used.

signal. Additionally, the Si RAMZM demonstrates SFDR greater than 105 dB·Hz$^{6/7}$ at RF X band. Notably, unlike the simulated results, the slope of the IMD traces is approximately 7 in both modulation scheme, indicating that 7th-order distortion dominates the nonlinear behavior of the device, and that makes more SFDR than the simulation.

Fig. 3-31 shows the measured SFDR of the Si RAMZM according to its bias point. Fig. 3-31(a) illustrates the transmission of the Si RAMZM and its internal RM as a function of wavelength. Fig. 3-31(b) shows the SFDR at each point in Fig. 3-31(a) for 4-GHz microwave signal, while Fig. 3-31(c) shows the measured SFDR for 10-GHz microwave signal. These results indicate that the highest SFDR can be achieved when the bias point of the Si RAMZM is located at the resonance wavelength of the RM. This is because the Si RAMZM has its highest

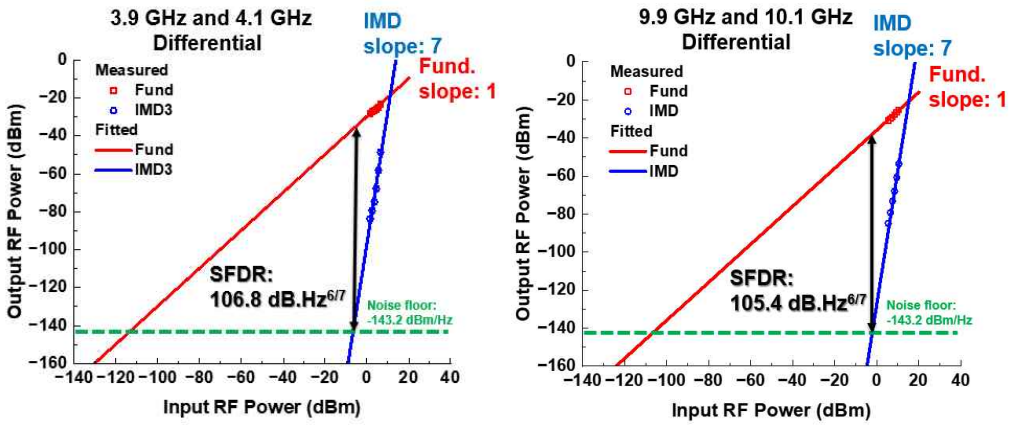

(a) (b)

Fig. 3-30. The output RF power of fundamental and IMD signals along the input RF power and its corresponding SFDR values with (a) 3.9-GHz and 4.1-GHz RF signals; and (b) 9.9-GHz and 10.1-GHz RF signals. The differential modulation scheme is used.

modulation efficiency and linearity when it is biased at resonance wavelength of the RM.

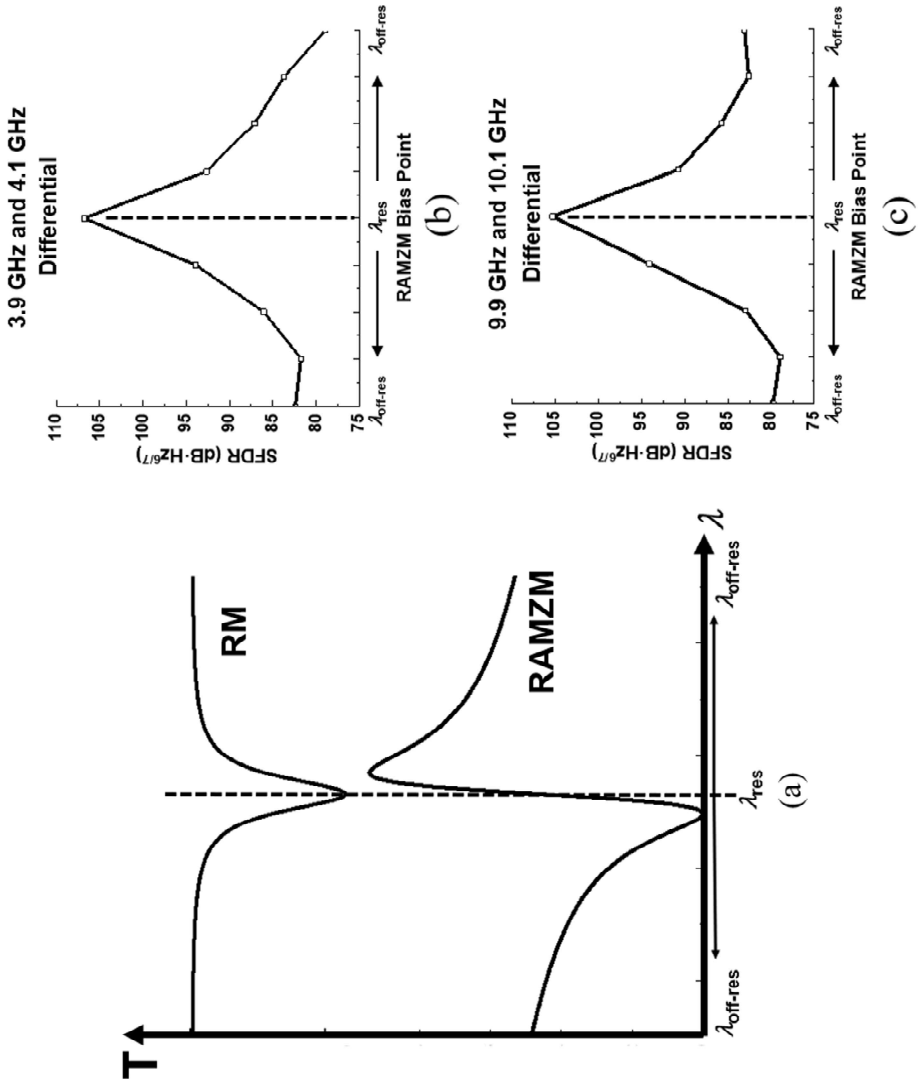

Fig. 3-31. (a) The optical transmission curve of the RAMZM and the RM inside the RAMZM. The measured SFDR values along various bias points of the Si RAMZM with (b) 3.9-GHz and 4.1-GHz RF signals; and (c) 9.9-GHz and 10.1-GHz RF signals.

Table 3-1 compares previous studies on the linearity for Si-based EO modulators with the work presented in this study. EO modulators based on other materials such as $LiNbO_3$ and III-V materials achieve SFDR values exceeding 110 dB in frequency ranges above 10 GHz, owing to the inherently high linearity of these materials. On the other hand, for Si-based EO modulators, higher linearity has been achieved by employing non-conventional structures, such as DSMZMs, DPMZMs, and RAMZMs [92]-[94], [115]. However, DSMZMs and DPMZMs require two conventional MZMs, resulting in a very large footprint, and previously demonstrated RAMZMs have only operated in low-frequency ranges of around 1 GHz. In contrast, the RAMZM developed in this work achieves an SFDR exceeding 105 dB at 10 GHz, while maintaining a compact footprint, offering a significant advantage. If figure of merit is set as the SFDR value divided by device footprint, it is confirmed that the Si RAMZM presented in this work exhibits markedly higher value compared to other Si EO modulators.

Table 3-1. The linearity comparison of Si-based EO modulators.

Ref.	Device structure	Device Footprint (mm^2)	Microwave Signal Frequency (GHz)	SFDR	Figure of Merit (SFDR / Footprint)
[112]	RM	-	1	103.6 $dB.Hz^{2/3}$	-
[113]	RM	-	10	94.7 $dB.Hz^{2/3}$	-
[114]	MZM	8	2	113.7 $dB.Hz^{2/3}$	14.2
[92]	DSMZM	5	10	127 $dB.Hz^{6/7}$	25.4
[115]	DPMZM	6.4	10	96.5 $dB.Hz^{2/3}$	15.1
[93]	RAMZM	15	10	99 $dB.Hz^{2/3}$	6.6
[94]	RAMZM	1.38	1.1	113 $dB.Hz^{2/3}$	81.9
This work	RAMZM	1.02	10	105.4 $dB.Hz^{6/7}$	103.3

3.6. Summary

In this research, A Si RAMZM is designed for MWP systems requiring high linearity. The proposed modulator achieves an exceptionally high SFDR of 105.4 $dB \cdot Hz^{6/7}$ at 10 GHz (X band), while maintaining a compact footprint of only ~1 mm^2. This performance is enabled by a differential modulation scheme and the use of two depletion-mode Si RMs, which are integrated into each arm of the MZI. The device is thermally tunable to ensure optimal optical biasing, which is resonance wavelength of the RMs, and coupling conditions.

To characterize linearity, two-tone measurements are conducted, revealing a dominant 7th-order IMD rather than typical 3rd-order, indicating improved linear behavior. The design employs ring resonance tuning, thermo-optic control, and voltage-to-phase compensation techniques to suppress lower-order IMDs.

Compared to other modulators including DPMZMs, DSMZMs, and standard Si MZMs, this RAMZM offers competitive linearity with minimal area. These features position the proposed modulator as a strong candidate for next-generation MWP systems requiring compactness and high fidelity.

4. Discussion

4.1. Comparison between Si EO Modulators

Si MZM and RAMZM exhibit significant differences in their linearity and optical DC transmission characteristics. This chapter will provide a detailed comparison of these two Si EO modulator architectures.

A standard Si MZM is based on a MZI structure and utilizes the plasma dispersion effect in silicon to achieve phase modulation. The fundamental optical transfer function of the MZM is inherently nonlinear, following a cosine relationship relative to the phase difference between its two arms. This cosine response is the primary source of intrinsic nonlinearity, causing signal distortion even in an ideal modulator.

In a practical Si MZM, this linearity is further degraded by nonlinear factors stemming from the PN junction used for phase shifting. Two sources are particularly critical. First, the change in the effective refractive index n_{eff} induced by the plasma dispersion effect is not linear with the applied voltage. Analysis reveals that n_{eff} has an approximately square-root dependence on the bias voltage, making it a primary contributor to overall transfer function nonlinearity of the MZM.

Second, the junction capacitance C_J of the PN junction is also voltage-dependent. This variable capacitance introduces a significant source of electrical nonlinearity, which is identified as a key factor degrading linearity, especially at higher bias voltages. Consequently, the performance of a realistic Si

MZM is compromised by this combination of its intrinsic optical (cosine) nonlinearity and these extrinsic electrical nonlinearities n_{eff} and C_J.

To overcome these limitations, the RAMZM structure was proposed. The RAMZM architecture integrates an RM into one or both arms of the base MZI structure. The core principle of the RAMZM is to use the ring resonator's sharp and nonlinear voltage-to-phase characteristics to compensate for the MZM's compressive phase-to-intensity response.

The RAMZM leverages the steep changes in optical intensity and phase that occur near the RM's resonance wavelength. By operating the RM in an over-coupling condition, the phase response of the MZI arm is intentionally modified. This results in the RAMZM's overall voltage-to-optical-output transfer function having a much steeper slope compared to that of a standard MZM, as shown in Fig. 3-9 and 3-11(b).

The Si MZM and RAMZM described in this dissertation have V_π values of 12 V and 8 V, respectively. This indicates that the Si RAMZM possesses a higher modulation efficiency than the standard Si MZM.

This steeper transfer function slope is the key to its improved performance. It allows the RAMZM to generate a stronger fundamental signal for the same input RF power. Because the ratio of the fundamental signal power to nonlinear distortion (such as IMD3) is increased, the overall SFDR of the system is significantly improved.

Additionally, the Si RAMZM has a more complex transfer function, which results from the combination of the MZI's cosine characteristic and the RM's round-trip characteristic. This complexity facilitates the cancellation of high-order

distortion through various combinations of straight-through coefficient r and round-trip optical absorption coefficient a (See Appendix C).

This performance difference is evident in the fabricated devices described in the text. The sample MZM (which used an SPPMZM structure) was measured to achieve an SFDR of approximately 99.1 $dB \cdot Hz^{2/3}$ under its optimal bias conditions. This value represents the linearity performance of a conventional, albeit optimized, Si MZM.

In contrast, the RAMZM fabricated using the same process demonstrated significantly higher linearity. The RAMZM achieved an SFDR exceeding 105 $dB \cdot Hz^{6/7}$. Notably, this high performance was achieved even when operating in the high-frequency X-band (around 10 GHz) and using a differential modulation scheme.

However, the Si RAMZM has an important drawback: higher optical insertion loss compared to the Si MZM. While the Si RAMZM in this dissertation exhibits 10 dB of optical insertion loss for differential, high-linearity operation, only 5 dB of optical loss is required for the proper operation of the Si MZM. If an MWP system has a light source with limited maximum power, the Si MZM may be the preferred choice to achieve the desired performance. Therefore, the appropriate EO modulator must be selected according to the specific requirements of each MWP system.

4.2. Limitations of Si EO Modulators

Si EO modulators inherently exhibit poor linearity because the changes in effective refractive index n_{eff} and absorption coefficient a due to the plasma dispersion effect are nonlinear with respect to the applied voltage. Therefore, linearization methods by combining several structures, such as RAMZM and DPMZM, should be chosen for cancellation of the nonlinear characteristics. Furthermore, in Si MZMs, the attenuation of the RF signal caused by the TWE reduces the fundamental signal power, which adversely affects the SFDR. Although the RM within RAMZM is less affected by TWE due to its small size, electrical parameters—such as those from the metal layer and junction RC—still contribute to a decrease in fundamental signal power and an increase in IMD power. Achieving high linearity in a Si MZM requires careful TWE design to ensure efficient RF-to-optical signal transfer. Additionally, the doping profile must be configured so that the junction RC is less dependent on voltage, all while ensuring modulation efficiency is not sacrificed.

Si EO modulators also exhibit temperature dependence. For the Si MZM described above, as shown in Fig. 4-1, the optical transmission varies with the voltage applied to the thermo-optic heater at a constant wavelength. This change in transmission leads to a shift in the bias point due to the modulator's cosine characteristic (as seen in Fig. 2-21 of chapter 2.3.4). This shift, in turn, causes variations in the power of the fundamental signal and the IMD3 signal, as confirmed by simulations or measurements. Consequently, this results in a change in SFDR depending on the bias point (as shown in Fig. 2-26 of chapter 2.3.6). Furthermore, the effect of the TWE on the RF signal in Si MZM is also

temperature-dependent. Especially, the junction capacitance in the TWE increases due to higher temperature. This is because the higher temperature causes the higher intrinsic carrier concentration n_i in (2.4). The higher n_i makes lower built-in potential ϕ_i in PN junction, and that leads to smaller depletion region width and higher junction capacitance. Therefore, for accurate simulations across different temperatures, the TWE characteristics at various temperatures must be incorporated into the model. Similarly, in a Si RAMZM, the optical DC transmission of the RM changes with temperature, causing variations in SFDR analogous to those resulting from changes in the input wavelength (as seen in Fig. 3-31 of chapter 3.5.2.).

Therefore, to mitigate the temperature dependence in both Si MZM and the RM within RAMZM, a calibration algorithm and accompanying circuitry are necessary to find and maintain the optimal operating bias for modulation [116]-[118].

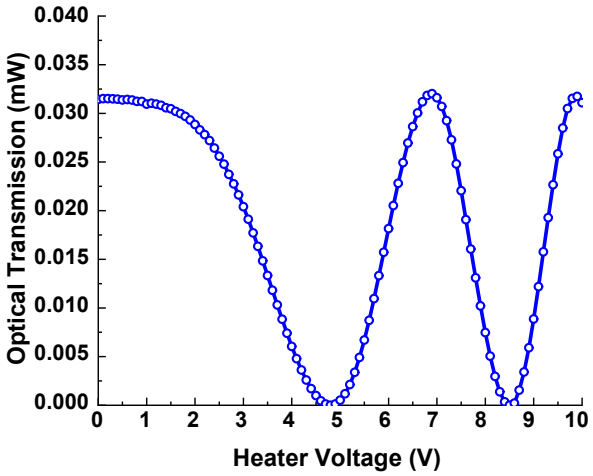

Fig. 4-1. The measured optical transmission of Si MZM with various heater voltages.

5. Conclusion

The linearity of an EO modulator is a key metric, as reducing IMD in the output signal directly improves the performance of MWP systems in terms of noise and effective number of bits. This dissertation analyzes the linearity of silicon-based EO modulators designed for MWP applications and demonstrates the fabrication and experimental verification of modulators with enhanced linearity. Because linearity plays such a critical role in overall system performance, establishing accurate methods for its analysis and developing modulators with improved linearity are of great importance. This work addresses these issues through both modeling and device implementation.

First, a characterization method was proposed to accurately evaluate the linearity of Si MZMs, and its validity was confirmed experimentally. The factors that influence the linearity of Si MZMs can be broadly categorized into three groups: the effects of the TWE, the PN junction phase shifter, and the junction capacitance. The TWE can be analyzed in terms of parameters such as characteristic impedance, microwave index, and optical group index, all of which affect frequency response. Using these factors, a linearity model was developed and experimentally verified. Furthermore, this model was employed to optimize linearity as a function of both the MZM bias point and the applied voltage.

Second, a Si RAMZM was designed, fabricated, and experimentally tested to demonstrate an EO modulator with both compact footprint and high linearity. Previous approaches achieving high linearity at high RF frequencies typically relied on large modulators such as DPMZMs, which incorporate two full MZMs.

In contrast, the RAMZM, which incorporates compact RMs, enables high linearity in a significantly smaller device. As a result, this work successfully implemented a RAMZM achieving an SFDR exceeding 105 $dB \cdot Hz^{6/7}$ at a 10-GHz RF signal, with a footprint of only ~1 mm^2—remarkably smaller than those reported in earlier studies.

In summary, this dissertation contributes to the study of EO modulators for MWP systems by addressing the critical metric of linearity. It presents both a validated model for optimizing Si MZM linearity and a compact RAMZM structure capable of delivering high linearity, offering pathways toward more efficient and scalable EO modulators.

Appendix A Euler's formula

The Euler's formulas are given by

$$e^{jx} = \cos x + j \cdot \sin x, \tag{A.1}$$

$$\cos x = \frac{e^{jx} + e^{-jx}}{2}, \tag{A.2}$$

$$\sin x = \frac{e^{jx} - e^{-jx}}{2j}. \tag{A.3}$$

The equations above can make (2.45) to (2.44) as follows:

$$r(\omega) = e^{\frac{-\alpha L}{2}} \cdot \left| \frac{\sin(\frac{-j\alpha L_{tw}}{2})}{\frac{-j\alpha L_{tw}}{2}} \right| = e^{\frac{-\alpha L}{2}} \cdot \frac{e^{\frac{\alpha L_{tw}}{2}} - e^{\frac{-\alpha L_{tw}}{2}}}{2j \frac{-j\alpha L_{tw}}{2}} = \frac{1 - e^{-\alpha L_{tw}}}{\alpha L_{tw}}. \tag{A.4}$$

Appendix B ABCD Matrix

The ABCD matrix is defined as a two-port network in terms of the total voltages and currents at the input and output ports, as illustrated in Fig. 2-16, and is given by the relation of (2.58).

When two two-port networks are connected in cascade, as shown in Fig. A-1, the overall ABCD matrix is obtained by multiplying the individual matrices as follows:

$$\begin{pmatrix} V_1 \\ I_1 \end{pmatrix} = \begin{pmatrix} A_1 & B_1 \\ C_1 & D_1 \end{pmatrix} \begin{pmatrix} A_2 & B_2 \\ C_2 & D_2 \end{pmatrix} \begin{pmatrix} V_3 \\ I_3 \end{pmatrix}. \tag{A.5}$$

It's important to maintain the same order of matrix multiplication as the physical arrangement of the networks, because matrix multiplication is generally not commutative.

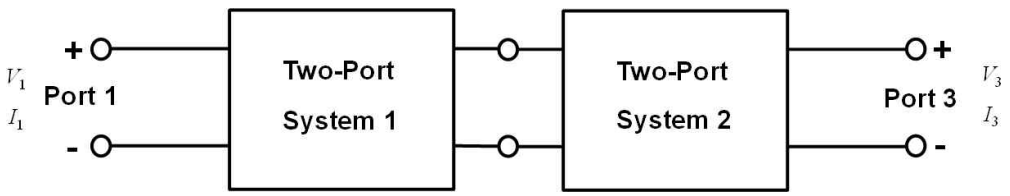

Fig. A-1. Diagram of cascaded two-port system.

Appendix C Numerical Linearity Analysis of Si RAMZM with Taylor Expansion

The linearity of a Si RAMZM is determined by the IMD component closest to the fundamental component when a microwave signal is applied. This is strongly influenced by the third- and seventh-order terms of the transfer function for the optical transmission, T_{out}, of the Si RAMZM. A common approach for mathematically analyzing this relationship is to express T_{out} as a polynomial equation using a Taylor expansion [80], [94]. In this dissertation, the Taylor expansion method is likewise employed for analysis.

For the case of a RAMZM incorporating two RMs, the analysis is conducted based on (3.8), where $E_{out.RM1}$ and $E_{out.RM2}$ can be expressed as follows.

$$E_{out.RM1} = A_1 \exp(j\theta_1),\ E_{out.RM2} = A_2 \exp(j\theta_2) \tag{A.6}$$

Here, A_1 and A_2 represent the amplitude responses of each RM, while θ_1 and θ_2 denote their respective phase responses. These parameters are assumed to be functions of the applied voltage. In addition, φ is set to 0 to achieve Q bias. Consequently, (A.8) becomes

$$E_{out} = \frac{1}{2} \cdot E_{in} \cdot [j \cdot A_1 \exp(j\theta_1) \cdot \exp(-j\varphi) + A_2 \exp(j\theta_2)] \ . \tag{A.7}$$

And then, optical transmission of the RAMZM can be expressed as

$$\left|\frac{E_{out}}{E_{in}}\right|^2 = \frac{A_1^2 + A_2^2 + 2A_1A_2\sin(\theta_1 - \theta_2)}{4}. \tag{A.8}$$

Assuming that $A_1 = A_2 = A$ and those have no variation with input voltage, (A.12) can be more simple equation, and that is

$$\left|\frac{E_{out}}{E_{in}}\right|^2 = \frac{2A^2 + 2A^2\sin(\theta_1 - \theta_2)}{4}. \tag{A.9}$$

Since θ_1 and θ_2 are functions of voltage v, they can be expressed as polynomial equations with respect to voltage. Furthermore, because the electrical signal is applied differentially to each RM, θ_1 and θ_2 at resonance wavelength can be represented as follows, if RMs are over-coupled.

$$\theta_1(v) = \pi + k_1v + k_2v^2 + k_3v^3 + k_4v^4 + \cdots \tag{A.10}$$

$$\theta_2(v) = \pi - k_1v + k_2v^2 - k_3v^3 + k_4v^4 - \cdots \tag{A.11}$$

θ is difference between θ_1 and θ_2, and that is

$$\theta(v) = \theta_1(v) - \theta_2(v) = 2k_1v + 2k_3v^3 + 2k_5v^5 + \cdots \tag{A.12}$$

As can be seen in (A.12), due to the differential operation, the even-order terms in the transfer function are eliminated. By substituting (A.12) into (A.9) and applying Taylor expansion to obtain $|E_{out}/E_{in}|^2$ as a function of voltage, only the odd-order terms remain, and the resulting expression is given as follows.

$$\left|\frac{E_{out}}{E_{in}}\right|^2 = \frac{2A^2 + 2A^2\sin(\theta(v))}{4} = \frac{A^2}{2} + \frac{A^2}{2}(c_1 v + c_3 v^3 + c_5 v^5 + c_7 v^7 + \cdots) \quad \text{(A.13)}$$

$$c_1 = 2k_1 \quad \text{(A.14)}$$

$$c_3 = 2k_3 - \frac{8k_1^3}{6} \quad \text{(A.15)}$$

$$c_5 = 2k_5 - 4k_1^2 k_3 + \frac{k_1^3}{15} \quad \text{(A.16)}$$

$$c_7 = 2k_7 - 4k_1^2 k_5 - 4k_1 k_3^2 + \frac{4k_1^4 k_3}{3} - \frac{8k_1^7}{315} \quad \text{(A.17)}$$

Here, reducing the absolute values of the coefficients for the third-, fifth-, or seventh-order terms can help minimize the IMD components. In particular, the conditions for eliminating the third- and fifth-order terms are as follows.

$$k_3 \approx \frac{2}{3}k_1^3 \quad \text{(A.18)}$$

$$k_5 \approx 2k_1^5 - \frac{k_1^3}{30} \quad \text{(A.19)}$$

Now, let us express the k_n values of θ in terms of the RM parameters a and r. The phase response of the Si RM is given by (3.3), and by applying the Maclaurin and Taylor expansions, it can be rewritten as a polynomial equation with respect to the round-trip phase shift ϕ inside the ring, as shown below.

$$\theta = \pi + s_1\phi + s_2\phi^2 + s_3\phi^3 + s_4\phi^4 + s_5\phi^5 + \cdots \tag{A.20}$$

$$s_1 = \frac{ar}{1-ar} + \frac{r}{a-r} + 1 \tag{A.21}$$

$$s_3 = -\frac{a^3r^3}{3(1-ar)^3} + \frac{a^2r^2}{2(1-ar)(ar-1)} - \frac{ar}{6(1-ar)} - \frac{r^3}{3(a-r)^3} - \frac{r^2}{2(a-r)^2} - \frac{r}{6(a-r)} \tag{A.22}$$

$$\begin{aligned} s_5 = {} & \frac{a^5r^5}{5(1-ar)^5} + \frac{a^4r^4}{2(1-ar)^3(ar-1)} + \frac{a^3r^3}{6(1-ar)^3} - \frac{a^2r^2}{12(1-ar)(ar-1)} \\ & + \frac{a^3r^3}{4(1-ar)(ar-1)^2} - \frac{a^2r^2}{24(1-ar)(ar-1)} + \frac{ar}{120(1-ar)} - \frac{r^5}{5(a-r)^5} \\ & + \frac{r^4}{2(a-r)^4} + \frac{r^3}{6(a-r)^3} + \frac{r^2}{12(a-r)^2} + \frac{r^3}{4(a-r)^3} + \frac{r^2}{24(a-r)^2} + \frac{r}{120(a-r)} \end{aligned} \tag{A.23}$$

$$s_2 = s_4 = 0 \tag{A.24}$$

If the input wavelength of Si RM is the resonance wavelength (ϕ_{DC} = 0), ϕ is given by

$$\phi(v) = b_1v + b_2v^2 + b_3v^3 + b_4v^4 + b_5v^5 + \cdots \tag{A.25}$$

Substituting (A.29) into (A.24), k_n are changed to

$$k_1 = s_1b_1 \tag{A.26}$$

$$k_2 = s_1b_2 \tag{A.27}$$

$$k_3 = s_1 b_3 + s_3 b_1^3 \tag{A.28}$$

$$k_4 = s_1 b_4 + 3 s_3 b_1^2 b_2 \tag{A.29}$$

$$k_5 = s_1 b_5 + s_3 (3 b_1^2 b_3 + 3 b_1 b_2^2) + s_5 b_1^5 \tag{A.30}$$

Since s_n is expressed as a function of a and r, it is possible to satisfy the linearity improvement conditions (A.18) and (A.19) for specific values of a and r. However, because ϕ is also a function of voltage, the coefficients b_n within ϕ result in many combinations of a and r that satisfy these conditions, making it easier to achieve a more linear output optical signal.

Bibliography

[1] “Global Cellular IoT Connections 2019-2030,” IoT Analytics, https://iot-analytics.com/global-cellular-iot-connections/ (accessed Aug. 29, 2025)

[2] E. A. Kadir, R. Shubair, S. K. Abdul Rahim, M. Himdi, M. R. Kamarudin and S. L. Rosa, "B5G and 6G: Next Generation Wireless communications technologies, demand and challenges," 2021 *International Congress of Advanced Technology and Engineering* (ICOTEN), Taiz, Yemen, 2021. pp. 1-6.

[3] H. Yu *et al*., “800 Gbps fully integrated silicon phootnics transmitter for data center applications,” in proceedings of SPIE Photonics West, San Francisco, CA, USA, 2022, paper M2D.7.

[4] D. Zhang *et al*., “Technological prospection and requirements of 800G transmission systems for ultra-long-haul all-optical terrestrial backbone networks,” *Journal of Lightwave Technology*, vol. 41, no.12, pp. 3774-3782, Jun. 2023.

[5] F. Ferraro *et al*., “IMEC silicon photonics platforms performance overview and roadmap,” in proceedings of *SPIE Photonics West*, San Francisco, CA, USA, 2023, paper 1242909.

[6] P. Dong, Y.-K. Chen, G.-H. Duan, and D. T. Neilson, “Silicon photonic devices and integrated circuits,” *Nanophotonics*, vol. 3, no. 4-5, pp. 215-228, Aug. 2014.

[7] R. Nagarajan *et al*., “Inp photonic integrated circuits,” *IEEE Journal of Selected Topics in Quantum Electronics*, vol. 16, no. 5, pp. 1113-1125, Sep.-Oct. 2010.

[8] J. Klamkin et al., “Indium phosphoide photonic integrated circuits:

Technology and applications," in proceedings of *IEEE BiCMOS and Compound Semiconductor Integrated Circuit and Technology Symposium (BCICTS)*, San Diego, CA, USA, pp. 8-13, 2018.

[9] C. P. Dietrich, A. Fiore, M. G. Thompson, M. Kamp, and S. Hölfling, "GaAs integrated quantum photonics: Towards compact and multi-functional quantum photonic integrated circuits," *Laser & Photonics Reviews*, vol. 10, no. 6, pp. 870-894, Sep. 2016.

[10] P. Jiang and K. C. Balram, "Suspened gallium arsenide platform for building large scale photonic integrated circuits: Passive devices," *Optics Express*, vol. 28, no. 8, pp. 12262-12271, Apr. 2020.

[11] A. Boes, B. Corcoran, L. Chang, J. Bowers, and A. Mitchell, "Status and potential of lithium niobated on insulatros (LNOI) for pohotonic integrated circuits," *Laser & Photonics Reviews*, vol. 12, no. 4, Feb. 2018.

[12] Z. Li *et al*., "High density lithium niobate photonic integrated circuits," *Nature Communications*, vol. 14, Aug. 2023.

[13] R. Soref, "The past, present, and future of silicon photonics," *IEEE Journal of Selected Topics in Quantum Electronics*, vol. 12, no. 6, pp. 1678-1687, Nov.-Dec. 2006.

[14] B. Jalali and S. Fathpour, "Silicon photonics," *Journal of Lightwave Technology*, vol. 24, no. 12, pp. 4600-4615, Dec. 2006.

[15] R. Won, "Integrating silicon photonics," *Nature Photonics*, vol. 4, pp. 498-499, Aug. 2010.

[16] F. Horst, W. M.J. Green, S. Assefa, S. M. Shank, Y. A. Vlasov, and B. J. Offrein, "Cascaded Mach-Zehnder wavelength filters in silicon photonics for low loss and flat pass-band WDM (de-)multiplexing," *Optics Express*, vol. 21, no. 10, pp. 11652-11658, May 2013.

[17] P. Dong, "Silicon photonic integrated circuits for wavelength-division

multiplexing applications," *IEEE Journal of Selected Topics in Quantum Electronics*, vol. 22, no. 6, pp. 370-378, Nov.-Dec. 2016.

[18] M. Huang *et al*., "Germanium on silicon avalanche photodiode," *IEEE Journal of Selected Topics in Quantum Electronics*, vol. 24, no. 2, Art no. 3800911, Mar.-Apr. 2018.

[19] S. Lischke *et al*., "Ultra-fast germanium photodiode with 3-dB bandwidth of 265 GHz," *Nature Photonics*, vol. 15, pp. 925-931, Dec. 2021.

[20] L. Liao, D. Samara-Rubio, M. Morse, A. Liu, and D. Hodge, "High speed silicon Mach-Zehnder modulator," *Optics Express*, vol. 13, no. 8, pp. 3129-3135, Apr. 2005.

[21] P. Dong *et al*., "Low Vpp, ultralow-energy, compact, high-speed silicon electro-optic modulator," *Optics Express*, vol. 17, no. 25, pp. 22484-22490, Dec. 2009.

[22] M. Arrazola, "Quantum circuits with many photons on a programmable nanophotonic chip," *Nature*, vol. 591, pp. 54 60, Mar. 2021.

[23] W. Bogaerts *et al*., "Programmable photonic circuits," *Nature*, vol. 586, pp. 207-216, Oct. 2020.

[24] Y. Zhou, L. Wang, Y. Liu, Y. Yu, and X. Zhang, “Microwave Photonic Filters and Applications,” *MDPI Photonics*, no. 10, 2023.

[25] P. Dong, Y.-K. Chen, G.-H. Duan, and D. T. Neilson, “Silicon photonic devices and integrated circuits,” *Nanophotonics*, vol. 3, no. 4-5, pp. 215-228, Aug. 2014.

[26] J. Capmany and D. Novak, “Microwave photonics combines two worlds,” *Nature photonics*, vol. 1, no. 6, p. 319, 2007.

[27] W. J. Chappell, E. J. Naglich, C. Maxey, and A. C. Guyette, “Putting the radio in “software-defined radio”: Hardware developments for adaptable rf systems,” *Proceedings of the IEEE*, vol. 102, no. 3, pp. 307 –320, 2014.

[28] I. F. Akyildiz, A. Kak, and S. Nie, “6g and beyond: The future of wireless communications systems,” *IEEE Access*, vol. 8, pp. 133 995–134 030, 2020.

[29] V. Urick, M. J.D., andW. K. J., Fundamentals of Microwave Photonics (Wiley series in microwave and optical engineering). *John Wiley & Sons Inc.*, 2014.

[30] J. Yao, “Microwave photonics,” *Journal of lightwave technology*, vol. 27, no. 3, pp. 314–335, 2009.

[31] D. Marpaung, C. Roeloffzen, R. Heideman, A. Leinse, S. Sales, and J. Capmany, “Integrated microwave photonics,” *Laser & Photonics Reviews*, vol. 7, no. 4, pp. 506–538, 2013.

[32] D. Marpaung, J. Yao, and J. Capmany, “Integrated microwave photonics,” *Nature photonics*, vol. 13, no. 2, pp. 80–90, 2019.

[33] K.Williams, R. Esman, and M. Dagenais, “Nonlinearities in p-i-n microwave photodetectors,” *Journal of Lightwave Technology*, vol. 14, pp. 84–96, 1996.

[34] A. Hilt, G. J´ar´o, A. Z´olomy, B. Cabon, T. Berceli, and T. Marozs´ak, “Microwave characterization of high-speed pin photodiodes,” in Proceeding in *9th Conference on Microwave Techniques COMITE’1997*, Oct. 1997, pp. 21–24.

[35] D. Decoster, J.-P. Vilcot, J. Harari, and V. Magnin, “Photodetectors for microwave applications: A review and trends,” in *Proceedings of SPIE*, 2003, pp. 1–5.

[36] O. Daulay, “High performance programmable integrated microwave photonic filters,” *Ph.D dissertation*, University of Twente, 2022.

[37] J. Capmany, J. Mora, I. Gasulla, J. Sancho, J. Lloret, and S. Sales, “Microwave photonic signal processing,” *Journal of Lightwave Technology*, vol. 31, no. 4, pp. 571–586, 2012.

[38] J. Capmany, B. Ortega, and D. Pastor, “A tutorial on microwave photonic filters,” *Journal of Lightwave technology*, vol. 24, no. 1, pp. 201–229, 2006.

[39] D. Marpaung, B. Morrison, R. Pant, et al., “Si 3 n 4 ring resonator-based microwave photonic notch filter with an ultrahigh peak rejection,” *Optics Express*, vol. 21, no. 20, pp. 23 286–23 294, 2013.

[40] S. Shahnia, M. Pagani, B. Morrison, B. J. Eggleton, and D. Marpaung, “Independent manipulation of the phase and amplitude of optical sidebands in a highly-stable rf photonic filter,” *Optics Express*, vol. 23, no. 18, pp. 23 278-286, 2015.

[41] J. S. Fandi˜no, P. Mu˜noz, D. Dom´enech, and J. Capmany, “A monolithic integrated photonic microwave filter,” *Nature Photonics*, vol. 11, no. 2, pp. 124–129, 2017.

[42] L. Zhuang, D. Marpaung, M. Burla, W. Beeker, A. Leinse, and C. Roeloffzen, “Low-loss, high-index-contrast si 3 n 4/sio 2 optical waveguides for optical delay lines in microwave photonics signal processing,” *Optics Express*, vol. 19, no. 23, pp. 23 162-170, 2011.

[43] Y. Liu, A. Choudhary, D. Marpaung, and B. J. Eggleton, “Gigahertz optical tuning of an on-chip radio frequency photonic delay line,” *Optica*, vol. 4, no. 4, pp. 418–423, 2017.

[44] X. Ji, X. Yao, Y. Gan, et al., “On-chip tunable photonic delay line,” *APL Photonics*, vol. 4, no. 9, p. 090 803, 2019.

[45] C. Tsokos, E. Andrianopoulos, A. Raptakis, et al., “True time delay optical beamforming network based on hybrid inp-silicon nitride integration,” *Journal of Lightwave Technology*, vol. 39, no. 18, pp. 5845 –5854, 2021.

[46] M. H. Khan, H. Shen, Y. Xuan, et al., “Ultrabroad-bandwidth arbitrary radio frequency waveform generation with a silicon photonic chip-based

spectral shaper," *Nature Photonics*, vol. 4, no. 2, pp. 117–122, 2010.

[47] A. M. Weiner, "Ultrafast optical pulse shaping: A tutorial review," *Optics Communications*, vol. 284, no. 15, pp. 3669–3692, 2011.

[48] D. Marpaung, L. Chevalier, M. Burla, and C. Roeloffzen, "Impulse radio ultrawideband pulse shaper based on a programmable photonic chip frequency discriminator," *Optics Express*, vol. 19, no. 25, pp. 24 838–24 848, 2011.

[49] J. Wang, H. Shen, L. Fan *et al*., "Reconfigurable radio-frequency arbitrary waveforms synthesized in a silicon photonic chip," *Nature Communications*, vol. 6, no. 1, pp. 1–8, 2015.

[50] W. Li, N. H. Zhu, L. X. Wang, and H. Wang, "Broadband phase-to-intensity modulation conversion for microwave photonics processing using brillouinassisted carrier phase shift," *Journal of Lightwave technology*, vol. 29, no. 24, pp. 3616–3621, 2011.

[51] M. Burla, L. R. Cortes, M. Li, X. Wang, L. Chrostowski, and J. Azana, "Onchip programmable ultra-wideband microwave photonic phase shifter and true time delay unit," *Optics Letters*, vol. 39, no. 21, pp. 6181–6184, 2014.

[52] C. Porzi, G. Serafino, M. Sans *et al*., "Photonic integrated microwave phase shifter up to the mm-wave band with fast response time in silicon-on-insulator technology," *Journal of Lightwave Technology*, vol. 36, no. 19, pp. 4494–4500, 2018.

[53] S. X. Chew, D. Huang, L. Li *et al*., "Integrated microwave photonic phase shifter with full tunable phase shifting range (> 360°) and rf power equalization," *Optics Express*, vol. 27, no. 10, pp. 14 798–14 808, 2019.

[54] C Wang *et al*., "Modeling and analysis of crosstalk for time-interleaved photonic ADCs," *Journal of Lightwave Technology*, vol. 38, no. 15, pp.

3926-3934, 2020.

[55] A. Khilo *et al*., "Photonic ADC: overcoming the bottleneck of electronic jitter," *Optics Express*, vol. 20, no. 4, pp. 4454-4469, 2012.

[56] "How to Calculated ENOB for ADC Dynamic Performance Measurement," Analog Devices, https://www.analog.com/en/resources/technical-articles/how-to-calculate-enob-for-adc-dynamic-performance-measurement.html (accessed Oct. 27, 2025)

[57] X. Yi, T. X. Huang, and R. A. Minasian, "Photonic beamforming based on programmable phase shifters with amplitude and phase control," *IEEE Photonics Technology Letters*, vol. 23, no. 18, pp. 1286–1288, 2011.

[58] L. Zhuang, M. Hoekman, C. Taddei, et al., "On-chip microwave photonic beamformer circuits operating with phase modulation and direct detection," *Optics Express*, vol. 22, no. 14, pp. 17 079–17 091, 2014.

[59] S. A. Miller, Y.-C. Chang, C. T. Phare, et al., "Large-scale optical phased array using a low-power multi-pass silicon photonic platform," *Optica*, vol. 7, no. 1, pp. 3–6, 2020.

[60] C. Zhu, L. Lu,W. Shan, et al., "Silicon integrated microwave photonic beamformer," *Optica*, vol. 7, no. 9, pp. 1162–1170, 2020.

[61] Y. Jo *et al*., "Modulation linearity characterization of Si ring modulators," *Journal of Lightwave Technology*, vol. 39, no. 24, pp.7842-7849, Dec. 2021.

[62] M.-H. Seong *et al*., "Modulation linearity characterization of Si Mach-Zehnder modulators," *Journal of Lightwave Technology*, vol. 42, no. 6, pp.1901-1909, Mar. 2024.

[63] J. Okyere, K. Yu, K. Entesari, and S. Palermo, :A fifth-order polynomial predistortion circuit for mach-zehnder modulator linearization in 65nm cmos," in Proceedings of *2017 Texas Symposium on Wireless and Microwave Circuits and Systems (WMCS), IEEE*, 2017, pp. 1–4.

[64] N. Hosseinzadeh, A. Jain, R. Helkey, and J. F. Buckwalter, “A distributed low-noise amplifier for broadband linearization of a silicon photonic mach−zehnder modulator,” *IEEE Journal of Solid-State Circuits*, vol. 56, pp. 1897−1909, 2020.

[65] M. Yang et al., "Non-blocking 4x4 electro-optic silicon switch for on-chip photonic networks," *Optics Express*, vol. 19, no. 1, p. 47, Jan. 2011.

[66] K. Suzuki et al., "Ultra-compact 8 x 8 strictly-non-blocking Si-wire PILOSS switch," *Optics Express*, vol. 22, no. 4, p. 3887, Feb. 2014.

[67] L. Qiao, W. Tang, and T. Chu, "32 x 32 silicon electro-optic switch with built-in monitors and balanced-status units," *Science Reports*, vol. 7, no. 1, p. 42306, Sep. 2017.

[68] D. Janner, D. Tulli, M. García-Granda, M. Belmonte, and V. Pruneri, "Micro-structured integrated electro-optic LiNbO3 modulators," *Laser & Photonics Review*, vol. 3, no. 3, pp. 301-313, Apr. 2009.

[69] M. Nedeljkovic, R. Soref, and Goran Z. Mashanovich, "Free-carrier electrorefraction and electroabsorption modulation predictions for silicon over the 1-14-Mm infrared wavelength range." *IEEE Photonics Journal*, vol. 3 no. 6, pp. 1171-80, 2011.

[70] S. M. Sze, “Semiconductor devices”, *Wiley*, New York, 1985.

[71] H. Chen, “Development of an 80 Gbit/s InP-based Mach-Zehnder Modulator,” *M.S. Dissertation*, Universität Berlin, Germany, 2022.

[72] Q. Xu, B. Schmidt, S. Pradhan, and M. Lipson, "Micrometre-scale silicon electro-optic modulator," *Nature*, vol. 435, no. 7040, pp. 325-327, May 2005.

[73] S. S. Azadeh et al., "Low V_π Silicon photonics modulators with highly linear epitaxially grown phase shifters," *Optics Express*, vol. 23, no. 18, p. 23526, Sep. 2015.

[74] F. Y. Gardes, D. J. Thomson, N. G. Emerson, and G. T. Reed, “40 Gb/s silicon photonics modulator for TE and TM polarisations,” *Optics Express*, vol. 19, no. 12, pp. 11804–11814, 2011.

[75] R. G. Walker: “High-Speed III-V Semiconductor Intensity Modulators,” *IEEE Journal of Quantum Electronics*, vol. 27, pp. 654-667, 1991.

[76] S. H. Lin and S. Y. Wang, “High throughput GaAs p-i-n electrooptic modulator with a 3dB bandwidth of 9.6 GHz at 1.3 μm,” *Applied Optics*, vol. 26, 1696-1700, 1987.

[77] S. Y. Wang and S. H. Lin, “High speed III-V electrooptic waveguide modulators at λ=1.3 μm,” *IEEE Journal of Lightwave Technology*, vol. 6, pp. 758-771, 1988.

[78] H. Xu, X. Li, X. Xiao, Z. Li, Y. Yu, and J. Yu, “Demonstration and characterization of high-speed silicon depletion-mode Mach–Zehnder modulators,” *IEEE Journal of Selected Topics in Quantum Electronics*, vol. 20, no. 4, Jul.-Aug. 2014, Art. no. 3400110.

[79] E. Voges and K. Petermann, “Optische kommunikationstechnik”, Springer, Berlin, 2002.

[80] Q. Zhang et al., “Linearity comparison of silicon carrier-depletion-based single, dual-parallel, and dual-series Mach–Zehnder modulators,” *Journal of Lightwave Technology*, vol. 36, no. 16, pp. 3318–3331, Aug. 2018, doi: 10.1109/JLT.2018.2839603.

[81] Yanyang Zhou, Linjie Zhou, Feiran Su, Xinwan Li, and Jianping Chen, "Linearity measurement and pulse amplitude modulation in a silicon single-drive push–pull Mach–Zehnder modulator," *Journal of Lightwave Technology*, vol. 34, 3323-3329, 2016.

[82] Matthew Streshinsky, Ali Ayazi, Zhe Xuan, Andy Eu-Jin Lim, Guo-Qiang Lo, Tom Baehr-Jones, and Michael Hochberg, "Highly linear silicon traveling wave Mach-Zehnder carrier depletion modulator based

on differential drive," *Optics Express*, vol. 21, 3818-3825, Feb. 2013.

[83] Y. Zhou et al., "Linearity characterization of a dual−parallel silicon Mach −Zehnder modulator," *IEEE Photonics Journal*, vol. 8, no. 6, pp. 1-8, Dec. 2016, Art no. 7805108, doi: 10.1109/JPHOT.2016.2616488.

[84] Jianfeng Ding, Sizhu Shao, Lei Zhang, Xin Fu, and Lin Yang, "Method to improve the linearity of the silicon Mach-Zehnder optical modulator by doping control," *Optics Express*, vol. 24, 24641-24648, 2016.

[85] A. M. Gutierrez et al., "Analytical model for calculating the nonlinear distortion in silicon-based electro-optic Mach−Zehnder modulators," *Journal of Lightwave Technology*, vol. 31, no. 23, pp. 3603-3613, Dec. 2013, doi: 10.1109/JLT.2013.2286838.

[86] C. G. Bottenfield, V. A. Thomas and S. E. Ralph, "Silicon photonic modulator linearity and optimization for microwave photonic links," *IEEE Journal of Selected Topics in Quantum Electronics*, vol. 25, no. 5, pp. 1-10, Sept.-Oct. 2019, Art no. 3400110, doi: 10.1109/JSTQE.2019.2908784.

[87] A. Samani, M. Chagnon, M. Morsy-Osman, M. Poulin, C. Paquet, S. Lessard, and D. V. Plant, “Experimental parametric study of a silicon photonic modulator enabled 112-Gb/s PAM transmission system with a DAC and ADC,” *Journal of Lightwave Technology*, vol. 33, 1380−1387, 2015.

[88] D. Frickey, “Conversions between S, Z, Y, H, ABCD, and T parameters which are valid for complex source and load impedances,” *IEEE Transaction on Microwave Theory and Technology*, vol. 42, 205−211, Feb. 1994.

[89] David Patel, Samir Ghosh, Mathieu Chagnon, Alireza Samani, Venkat Veerasubramanian, Mohamed Osman, and David V. Plant, "Design, analysis, and transmission system performance of a 41 GHz silicon

photonic modulator," Opt. Exp., vol. 23, 14263-14287, Jun. 2015.

[90] W. B. Bridges and J. H. Schaffner, “Distortion in linearized electrooptic modulators,” *IEEE Transaction on Microwave Theory and Technology*, vol. 43, no. 9, pp. 2184–2197, Sep. 1995.

[91] Singh, Sarika, Sandeep K. Arya, and Shelly Singla. "Linearization of photonic link based on phase-controlled dual drive dual-parallel Mach–Zehnder modulator," *Wireless Personal Communications*, vol.114, no.1, pp. 85-92, 2020.

[92] Q. Zhang, Q. Huang, P. Xia, Y. Li, X. Jiang, S. Zhang, S.Fang, J. Yang, and H.. Yu, “All-Optically Linearized Silicon Modulator with Ultrahigh SFDR of 131 dB.Hz$^{6/7}$,” *Photonics Research*, vol. 13, no. 2, pp. 433–441, 2025.

[93] J. Cardenas, P. A. Morton, J. B. Khurgin, A. Griffith, C. B. Poitras, K. Preston, and M. Lipson, “Linearized silicon modulator based on a ring assisted mach zehnder inteferometer,” *Optics Express*, vol. 21, pp. 22549 –22557, 2013.

[94] M. J. Shawon and V. Saexena, “Optical Linearization of Silicon Photonic Ring-Assisted Mach-Zehnder Modulator,” *Journal of Lightwave Technology*, vol. 42, no. 8, pp 2868-2879, 2023.

[95] W. Bogaerts et al., "Silicon microring resonators," *Laser & Photonics Reviews*, vol. 6, no. 1, pp. 47-73, Sep. 2012.

[96] K. De Vos et al., "Multiplexed Antibody Detection With an Array of Silicon-on-Insulator Microring Resonators," *IEEE Photonics Journal*, vol. 1, no. 4, pp. 225-235, Oct. 2009.

[97] D.-X. Xu et al., "Label-free biosensor array based on silicon-on-insulator ring resonators addressed using a WDM approach," *Optics Letter*, vol. 35, no. 16, pp. 2771, Aug. 2010.

[98] A. L. Washburn, L. C. Gunn, and R. C. Bailey, "Label-Free Quantitation

of a Cancer Biomarker in Complex Media Using Silicon Photonic Microring Resonators," *Analytical Chemisty Journal*, vol. 81, no. 22, pp. 9499-9506, Nov. 2009.

[99] S. M. Lo, S. Hu, G. Gaur, Y. Kostoulas, S. M. Weiss, and P. M. Fauchet, "Photonic crystal microring resonator for label-free biosensing," *Optics Express*, vol. 25, no. 6, p. 7046, Mar. 2017.

[100] B. G. Lee, B. A. Small, K. Bergman, Q. Xu, and M. Lipson, "Transmission of high-data-rate optical signals through a micrometer-scale silicon ring resonator," *Optics Letter*, vol. 31, no. 18, p. 2701, Sep. 2006.

[101] M. A. Popovíc et al., "Multistage high-order microring-resonator add-drop filters," *Optics Letter*, vol. 31, no. 17, p. 2571, Sep. 2006.

[102] T. Barwicz et al., "Silicon photonics for compact, energy-efficient interconnects [Invited]," *Journal of Optical Communications and Networking*, vol. 6, no. 1, p. 63, 2007.

[103] M. A. Seyedi, R. Wu, C. Chen, M. Fiorentino, and R. G. Beausoleil, "15 Gb/s Transmission with Wide-FSR Carrier Injection Ring Modulator for Tb/s Optical Links," in Proceedings of *Conference on Lasers and Electro-Optics*, 2016, p. SF2F.7.

[104] R. Wu, C.-H. Chen, T.-C. Huang, K.-T. Cheng, and R. Beausoleil, "20 Gb/s carrier-injection silicon microring modulator with SPICE-compatible dynamic model," in Proceeding of *2015 International Conference on Photonics in Switching (PS)*, 2015, pp. 31-33.

[105] Y. Ban et al., "Low-Voltage 60Gb/s NRZ and 100Gb/s PAM4 O-Band Silicon Ring Modulator," in Proceeding of *2019 IEEE Optical Interconnects Conference (OI)*, 2019, pp. 1-2.

[106] S. Pitris et al., "O-Band Silicon Photonic Transmitters for Datacom and Computercom Interconnects," *Journal of Lightwave Technology*, vol. 37,

no. 19, pp. 5140-5148, Oct. 2019.

[107] S. Pitris et al., "A 400 Gb/s O-band WDM (8x50 Gb/s) Silicon Photonic Ring Modulator-based Transceiver," in Proceedings of *Optical Fiber Communication Conference (OFC) 2020*, 2020, p. M4H.3.

[108] S. Chen, G. Zhou, L. Zhou, L. Lu, and J. Chen, " High-Linearity Fano Resonance Modulator Using a Microring-Assisted Mach-Zehnder Structure," *Journal of Lightwave Technology*, vol. 38, no. 13, pp 3395-3403, 2020.

[109] J. Rhim *et al.*, "Verilog-A behavioral model for resonance-modulated silicon micro-ring modulator." *Optics Express*, vol. 23, no. 7, pp. 8762-8772, 2015.

[110] R. Dubé-Demers *et al*., "Analytical Modeling of Silicon Microring and Microdisk Modulators With Electrical and Optical Dynamics," *Journal of Lightwave Technology*, vol. 33, no. 20, pp. 4240-4252, 15 Oct., 2015.

[111] M. Shin *et al*., "A Linear Equivalent Circuit Model for Depletion-Type Silicon Microring Modulators," *IEEE Transactions on Electron Devices*, vol. 64, no. 3, pp. 1140-1145, 2017.

[112] A. Jain, X. Wu, J. E. Bowers, R. Helkey and J. Buckwalter, "Linear Ring Modulators with DC Kerr Phase Shifters," in Proceedings in *2018 IEEE Avionics and Vehicle Fiber-Optics and Photonics Conference (AVFOP)*, Portland, OR, USA, 2018, pp. 1-2.

[113] Q. Zhang et al., "Improving the Linearity of Silicon Ring Modulators by Manipulating the Photon Dynamics," *IEEE Photonics Journal*, vol. 12, no. 2, pp. 1-10, April 2020, Art no. 6600810,

[114] M. Streshinsky et al., "Highly Linear Silicon Traveling-Wave Mach–Zehnder Carrier Depletion Modulator based on Differential Drive," *Optics Express*, vol. 21, no. 3, pp. 3818–3825, 2013.

[115] Y. Zhou, L. Zhou, M. Wang, Y. Xia, Y. Zhong, and X. Li, “Linearity Characterization of a Dual–Parallel Silicon Mach–Zehnder Modulator,” *IEEE Photonics Journal*, vol. 8, no. 6, Dec. 2016, Art. no. 7805108.

[116] J. -K. Park, M. -H. Seong, K. Kim, J. -H. Lee and W. -Y. Choi, "A Quadrature Biasing Method Based on Slope Detection for Si Mach-Zehnder Modulators," *IEEE Photonics Journal*, vol. 17, no. 4, pp. 1-5, Aug. 2025, Art no. 6601305.

[117] H. -K. Kim, K. Kim, M. -H. Seong, Y. Ji and W. -Y. Choi, "A Bias Controller for Si Mach-Zehnder Modulator," *IEEE Photonics Technology Letters*, vol. 35, no. 19, pp. 1027-1030, 1 Oct.1, 2023.

[118] Min-Hyeong Kim, Lars Zimmermann, and Woo-Young Choi, "A Temperature Controller IC for Maximizing Si Micro-Ring Modulator Optical Modulation Amplitude," *Journal of Lightwave Technology*, vol. 37, pp. 1200-1206, 2019.

Abstract in Korean

마이크로파 포토닉스를 위한 실리콘 기반 전자-광 변조기의 변조 선형성

이 논문은 차세대 마이크로파 포토닉스(MWP) 시스템을 위한 고선형 실리콘(Si) 전자-광(EO) 변조기의 모델링, 설계 및 특성화를 다룬다. 디지털 전자 기술의 한계에 직면하여, MWP는 넓은 주파수 대역폭, 낮은 전송 손실, 그리고 전자기 간섭에 대한 면역성과 같은 강점을 통해 미래 통신 기술의 요구 사항을 충족하는 유망한 해결책으로 부상했다. 이 시스템의 핵심 부품인 실리콘 기반 전자-광 변조기는 높은 집적도와 낮은 제조 비용의 이점을 제공하지만, PN 접합 효과로 인해 본질적인 비선형성을 겪는다. 이 비선형성은 전체 시스템 성능을 저하시키며, 특히 3차 상호변조 왜곡(IMD3)과 무혼변조 동적 범위(SFDR)가 중요한 성능 지표로 사용된다.

전자적 전치 왜곡(pre-distortion)과 같은 외부 보상 기술이 문제를 완화하기 위해 제안되었지만, 높은 전력 소모와 협대역 특성으로 인해 광대역 광자 시스템에는 적합하지 않은 경우가 많다. 따라서 본질적으로 높은 선형성을 갖는 전자-광 변조기를 개발하는 것이 매우 중요하다. 이 논문은 변조기 선형성을 정확하게 예측하고 최적화할 수 있는 정밀한 시뮬레이션 모델을 구축하는 것의 중요성을 강조한다. 본 연구는 실리콘 전자-광 변조기의 선형성을 향상시키기 위한 모델링 및 설계 접근 방식을 제시하며, 제안된 방법론의 효과를 입증한다.

본 연구는 먼저 실리콘 진행파 전극 마크젠더 변조기(Si TWE MZM)를 위한 새롭고 정확한 시뮬레이션 모델을 소개한다. 이 모델은 전압 의존적 유효 굴절률 및 접합 커패시턴스와 같은 핵심 매개변수를 통합하여 전기-광학 위상 변위기와 TWE의 비선형성을 모두 고려한다. 모델 매개변수는 측정과 시뮬레이션의 조합을 통해 추출되었으며, 전자-광 주파수 응답 및 IMD3에 대한 시뮬레이션 결과와 실험 결과를 비교하여 정확성을 검증했다. 우리의 분석은 유효 굴절률과 접합 커패시턴스의 비선형적 변화가 IMD3의 주요 원인임을 밝혀냈으며, 이들의 상대적 중요성은 DC 바이어스 전압에 따라 달라진다. relative

intensity 잡음, shot 잡음 및 열 잡음으로부터 잡음 플로어를 정확하게 추정함으로써, 우리 모델은 장치의 SFDR을 효과적으로 예측하여 고성능 Si MZM의 설계 및 최적화를 위한 귀중한 도구를 제공한다.

또한, 우리는 MWP application을 위해 설계된 새로운 고선형 실리콘 링 보조 마크젠더 변조기(RAMZM)를 제안한다. 이 장치는 차동 변조 방식을 사용하며, 두 개의 공핍형 실리콘 링 변조기를 마크젠더 간섭계에 통합한다. 최적의 성능을 보장하기 위해, 이 장치는 광학 바이어싱을 위한 열적 튜닝 기능을 포함한다. Two-tone 측정을 통해 제안된 RAMZM은 약 1 mm^2의 작은 크기를 유지하면서 10 GHz에서 105.4 $dB \cdot Hz^{6/7}$의 탁월하게 높은 SFDR을 시연했다. 특히, 측정 결과는 7차 상호변조 왜곡이 우세하게 나타나 기존 실리콘 변조기에 비해 선형성이 크게 개선되었음을 보여준다. 이 고성능의 소형 RAMZM은 광대역 및 고충실도 차세대 통신 시스템을 위한 유망한 후보이다.

핵심되는 말: 실리콘 포토닉스, 마이크로파 포토닉스, 전자-광 변조기, 변조 선형성, 상호변조 왜곡, 무혼변조 동적 범위, 마크젠더 변조기, 진행파 전극, 링 보조 마크젠더 변조기

List of Publications

International Journal Papers

**equally contributed*

[1] **Min-Hyeok Seong**, Yongjin Ji, Chulsoon Im, Youngseok Bae, and Woo-Young Choi, “Modulation linearity characterization of Si Mach-Zehnder modulators,” Journal of Lightwave Technology, vol. 42, no. 6, pp. 1901–1909, Mar. 2024.

[2] Jae-Koo Park*, **Min-Hyeok Seong***, Kihun Kim, Jae-Ho Lee and Woo-Young Choi, "A Quadrature Biasing Method Based on Slope Detection for Si Mach-Zehnder Modulators," IEEE Photonics Journal, vol. 17, no. 4, pp. 1-5, Aug. 2025.

[3] Hyun-Kyu Kim*, Kihun Kim*, **Min-Hyeok Seong**, Yongjin Ji and Woo-Young Choi, "A Bias Controller for Si Mach-Zehnder Modulator," IEEE Photonics Technology Letters, vol. 35, no. 19, pp. 1027-1030, 1 Oct.1, 2023

International Conference Presentations

[1] **Min-Hyeok Seong**, Yongjin Ji, Chul-Soon Im, Youngseok Bae, and Woo-Young Choi, “A simple but accurate linearity model for Si Mach-Zehnder modulators,” in Proceedings of SPIE Photonics West 2024, Terahertz, RF, Millimeter, and Submillimeter-Wave Technology and Applications XVII, 27 Jan. - 1 Feb., 2024.

[2] **Min-Hyeok Seong**, Yongjin Ji, and Woo-Young Choi, “A highly linear and compact Si ring-assisted mach-zehnder modulator at X band,” in Proceedings of International Topical Meeting on Microwave Photonics 2025 (MWP 2025), 14-17 Oct., 2025.

[3] (Invited) Woo-Young Choi, **Min-Hyeok Seong**, and Yongjin Ji, “Modulation linearity of Si mach-zehnder modulators,” accepted for 2025 Asia-Pacific Microwave Conference (APMC 2025).

[4] Hyun-Kyu Kim, Yongjin Ji, **Min-Hyeok Seong**, Kihun Kim, and Woo-Young Choi “Automated calibration of MZI-based Si optical switch matrix,” in Proceedings of SPIE Photonics West 2023, Smart Photonic and Optoelectronic Integrated Circuits, 28 Jan. - 2 Feb., 2023.

Domestic Journal Papers

[1] **성민혁**, 조영관, 김민규, 박강엽, 오원석, 최우영, “25-Gbps Depletion-Type 실리콘 링 변조기 성능 극대화를 위한 소자 구조 최적화,” 전자공학회논문지, vol. 58, no. 1, pp. 21-29, 2021.

[2] Tae-Young Choi, Jae-Ho Lee, Donghyeon Kim, **Min-Hyeok Seong**, and Woo-Young Choi, “An Inductor-Less 28-Gb/s NRZ Optical Receiver Analog Front-End Optimization Using BAG in 28-nm CMOS,” IDEC Journal of Integrated Circuits and Systems, vol. 11, no.1, pp.32-37, 2025.

Domestic Conference Presentation

[1] **성민혁**, 조영관, 최우영, “1.3 *m*m 대역 25-Gbps Silicon Micro-Ring Modulator의 Parametric Optimization,” 2018 Photonics Conference, 28-30 Nov., 2018.

[2] **성민혁**, 조영관, 최우영, “Date Rate에 따른 실리콘 링 변조기의 구조 최적화,” 제26회 광전자 및 광통신 학술대회 (COOC 2019), 2-5 Jun., 2019.

[3] **성민혁**, 조영관, 최우영, “Performance Optimization of 25-Gbps O-Band Depletion-Type Silicon Ring Modulators,” 2019 Photonics Conference, 28-30 Nov., 2019.

[4] **성민혁**, 김현규, 지용진, 임철순, 조준형, 배영석, 최우영, “Si Photonics 기반 Mach-Zehnder 변조기의 디지털 및 아날로그 특성,” 2022 Photonics Conference, 28-30 Nov., 2022.

[5] **성민혁**, 지용진, 최우영, “실리콘 기반 Ring-Assisted Mach-Zehnder 광 변조기의 동적 특성 시뮬레이션,” 2024 Photonics Conference, 27-29 Nov., 2024.

[6] Hyun-Kyu Kim, Yongjin Ji, **Min-Hyeok Seong**, and Woo-Young Choi, “FPGA Controller for Si Photonic MZI-Based 2 × 2 Optical Switch,” 한국광학회 제33회 정기총회 및 2022 동계학술발표회, 16-18 Feb., 2022.

[7] 임철순, **성민혁**, 조준형, 백선우, 최우영, 이승의, 배영석, “마이크로파 신호수신용 광자기반 수신기,” 2023 한국군사과학기술학회 종합학술대회, 15-16 Jun., 2023.

Patents

[1] **Min-Hyeok Seong** and Woo-Young Choi, "실리콘 마크젠더 변조기 기반 광자 RF 믹서," Korea Patent (*Registered*), Registration No. 10-2871979, Oct. 13, 2025.

[2] **Min-Hyeok Seong** and Woo-Young Choi, "Silicon Mach-Zehnder Modulator-Based Photonic RF Mixer," USA Patent (*Pending*), Application No. US 19/351,422, Oct. 7, 2025.

Awards

[1] 우수 논문상: “Performance Optimization of 25-Gbps O-Band Depletion-Type Silicon Ring Modulators,” 2019 Photonics Conference, 28-30 Nov., 2019.

[2] Best Student Paper Finalist, “A highly linear and compact Si ring-assisted mach-zehnder modulator at X band,” International Topical Meeting on Microwave Photonics 2025 (MWP 2025), 14-17 Oct., 2025.